

**TUNING MELT/BRUSH INTERACTIONS FOR
FUNCTIONAL POLYMER FILMS**

A Thesis

Presented to

the Faculty of the Department of Chemical and Biomolecular Engineering

University of Houston

In Partial Fulfillment

of the Requirements for the Degree

Doctor of Philosophy

in Chemical Engineering

by

Indranil Mitra

May 2015

**TUNING MELT/BRUSH INTERACTIONS FOR
FUNCTIONAL POLYMER FILMS**

Indranil Mitra

Approved:

Chair of the Committee
Gila Stein, Assistant Professor,
Chemical and Biomolecular Engineering

Committee Members:

Vincent M. Donnelly, Professor,
Chemical and Biomolecular Engineering

Megan Robertson, Assistant Professor,
Chemical and Biomolecular Engineering

Paul Ruchhoeft, Associate Professor,
Electrical and Computer Engineering

Haleh Ardebili, Assistant Professor,
Mechanical Engineering

Suresh K. Khator, Associate Dean,
Cullen College of Engineering

Michael P. Harold,
Professor and Chair,
Chemical and Biomolecular Engineering

Acknowledgements

First and foremost, I would like to take this opportunity to express my sincere gratitude to my advisor, Dr. Gila Stein for her continuous support in my Ph.D study and research. I am indebted to her for providing me with motivation, guidance, ideas and care throughout this endeavour. I would also like to thank her for her patience, enthusiasm, profound knowledge and help in almost everything. I do not think I would have been able to accomplish my Ph.D without her persistent efforts to make me work hard, be organized and accurate.

My deepest gratitude also goes to all of my committee members. In particular I sincerely appreciate Dr. Vincent Donnelly and Dr. Megan Robertson for all their feedback and suggestions without which this project would never have reached fruition.

I also would like to extend my heartfelt thanks to all my Professors in the Chemical & Biomolecular Engineering Department, University of Houston for providing me with an outstanding academic environment.

I was hugely benefited from the regular use of the Nanofabrication Facility at the University of Houston, and appreciate all the help and support given by it's staff members. I also acknowledge the Advanced Photon Source in Argonne National Laboratory, especially Dr. Joe Strazalka for the use of beamline 8-ID-E.

For the work on bottlebrush polymers, I would really like to thank Dr. Rafael Verduzco's group for the full help with the synthesis work, in particular to Dr. Xianyu Li and Stacy Pesek. I would also like to thank Dr. Brad Lokitz, Dr. David Uhrig and Dr. John Ankner for the help with neutron reflectivity experiments.

I would also like to thank my wonderful lab members in Dr. Stein's group who have already graduated: Dr. Ginusha Perera, Dr. Suchanun Mounghai and Dr.

Nikhila Mahadevapuram. Next I would like to thank the present members who have really made our lab a special place to work: Abhijit Patil, Saeed Ahmadi Vaselabadi, David Truong, Adeline Mah and Minnie Lahoti. I am also very pleased to extend my thanks to all the undergrads who have worked in our lab for the last couple of years and made our lab so vibrant.

This is also a moment to acknowledge the help, friendship and cooperation of my colleagues in the department. They are too many to name, but each of them has helped me in some way or the other which I will remain indebted to.

Last but certainly not the least I profusely thank my friends, relatives and family members who stood beside me through every phase of my life and have given me the strength to live, learn and grow.

**TUNING MELT/BRUSH INTERACTIONS FOR
FUNCTIONAL POLYMER FILMS**

An Abstract
of a
Thesis
Presented to
the Faculty of the Department of Chemical and Biomolecular Engineering
University of Houston

In Partial Fulfillment
of the Requirements for the Degree
Doctor of Philosophy
in Chemical Engineering

by
Indranil Mitra

May 2015

Abstract

Polymer films are employed in a variety of industries that include electronic materials, anti-fouling coatings, barrier coatings, and adhesives. In many applications, the functionality of these films is controlled by surface and interfacial properties. Polymer brushes can modify the chemistry, energetics and function at a polymer/substrate or polymer/air interface. This thesis describes two systems where the structure and function of a polymer coating are controlled by interactions at a brush/melt interface.

First, we investigated the role of substrate “neutrality” on domain ordering in thin films of poly(styrene-*b*-methyl methacrylate) (PS-PMMA) lamellar diblock copolymers confined between a “neutral” free surface on the top and “nearly neutral” brushed poly(styrene-*r*-methyl methacrylate) silicon substrate at bottom. The PS-PMMA film thickness (t) and brush grafting density (Σ) were systematically varied to examine their impacts on in-plane and out-of-plane ordering. A combination of high resolution microscopy and grazing-incidence small angle X-ray scattering characterizes lateral order and out-of-plane ordering respectively. Lateral correlation lengths at the top of the film scaled as t^n , where the exponent n increased from approximately 0.75 to 1 as Σ decreased from 0.6 to 0.2 nm⁻². Out-of-plane defects such bent or tilted domains were detected in all films. Our results demonstrate that preferential interactions at the substrate can contribute to both in-plane and out-of-plane disorder.

Second, we studied the phase behavior of bottlebrush polystyrene (PS) and linear deuterated polystyrene (dPS) in thinfilms. These nearly athermal systems exhibit wetting and dewetting transitions that drive bottlebrush dispersion or aggregation, respectively. These effects depend on the relative degrees of polymerization of matrix chains N_m to those of bottlebrush side-chains N_{sc} . When N_m/N_{sc} is low (≤ 1.6), the

bottlebrushes are dispersed throughout the film thickness with a slight excess at the free surface and substrate interfaces. When N_m/N_{sc} is high (≥ 8), the bottlebrushes are depleted from the interior of the film and strongly segregated at the interfaces. The interfacial excess is driven by an entropic depletion attraction effect. These studies demonstrate that low concentrations of certain bottlebrush polymer architectures can generate brushlike surfaces and interfaces in any thermoplastic material through a spontaneous, entropy-driven segregation process.

Table of Contents

Acknowledgements	iv
Abstract	vii
Table of Contents	ix
List of Figures	xii
List of Tables	xviii
Chapter 1 Introduction	1
1.1 Introduction	1
1.2 Polymer Thin Films	2
1.2.1 Block Copolymers	2
1.2.2 Thermodynamics of Diblock Copolymers	3
1.2.3 Diblock Copolymer Thin Films	5
1.2.4 Segregation of Polymer Blends at Interfaces	9
1.3 Goal of the Work	10
Chapter 2 Role of Substrate Interactions on In-Plane and Out-of-Plane Order in Thin Films of Lamellar Copolymers	12
2.1 Introduction	12
2.2 Experimental Procedures	15
2.2.1 Materials	15
2.2.2 Brush Preparation.	15
2.2.3 Brush Thickness.	16

2.2.4	Surface Energy.	17
2.2.5	PS-PMMA Thin Films.	17
2.2.6	Microscopy.	18
2.2.7	Grazing-Incidence Small Angle X-Ray Scattering (GISAXS).	19
2.3	Results and Discussions	20
2.3.1	Substrate Preparation.	20
2.3.2	Substrate Neutrality.	21
2.3.3	Lateral Order.	27
2.3.4	GISAXS.	30
2.3.5	Physics of Out-of-Plane Disorder.	41
2.4	Conclusions	45

Chapter 3 Thin film phase behavior of bottlebrush/linear polymer

	blends	48
3.1	Introduction	48
3.2	Experimental Procedures	50
3.2.1	Materials	50
3.2.2	Synthesis of NB-PS-CTA Macromonomers	50
3.2.3	P(NB-PS6K-CTA)	51
3.2.4	P(NB-PS)	51
3.2.5	Synthesis of Deuterated Linear Polystyrene (dPS)	52
3.2.6	Instrumentation	53
3.2.7	Gel Permeation Chromatography (GPC)	53
3.2.8	Nuclear Magnetic Resonance Spectroscopy (NMR)	53
3.2.9	Preparation of Thin Film Blends	54
3.2.10	Film Thickness Characterization	54
3.2.11	Secondary Ion Mass Spectrometry (SIMS)	54

3.3	Results	55
3.4	Conclusions	66
Chapter 4	Conclusion and Outlook	68
4.1	Future Directions	74
References	77
Chapter A	Appendix A	104
Chapter B	Appendix B	115

List of Figures

Figure 1.1	Cartoon of a diblock copolymer.	3
Figure 1.2	Theoretical phase diagram for diblock copolymer morphology [1, 2].	4
Figure 1.3	Asymmetric BC for diblock copolymer thin films a) parallel morphology for commensurate film thickness and for incommensurability b) holes and c) islands of height comparable to lamellar periodicity.	7
Figure 1.4	Perpendicular lamellae structures for arbitrary film thickness when the neutrality of the substrate as well as the free surface with respect to both the blocks is achieved.	9
Figure 2.1	Mixed domain orientations in a PS-PMMA lamellar copolymer. Film thickness is $t = 1.2L_0$. Sample was annealed at 240 °C, then annealed again at 200 °C for two days. Scale bar = 250 nm.	22
Figure 2.2	Fraction perpendicular lamellae. (a) Annealing at 240 °C for 10 min. H/L: hexagonal and lamellar structures. (b) Annealing at 200 °C for 2 days. The dashed line is a guide to the eye.	23
Figure 2.3	AFM images with parallel domain orientations. Samples heated at 200 °C with grafting density of 0.20 nm^{-2} a) $t/L_0 = 2.3$, and b) $t/L_0 = 2.7$. Inset plots denote the topography “ z ” along the line cut “ x ”.	24

Figure 2.4	Microscopy measurements for different film thicknesses (t/L_0) and brush grafting densities (Σ). The grains in each image are colored according to their in-plane orientation.	28
Figure 2.5	(a) OCL (ζ/L_0) at the top of the film as a function of film thickness (t/L_0). Lines are best-fit to a power law $\zeta \propto t^n$. (b) OCL (ζ/L_0) at the top of the film as a function of brush grafting density (Σ).	29
Figure 2.6	GISAXS patterns for films with thicknesses (a) $t/L_0 \simeq 1$; and (b) $t/L_0 \simeq 2.5$. ($\alpha^i = 0.22^\circ$). Arrows (1) and (2) indicate the scattering rod and Debye-Scherrer rings, respectively, at the first-order peak ($2\Theta \approx 0.21^\circ$).	31
Figure 2.7	(a) Rocking curve and (b) reflectivity for a PS-PMMA film thickness of $t/L_0 = 1.5$ brush ($\Sigma = 0.59 \text{ nm}^{-2}$) (c) and (d) show the first-order peak before and after background correction, respectively.	34
Figure 2.8	First-order diffraction rod as a function of brush grafting density for (a) $t/L_0 = 1$ and (b) $t/L_0 = 2$. Solid black line is the best-fit to the DWBA model ($\alpha^i \approx 0.22^\circ$).	35
Figure 2.9	(a) Domain probability density (σ_γ) of tilt angles. (b) σ_γ as a function of film thickness t/L_0 . Dashed line marks the resolution limit for this method of analysis. (c) σ_γ as a function of brush grafting density Σ	37
Figure 2.10	(a) γ_{max} as a function of normalized film thickness t/L_0 . Dashed line marks the resolution limit. (b) γ_{max} as a function of brush grafting density Σ	39

Figure 2.11	Comparison of DWBA modeling (σ_γ) and contour analysis (γ_{max}) The solid line marks $3\sigma_\gamma = \gamma_{max}$	40
Figure 2.12	(a) For fixed bending curvature, γ_{max} increases with film thickness. (b) Free energy penalty (per chain) for domain curvature.	42
Figure 2.13	Cross-sectional SEM for $t/L_0 = 1.4$ and $\Sigma = 0.45 \text{ nm}^{-2}$. Horizontal yellow lines denote the top and bottom interfaces, while vertical green lines denote the approximate domain orientation.	44
Figure 3.1	Synthetic scheme for the preparation of bottlebrush polymers with PS side-chains. i) AIBN, styrene, 60C, ii) CH_2Cl_2 , $((\text{H}_2\text{IMeS})(3\text{-Br-Py})_2(\text{Cl}_2)\text{RuCHPh})$ iii) THF, hexylamine, tributylphosphine.	57
Figure 3.2	Concentration of bottlebrush polymer (φ) as a function of depth of film. Each column and row has different N_m , and different annealing times (165 C) respectively. (red: $N_b = 193$, and blue: $N_b = 90$).	59
Figure 3.3	Cartoon illustrating the segregation profiles from SIMS after thermal annealing. As N_m increases, bottlebrush polymers segregate at both interfaces (with a bias toward accumulation at the substrate).	60
Figure 3.4	Interfacial excess z^* as a function of N_m and annealing time. Open and closed symbols correspond with surface and substrate excess, respectively. Red squares: $N_b = 193$ and blue diamonds: $N_b = 90$	61

Figure 3.5	Bulk bottlebrush concentration φ^∞ as a function of N_m and annealing time. Closed symbols: $N_b = 193$ and open symbols: $N_b = 90$. $\varphi^\infty < 0.1$ indicates that bottlebrush is depleted from the middle of the film.	62
Figure 4.1	Patchy microscopy images for two BCP film thickness on silane substrate exposed for $\tau_{ox} = 15$ secs. Upper panel is the optical image and lower one is the AFM image.	70
Figure 4.2	Optical, SEM and GISAXS characterization of thin films on SAM oxidized for different times as shown above. (All film thickness are $t/L_0 \sim 1$ except for $\tau_{ox} = 20$ secs, film thickness is around $0.5L_0$	71
Figure 4.3	GISAXS data for cylindrical diblocks for $t/L_0 = 1.09$ a) T: 190 °C; time: 10 min, b) T: 240 °C; time: 10 min, c) T: 190 °C; time: 24 hours and d) T: 240 °C; time: 24 hours.	72
Figure 4.4	GISAXS line cuts for cylindrical diblocks for $t/L_0 = 1.09$ a) T: 190 °C; time: 10 min, b) T: 240 °C; time: 10 min, c) T: 190 °C; time: 24 hours and d) T: 240 °C; time: 24 hours. Arrows mark the relative peak positions.	73
Figure 4.5	Effect of the frequency of chemical pattern on lamellar diblock copolymer ordering. a) Well ordered perpendicular lamellar and b) presence of tilted domains.	75
Figure A.1	Brush thicknesses from X-ray reflectivity. Best fit results in (a-e) are 6.2 nm, 4.8 nm, 4.4 nm, 3.4 nm and 2.6 nm, respectively.	104
Figure A.2	Normalized orientational correlation length as a function of normalized film thickness.	105

Figure A.3	Area fraction of perpendicular lamellae (f_{perp}) as a function of normalized film thickness (t/L_0) and annealing time.	106
Figure A.4	Perpendicular lamellae are detected after annealing for 6 hours at 230 °C. Normalized film thickness is noted on each image.	107
Figure A.5	Surface microscopy images as a function of film thickness and grafting densities. Image width = 3 μm	108
Figure A.6	Surface microscopy images as a function of film thickness and grafting densities. Image width = 3 μm	109
Figure A.7	(a) In-plane line shape example; (b) FWHM as a function of normalized film thickness.	110
Figure A.8	Plots of intensity (I) verses scattering vector (q_y) for PS-PMMA thin films on brushes with Σ (a) 0.32 nm^{-2} , and (b) 0.59 nm^{-2} . The first-order peak is denoted as q^*	111
Figure A.9	Film of thickness $t = 1.5L_0$ on brush with $\Sigma = 0.59 \text{ nm}^{-2}$. Substrate orientation is marked by the white line. Yellow lines mark approximate domain orientation with respect to the substrate.	112
Figure A.10	Film of thickness $t = 2L_0$ on brush with $\Sigma = 0.45 \text{ nm}^{-2}$	113
Figure A.11	Film of thickness $t = 2L_0$ on brush with $\Sigma = 0.45 \text{ nm}^{-2}$ at higher magnification compared to Figure A.10.	114
Figure B.1	^1H NMR spectra of PS bottlebrush with CTA side-chain endgroups (P(NB-PS-CTA), top); and PS bottlebrush with thiol side-chain endgroups (P(NB-PS-SH) , bottom)	115
Figure B.2	Size-exclusion chromatography analysis of PS bottlebrush and macromonomers used for PS bottlebrush batch 1 (left) and batch 2 (right).	116

Figure B.3	AFM measurements of blend films (10 wt% bottlebrush polymer). (a,c) Height and phase measurements of films surface, $N_m = 19$; (b,d) Height and phase measurements of films surface, $N_m = 2500$	118
Figure B.4	Optical microscopy (2.5X) of blend films (10 wt% bottlebrush polymer, $N_{sc} = 61$). N_m is noted on each micrograph, along with the annealing time at 165 °C.	119
Figure B.5	Optical microscopy (100X) of blend films (10 wt% bottlebrush polymer, $N_{sc} = 61$). N_m is noted on each micrograph, along with the annealing time at 165 °C.	120
Figure B.6	φ as a function of depth into the film Each column has different N_m , and each row, different annealing time (165 C). (red: $N_b = 193$, and blue: $N_b = 90$).	121
Figure B.7	GPC spectra of dPS macromonomer (NB-dPS-CTA, red line) and dPS bottlebrush (P(NB-dPS-CTA), black line).	122
Figure B.8	SIMS data of dPS bottlebrushes (BB) with hydrogenated linear PS. The dPS BB has $N_{sc} = 52$ ($\mathcal{D} = 1.23$) and $N_b = 49$ ($\mathcal{D} = 1.28$). The linear PS matrix has $N_m = 2476$ ($\mathcal{D} = 1.05$).	124
Figure B.9	Representative neutron reflectivity spectra of bottlebrush polymer mixed with 2K deuterated linear PS for as cast and thermally annealed films. Data were fit with a 1, 2, or 3-layer model.	126

List of Tables

Table 2.1	Material Characteristics	15
Table 2.2	Brush thicknesses determined with X-ray reflectivity (XRR). Processing conditions (T , τ) are reported for each brush system.	16
Table 2.3	Contact angle measurements and surface energy calculations for P(S- r -MMA) brushes.	21
Table 2.4	Contact angle measurements and surface energy calculations for PS, PMMA, and PS-PMMA (control samples).	21
Table 2.5	Scaling exponent n for OCL (ζ) as a function of film thickness, i.e., $\zeta \propto t^n$. Exponent is reported for each brush grafting density Σ	30
Table 3.1	Characteristics of Bottlebrush Polystyrene	55
Table 3.2	Characteristics of Linear Deuterated Polystyrene	58
Table B.1	Critical temperature predicted by Flory-Huggins theory for analogous linear PS/linear dPS blends.	117

1 Introduction

1.1 Introduction

Understanding surface energetics and physics of polymer thin films have emerged as one of the most challenging areas of research in recent times for its wide applicability in a variety of areas. There is a lot of work are going on at present to get a better understanding of the problem by utilizing different polymer systems [3–7].

Construction of precisely ordered nanoscale structures leads to the miniaturization of functional devices which have huge advantages in micro and macroscale devices due to their large surface/volume ratio, high throughput, and ability to control features at nano-meter length scales [8–10]. Top down lithographic process currently dominates as the most critical procedure for patterning nanoscale structures. Exposure of an appropriate material to electromagnetic radiation introduces a latent image into the material as a result of a set of chemical changes in its molecular structure. However the process is usually limited by Rayleigh resolution criterion. Most of the methods of improvement of the top-down approaches suffer from high operating costs, multiple processes and the ability to satisfy the different material requirements and makes it difficult to reproduce both topographical patterns with a wide range of well-defined structures and chemical patterns with well-defined geometries [11, 12].

Thus the expanding avenues in electronic devices are approaching a bottleneck in order to achieve cost effective miniaturization solutions. Self-assembly methods are in particular promising alternatives. These bottom-up approach for pattern generation heavily relies on assembly of small building blocks such as polymer molecules or nanoparticles [13–15]. Self-assembly methods using block copolymers (BCPs) have

emerged as frontrunners in this approach [16, 17]. BCPs are composed of sequences of chemically distinct repeat units and yield materials with different hybrid properties [18]. The underlying physics of BCPs both in bulk and thin films are already well established and the mechanical properties of the thin films formed from BCPs can be well compared with the conventional polymer photoresists and BCPs have high resolution, high throughput, and low cost. However at the same time BCP's lack long range order and are plagued with defects [19, 20]. This is of critical importance to extend block copolymers for commercial applications and a number of strategies are emerging which includes tuning surface energetics, guided assembly and using blends of polymers [21].

1.2 Polymer Thin Films

Our work is related to polymer thin films. Polymer films have found applicability in areas ranging from microelectronics and sensors to adhesives and bio-medical devices [22, 23]. Understanding wetting phenomena on polymer surfaces has thereby become important and interfaces has played a crucial role in quantitative segregation studies [24]. In particular interfacial energetics at interfaces play a tremendous role in surface physics of polymer thin films. In this section we first discuss about bulk behavior of diblock copolymer and diblock copolymer thin film physics. In the last subsection we briefly mention about the role of polymer blends in understanding of segregation phenomena.

1.2.1 Block Copolymers

As we have just mentioned, the critical importance of block copolymers lies in their superb control in self-assembly and applications of the resulting nanostructures

[16]. Thus the immiscibility and covalent linkage of the blocks governs the self-assembly of BCPs into a range of highly ordered morphologies. In this thesis our work mainly involves understanding the behavior of diblock copolymer thin films in nanostructure generation.

1.2.2 Thermodynamics of Diblock Copolymers

In Figure 1.1 we show a cartoon of a diblock copolymer which plays the central role in our study. By definition a diblock copolymer is a polymer which has two types of monomers A and B arranged in such a way that there is a chain of each monomer and those chains are grafted together to form a single copolymer chain.

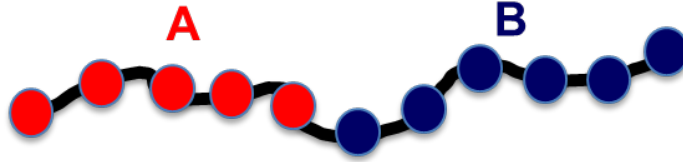


Figure 1.1: Cartoon of a diblock copolymer.

Before we discuss the thermodynamics of diblock copolymer system, we would like to motivate the basic relevant physics for a relatively simpler system, a polymer blend. The phase behavior of a polymer blend can be described thermodynamically using the Flory-Huggins (FH) theory [25–27]. For a blend of two homopolymers A (degree of polymerization: N_A , volume fraction: ϕ_A) and B (degree of polymerization: N_B , volume fraction: ϕ_B) the free energy of mixing is given by

$$\frac{\Delta G_{mix}}{kT} = \frac{\phi_A}{N_A} \ln(\phi_A) + \frac{\phi_B}{N_B} \ln(\phi_B) + \chi \phi_A \phi_B, \quad (1.1)$$

where χ is Flory–Huggins interaction parameter. Equation 1.1 clearly shows that the free energy has contribution from configurational entropy of the individual polymer

system apparent in the first two terms and the last term is the enthalpic/energetic contribution as a result of A–B monomer interactions, which depends on the chemistry of respective molecules and also the temperature.

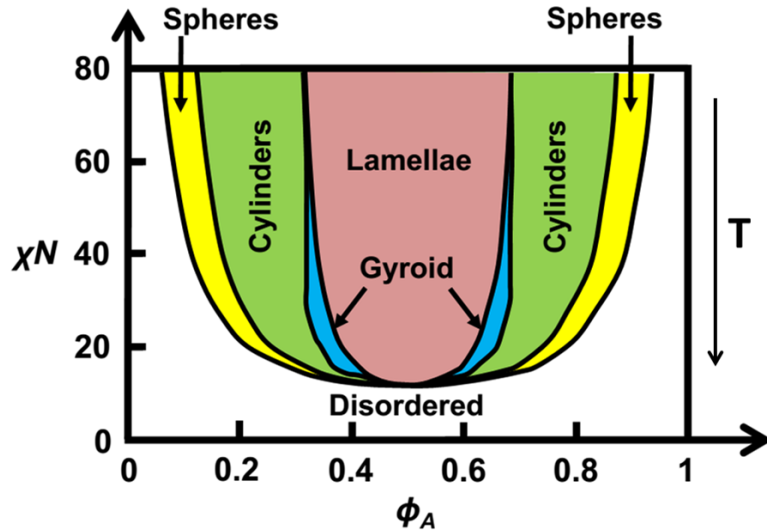


Figure 1.2: Theoretical phase diagram for diblock copolymer morphology [1, 2].

In the case for block copolymers there is a subtle competition between energetic and entropic factors which leads to a disorder-to-order (ODT) phase transition [2] at nanometer length scales. However, unlike polymer blends, the connectivity of the two blocks for the block copolymer case tends to assemble the A and B components on opposite sides of the interface and prevents macrophase separation. Thus self-assembly is an equilibrium process which is maintained by forces between the competing blocks for block copolymer systems. It is now well established from self-consistent field theory (SCFT) calculations [2, 28, 29] that the equilibrium morphology of a system of block copolymers is dependent on the total degree of polymerization N , the pure component composition (ϕ_i) and the Flory-Huggins interaction parameter χ . The strength of segregation is proportional to χN whose value when exceeds a threshold

$(\chi N)_{ODT}$, the block copolymer microphase separates into a periodically ordered structures with length scales spanning between 5–200 nm [30]. The results for the phase diagram and geometries obtained using SCFT [28] is shown in Figure 1.2. Microphase segregation has two distinct regimes as shown in Figure 1.2. For $\chi N \ll 10$ the chains behave close to being Gaussian coils and are in a disordered phase. In this regime the entropic terms are larger than the interaction term. However very near to ODT limit where $\chi N \approx 10.5$, we are in the weak segregation limit and the volume fraction of one of the blocks in this case spatially varies sinusoidally about the average value. The strong segregation limit (SSL) is defined by $\chi N \gg 10$ where the interaction energy takes over where the interphase between the blocks is sharp and localized [31]. The dominant forces drives the blocks to segregate into well defined microdomains, perturbing the chains from their Gaussian configurations and changing the dependence of the periodicity on the degree of polymerization and chi-parameter [32].

1.2.3 Diblock Copolymer Thin Films

The natural ability of block copolymers to self-assemble into ordered patterns has given rise to a tremendously prospective avenue for specific lithographic tools to allow controlling the polymer structures upon formation of thin films [33]. Patterning via thin and ultra-thin block-copolymer films is one of the hot research areas at present for developing new generations of functional devices [22, 34]. These materials can improve the quality of projection lithography by “shrinking” the sizes of patterned features [20, 35, 36], so leading semiconductor manufacturers are considering their use in next-generation integrated circuit manufacturing. Selective removal of one of the blocks results in templates that can be used in further nanofabrication processes.

Spin coating is the most prevalent method for producing block copolymer films whereby polymer film spreads on the substrate by centrifugal forces and the thickness

of the film is controlled mainly by the spin speed and the concentration of the block copolymer and by the volatility of the solvent which has been used to prepare the polymer solution. The dynamic effects of solvent evaporation can induce orientational field to generate variety of morphologies, but in general the films are heated to induce phase separation, so thin film thermodynamics will determine the resulting domain structure and orientation.

Although the bulk phase behavior of block copolymers has been well described in terms of two parameters of the composition and the degree of segregation between the blocks [37], the thin film ordered structures and their orientations are more complicated due to the film preparation conditions and film confinement conditions such as the film thickness and wetting properties of each block on the substrate surface and at the air/film interface [22,38–41]. One of the key arguments against application of block copolymers as lithographic templates is the lack of long range order due to the presence of a combination of defects. Thus, investigation of these defects with an aim to eliminate them will play a very important role in the success of block copolymers as lithographic materials.

There is a lot of interrelationship between confinement, substrate surface effects which can be made by modifying substrates, choosing proper annealing conditions for solvent and using films of appropriate film thickness to generate large number of defect free regularly sized and shaped domains with a specific structure and orientation.

Our object of interest in this work is one of the most widely used block copolymer system, poly(styrene-*b*-methyl methacrylate) (PS-PMMA) which we have mainly focused on hereafter. PS-PMMA on oxidized silicon is an example of a system with asymmetric boundary conditions (BC), meaning different blocks are preferred at each interface which is a consequence of imbalance of surface energetics. PS has a slightly lower surface tension than PMMA (below 220 °C), which favors the formation

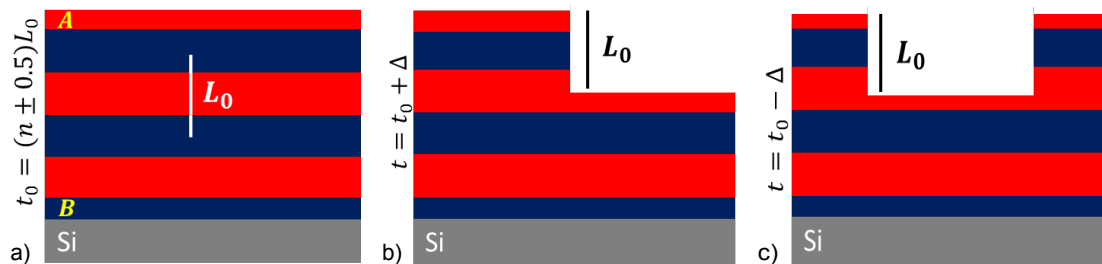


Figure 1.3: Asymmetric BC for diblock copolymer thin films a) parallel morphology for commensurate film thickness and for incommensurability b) holes and c) islands of height comparable to lamellar periodicity.

of a PS wetting layer at the free surface, and PMMA will adsorb at the silicon substrate to form a brush-like layer at any processing temperature [42,43]. In general the preferential interactions at each interface induce a parallel layering of domains. The film thicknesses that are commensurate with asymmetric wetting are $t = (n + 1/2)L_0$, where n is an integer and L_0 is the equilibrium lamellar period. For films whose thickness deviate from this condition, the film separates into regions of two commensurate thicknesses giving rise to island/hole surface relief structures [42]. In Figure 1.3 we show energetically the most probable structures on an oxidized silicon substrate.

However from a lithographic point of view these structures are not very useful. Lithography requires nanopatterns in the plane of the film, which implies that lamellar domains must be oriented perpendicular to the substrate. At moderate processing temperatures above the glass transition temperature (T_g) for both the blocks, perpendicular PS–PMMA lamellae can be achieved at certain film thicknesses by coating the substrate with a “neutral” material. The term neutral implies that neither block is preferred at the substrate, thereby eliminating any tendency to form wetting layers at the bottom of the film.

The domain orientation and wetting of a block copolymer has a strong dependence on strength and nature of interaction of the substrate boundaries with the polymer components. However, even though the standard neutral coating technique can make the substrate neutral, the air interface is still slightly preferential to PS at least for relatively lower temperatures ($T > T_g$). Thus perpendicular orientation is a relatively unstable configuration which is sustained when film thickness is highly incompatible with asymmetric boundary conditions. Those are cases where the domains orient normal to the substrate to relieve bulk frustration at the expense of a small surface energy gain [44–50]. In particular for the PS–PMMA system, the condition of maximum frustration is roughly $t \simeq L_0$ and films around this thickness are optically smooth (no islands or holes), and the classic fingerprint pattern is detected at the free surface. Films with different thicknesses ($t \neq L_0$) give rise to island and hole structures, or mixed parallel and perpendicular domain orientations [49, 51].

Perpendicular PS–PMMA domain orientations on neutral substrates can be achieved for a wide range of thicknesses by controlling the annealing temperature, copolymer architecture or copolymer molecular weight. Some work, including results from our group, have shown that for high molecular weight copolymers dynamic barriers may stabilize perpendicular orientations by inhibiting island/hole formation [49, 52]. Apart from considering high molecular weight copolymers, the remarkable property unique to PS–PMMA system is the fact that the surface tensions of PS and PMMA are very similar at elevated temperatures (220–240 °C). Thus the target annealing temperature for the block copolymer thin films in that range makes the air interface very close to being neutral [45, 53]. Thus, depending on the efficacy of our neutral coating on the substrate, the operating temperature provides a suitable control to achieve a broader window of film thickness which can sustain stable perpendicular orientations as shown in Figure 1.4.

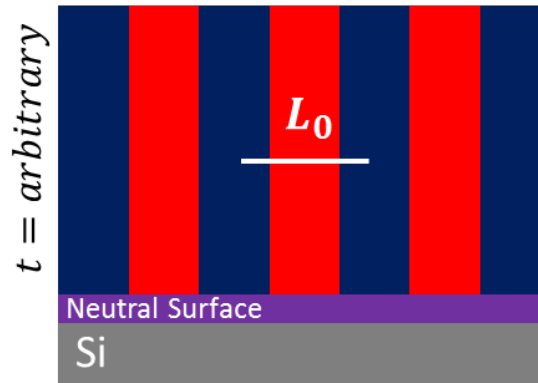


Figure 1.4: Perpendicular lamellae structures for arbitrary film thickness when the neutrality of the substrate as well as the free surface with respect to both the blocks is achieved.

1.2.4 Segregation of Polymer Blends at Interfaces

Phase separation in thin films can be tailored to tune desirable characteristics which can make the surface responsive. A reasonable amount of studies have investigated the phase separation and segregation of polymer blend films. It is observed that segregation is mainly induced by the simply tuning the polymer/substrate interaction through chemical modification of the substrate [54,55]. The variables which influence the segregation morphology will play a very important role in understanding wetting behavior in these systems. It is also important to understand the interrelationship between kinetics and dynamics in surface segregation of polymer blends.

Our main focus has been on understanding the segregation properties of polymer blends consisting of bottle brush polymers with linear polymers [54,56]. Bottlebrushes are macromolecules with polymeric densely grafted side-chains and have found numerous applications in different areas [57,58].

In this work we have understood the role of polymer blends of linear polystyrene with polystyrene based bottlebrushes to understand and control surface properties.

The surface responsiveness may be an indicator of conformational flexibility of the bottlebrushes and by changing the length of the bottlebrush side-chains we can achieve different chemical functionalities and wetting characteristics of polymer thin films [59,60].

1.3 Goal of the Work

Lithographic processes which have applications in the semiconductor industry require precise control over domain orientation and placement, which is potentially achieved through careful tuning of free surface and substrate interactions. In our work we exclusively focus on thin films of symmetric lamellar diblock copolymers which spontaneously self-assemble into nanoscale lamellar domains. Our current work is to examine the role of substrate “neutrality” on domain ordering in thin films of PS–PMMA lamellar copolymers. In this work we have explored neutral coatings based on random copolymers of styrene and methyl methacrylate [48,61,62]. We also have extensively worked on tunable silane chemistries [63,64] and have reported some of the salient issues associated with it in Chapter 4.

Our main emphasis is to explore the effects of interfacial interactions on perpendicular ordering of lamellar diblock copolymers. We investigate how interactions between the polymer blocks and surrounding interfaces influence in-plane and out-of-plane alignment of block copolymer domains. The work will have major impact on high-throughput screening and optimization of neutral coatings for block copolymer lithography [65–67].

For our work related to bottlebrush/linear polymer blends we investigated the phase behavior for bottlebrush polystyrene (PS) and linear deuterated polystyrene (dPS) in thin films. These nearly athermal systems exhibit wetting and dewetting

transitions that drive bottlebrush dispersion or aggregation, respectively. One of the salient aspects of our study was concerned about identifying the key variables which control segregation phenomena in these blend systems.

2 Role of Substrate Interactions on In-Plane and Out-of-Plane Order in Thin Films of Lamellar Copolymers

2.1 Introduction

Thin films of symmetric diblock copolymers will spontaneously self-assemble into nanoscale lamellar domains (i.e., nanolines) [10, 68]. These materials can improve the quality of projection lithography by “shrinking” the sizes of patterned features [20, 35, 69, 70], so leading semiconductor manufacturers are considering their use in next-generation integrated circuit manufacturing. The most demanding lithographic processes require precise control over domain orientation and placement, which is potentially achieved through careful tuning of free surface and substrate interactions. The objective of our current work is to examine the role of interfacial interactions on domain ordering in thin films of poly(styrene-*b*-methyl methacrylate) (PS-PMMA) lamellar copolymers.

Lithography requires nanopatterns in the plane of the film, so lamellar domains must be oriented perpendicular to the substrate. The perpendicular orientation is stable when the free surface and substrate are energetically “neutral” with respect to each block, so there is no tendency to form wetting layers at either interface. In the case of PS-PMMA, processing schemes that achieve interfacial neutrality are well-known: the melt surface tensions of PS and PMMA are equal at elevated temperature [45, 53], and the substrate chemistry can be tuned with established protocols

to screen preferential interactions with one block [48, 61–64, 71]. A perpendicular domain orientation is normally inferred in these systems from the presence of “fingerprint” patterns at the free surface and the absence of islands/holes over a broad range of film thicknesses. However, subtle changes in interactions at the substrate could impact both in-plane and out-of-plane order, and such physics are difficult to interrogate with surface microscopy alone.

Perpendicular lamellae and parallel cylinders are both examples of smectic block copolymer phases, and their in-plane ordering on homogeneous surfaces has been extensively studied through theory and experiment [72–77]. Fingerprint patterns are characterized by dislocations and disclinations, and the densities of these topological defects will increase with proximity to the order-disorder transition temperature. The phase behavior and defectivity in these systems are sensitive to thin film confinement and interfacial interactions. In perpendicular lamellar phases, the order-disorder transition temperature can vary with the composition of neutral substrate coatings [78], and defect densities increase as film thickness is reduced [77, 79, 80]. Similarly, confinement of parallel cylinders in a monolayer can suppress the order-disorder transition temperature and increase the defect densities [76], with the maximum disorder detected on adsorbed brushes compared with grafted brushes [81, 82]. Adsorbed brushes are thought to have lower chain densities (per unit area) than grafted brushes, and are therefore less effective at screening interactions between a substrate and overlying copolymer film.

Out-of-plane order in perpendicular block copolymer phases has received little attention in experiments, but there is evidence that domains are not perfectly perpendicular to the substrate. One work used detailed studies of pattern transfer to show that perpendicular cylinders can tilt and bend [83], which was described as a

response to the strain field associated with in-plane topological defects. A different study used grazing-incidence small angle X-ray scattering to show tilting and bending in perpendicular lamellae [49], and this behavior was attributed to weakly preferential interactions at the substrate. Much of the current understanding of three-dimensional order is derived from theoretical models [67]. For example, a variety of simulation methods predict that preferential interactions at a boundary can locally deform domain shapes and introduce complex morphologies [70, 84–87], and some of these features have been verified in experiments [70, 86].

The present manuscript describes the effects of substrate interactions on in-plane and out-of-plane defectivity in perpendicular lamellar phases. Using a combination of X-ray reflectivity (XRR), grazing-incidence small angle X-ray scattering (GISAXS), and surface microscopies, we examine ordering in thin films of PS-PMMA lamellar copolymers prepared on end-grafted poly(styrene-*r*-methyl methacrylate) brushes. The principal experimental variables are normalized PS-PMMA film thickness (t/L_0) and brush grafting density (Σ). While t/L_0 is a common variable for investigations of substrate neutrality, the impact of Σ on lamellar ordering is far less studied [84, 85], and this parameter is rarely reported [10] in experiments. Brushes with a range of Σ are prepared by varying the kinetics of the grafting-to reaction [88], and Σ is characterized through XRR measurements of the dry brush thickness [88, 89]. All PS-PMMA films are processed at an elevated temperature where the blocks have equal surface tensions (approximately), and we use a variant on island/hole studies to establish that PMMA is weakly preferred at the brushed substrate. Therefore, all films are confined between a neutral free surface and a “nearly neutral” substrate. Through detailed analysis of microscopy and GISAXS, we find that all films are characterized by high densities of in-plane and out-of-plane defects, and the defectivity in these systems is at least partly controlled by preferential interactions at the substrate.

2.2 Experimental Procedures

2.2.1 Materials

The diblock copolymer used for these studies is a lamellar poly(styrene-*b*-methyl methacrylate) (PS-PMMA). The equilibrium lamellar periodicity (L_0) for this PS-PMMA copolymer is 46 nm (measured with grazing-incidence small angle X-ray scattering). The segregation strength for this polymer is $\chi N \simeq 45$ and approximately independent of temperature [90]. Polymer brushes were prepared from hydroxyl-terminated poly(styrene-*r*-methyl methacrylate) random copolymers, hereafter denoted by P(S-*r*-MMA). All polymers were purchased from Polymer Source and independently characterized at the University of Houston. The compositions, molecular weights, and dispersities are reported in Table 2.1. Substrates were 3-inch diameter, (100)-oriented silicon wafers. Substrates were cleaned with a UVOCS UV/ozone system for 20 mins to destroy organic contamination and grow a thin oxide layer.

Table 2.1: Material Characteristics

Polymer	Styrene %	M_n (kDa)	\mathcal{D}
PS-PMMA	53% vol	98	1.1
P(S- <i>r</i> -MMA)	59% mol	8.6	1.5
P(S- <i>r</i> -MMA)	55% mol	7	1.3

2.2.2 Brush Preparation.

End-functional random copolymers were dissolved in toluene at a concentration of 1 wt%, and films that were approximately 30 nm thick were prepared by spin-casting on ultraclean silicon substrates. Polymer chains were grafted to the substrate by annealing under low vacuum (10 mTorr) or in a nitrogen-purged glove box for

the temperature and time reported in Table 2.2. Processing conditions were varied to control the thickness of the polymer brushes (annealing temperature T , annealing time τ). Un-grafted polymer was extracted by soaking in toluene with mild agitation. Samples were then dried under a nitrogen stream. The quality of each brush was assessed by measuring the contact angle of water, which was usually 76° after this process. Contact angle was increased to ca. 80° by repeating all steps a second time (includes coating a new film, annealing, and rinsing), which improves the homogeneity of the coating across the wafer surface. This contact angle is consistent with other literature studies [44, 78], and does not change by repeating all steps a third time.

Table 2.2: Brush thicknesses determined with X-ray reflectivity (XRR). Processing conditions (T , τ) are reported for each brush system.

Brush	$T(^{\circ}\text{C})$	τ (hr)	t_b (nm)
55% S	170	48	6.2 ± 0.1
55% S	170	24	4.8 ± 0.1
55% S	230	1	4.4 ± 0.1
55% S	210	1.5	3.4 ± 0.1
59% S	170	48	2.6 ± 0.1

2.2.3 Brush Thickness.

The brush thicknesses were measured using X-ray reflectivity (XRR). XRR experiments were performed at the Advanced Photon Source of Argonne National Laboratory (beamline 8-ID-E) [91]. Data were acquired by varying the incident angle in the range of $0.1\text{-}2^\circ$ using increments of 0.003° , and the intensity at specular reflection was recorded with an avalanche photodiode detector. XRR data were modeled

following the Parratt recursions [92] convolved with an instrumental resolution function [91], where brush thickness (t_b), brush scattering length density (ca. 10×10^{-10} cm⁻²), and native oxide thickness (ca. 1 nm) were refined through regression analysis. The exact algorithm is described in detail elsewhere [93]. The fits to XRR data are included in the Appendix A Figure A.1. The brush thicknesses that were calculated from XRR are reported in Table 2.2. The uncertainties reported in Table 2.2 for t_b reflect the statistically-derived error.

2.2.4 Surface Energy.

The surface energies of all polymer brushes were calculated from equilibrium contact angle measurements based on Wu’s harmonic method [94,95]. Four liquids were used: diiodomethane (non-polar), deionized water (polar), ethylene glycol (polar), and formamide (polar). Contact angles were recorded from at least three points on the substrate using a DataPhysics OCA 15EC goniometer. We report the average and standard deviation in Tables 2.3 and 2.4. Control measurements were performed from thin films of PS and PMMA homopolymer, as well as the PS-PMMA block copolymer (50 nm thick). The PS has M_n of 140 kDa and \bar{D} of 1.6, and the PMMA has M_n of 60 kDa and \bar{D} of 1.4. Note that uncertainty in surface energy calculations reflects the variability in contact angle measurements.

2.2.5 PS-PMMA Thin Films.

Thin films of PS-PMMA block copolymers were prepared on the P(S-*r*-MMA) brushes. PS-PMMA was dissolved in toluene at concentrations that ranged from 1-4 wt%, and solutions were filtered with a 0.2 μ m Teflon mesh. Films that ranged in thickness from 20 nm to 120 nm were prepared by spin-casting and annealed as described in the Results and Discussion. Polymer film thicknesses were measured with

XRR following similar procedures as described for characterization of brush thickness. XRR measurements were conducted at the Advanced Photon Source of Argonne National Laboratory (beam line 8-ID-E). Data were acquired by varying the incident angle in the range of 0.1-2° using increments of 0.003°, and the intensity at specular reflection was recorded with an avalanche photodiode detector. XRR data were modeled following the Parratt recursions [92] convolved with an instrumental resolution function [91], where polymer film thickness, polymer scattering length density (ca. $10 \times 10^{-10} \text{ cm}^{-2}$), surface roughness (ca. 0.3 nm), and oxide thickness (ca. 1 nm) were refined through regression analysis. When modeling XRR data, the “polymer layer” includes both PS-PMMA block copolymer and the underlying P(S-*r*-MMA) brush. (The brush thickness was characterized after the grafting reaction, so this value is subtracted from the “polymer layer” thickness to determine the PS-PMMA layer thickness.)

2.2.6 Microscopy.

The nanoscale structure at the surface of each film was characterized with atomic force microscopy (AFM) and/or scanning electron microscopy (SEM). AFM micrographs were collected with a MultiMode 3 (Veeco) in Tapping Mode using silicon probes with a spring constant of approximately 40 N/m. Typical parameters for data acquisition were 1.7 Hz scan frequency, $5 \mu\text{m} \times 5 \mu\text{m}$ scan area, and 512×512 image resolution. SEM images were recorded with a FEI XL-30FEG SEM in secondary electron (SE) mode. Operating parameters for image acquisition were an accelerating voltage of 5 kV, beam current of 95 pA, working distance of 5 mm, and magnifications ranging from 50-65 kx. Lateral domain order was quantified by calculating the orientational correlation function $g(\vec{r})$ and fitting the azimuthal average to an exponential decay, i.e., $g(r) = \exp(-r/\zeta)$ [72–74]. The exact algorithm is described elsewhere [74].

Average values of the orientational correlation length ζ (normalized by $L_0 = 46$ nm) were computed from a minimum of 5 micrographs and error bars denote the standard deviation, and in some instances are the same size as the symbols. We verified that ζ values calculated from AFM and SEM are identical within error (see Appendix A Figure A.2).

2.2.7 Grazing-Incidence Small Angle X-Ray Scattering (GISAXS).

GISAXS measurements of PS-PMMA films were conducted at the Advanced Photon Source of Argonne National Laboratory (beamline 8-ID-E) [91]. Samples were placed in a vacuum chamber and illuminated with 7.35 keV radiation at incident angles (α^i) in the range of $0.1 - 0.24^\circ$. The off-specular scattering was recorded with a Pilatus 1MF pixel array detector (pixel size = $172 \mu\text{m}$) positioned 2175 mm from the sample. Acquisition times were approximately 10 sec per frame. Each data set was stored as a 981×1043 32-bit tiff image with 20-bit dynamic range. The X-ray penetration depth varies from approximately 10 nm up to the full film thickness as incident angle is increased through the critical angle of the film (ca. 0.17°). All data in this manuscript are displayed as intensity maps $I(2\Theta, \alpha^f)$, where 2Θ and α^f denote in-plane and out-of-plane diffraction angles, respectively.

Rocking curves were recorded at the same beam line to quantify the effects of wafer curvature on incident beam angle, which is necessary for quantitative analysis of GISAXS data with the distorted-wave Born approximation [96]. Measurements were implemented by setting the incident angle to 0.4° and scanning an avalanche photodiode detector about the specular condition (from 0.35 - 0.45° in increments of 0.003°). Data were fit to a Gaussian resolution function,

$$R(q_z) = \frac{1}{\sqrt{2\pi}\delta_{q_z}} \exp\left(-\frac{q_z^2}{2\delta_{q_z}^2}\right), \quad (2.1)$$

where $q_z = 2\pi(\sin[\alpha^f] + \sin[\alpha^i])/\lambda$ is the perpendicular scattering vector (out of plane) and $\delta_{q_z} = (\Delta\lambda/\lambda)q_z + 4\pi\Delta\alpha^i/\lambda$. The wavelength spread is $\Delta\lambda/\lambda = 10^{-4}$ (fixed) [91], and the angular divergence of the beam ($\Delta\alpha^i$) is an adjustable parameter for regression analysis. The angular divergence is typically 5×10^{-5} rad for a 400 μm thick silicon wafer.

2.3 Results and Discussions

2.3.1 Substrate Preparation.

The aim of these studies is to examine the effects of substrate interactions on in-plane and out-of-plane order in lamellar PS-PMMA block copolymers. All PS-PMMA films were cast on silicon wafers that were functionalized with random copolymer P(*S*-*r*-MMA) brushes, and substrate interactions were tuned by varying the brush grafting density. The grafting density Σ for each sample was calculated from the measured brush thickness t_b ,

$$\Sigma = \frac{t_b \rho N_A}{M_n}, \quad (2.2)$$

where $\rho = 1.1 \text{ g/cm}^3$ is the approximate polymer density, N_A is Avogadro's number, and M_n is the number-average molecular weight [88]. Using the brush thicknesses calculated from XRR, we predict that Σ ranges from approximately 0.2 nm^{-2} to 0.6 nm^{-2} . These calculations are summarized in Table 2.3. (If we base the calculation of Σ on weight-average molecular weight instead of M_n , then the estimated value drops by approximately 0.1 nm^{-2} in each case.) The brushes prepared for this work span a broad range in Σ , but the wettability and surface energy determined with contact angle goniometry were consistent among all samples. Referring to the control data

in Table 2.4, the surface energies of brushed substrates are nearly the same as PS-PMMA, and intermediate to those of PS and PMMA homopolymers. The control data in Table 2.4 are consistent with other literature reports [94, 95, 97–100].

Table 2.3: Contact angle measurements and surface energy calculations for P(S-*r*-MMA) brushes.

Brush	t_b (nm)	Σ (nm ⁻²)	H ₂ O (°)	C ₂ H ₆ O ₂ (°)	CH ₃ NO (°)	CH ₂ I ₂ (°)	γ (mN/m)
55% S	6.2 ± 0.1	0.59 ± 0.01	82 ± 1	61 ± 1	70 ± 1	27 ± 1	42.2 ± 0.7
55% S	4.8 ± 0.1	0.45 ± 0.01	83 ± 1	61 ± 1	70 ± 1	25 ± 3	42.6 ± 0.5
55% S	4.3 ± 0.1	0.41 ± 0.01	79 ± 1	61 ± 1	67 ± 1	27 ± 1	42.9 ± 0.7
55% S	3.4 ± 0.1	0.32 ± 0.01	81 ± 1	63 ± 1	69 ± 1	27 ± 2	41.5 ± 0.5
59% S	2.6 ± 0.1	0.20 ± 0.01	81 ± 1	59 ± 1	70 ± 1	25 ± 1	42.6 ± 0.8

Table 2.4: Contact angle measurements and surface energy calculations for PS, PMMA, and PS-PMMA (control samples).

Polymer	H ₂ O (°)	C ₂ H ₆ O ₂ (°)	CH ₃ NO (°)	CH ₂ I ₂ (°)	γ (mN/m)
PS	90 ± 1	69 ± 1	70 ± 1	33 ± 3	40.7 ± 0.6
PMMA	70 ± 1	53 ± 1	54 ± 1	31 ± 2	44.8 ± 0.3
PS-PMMA	85 ± 1	59 ± 1	60 ± 1	36 ± 2	41.1 ± 0.6

2.3.2 Substrate Neutrality.

The following paragraphs describe simple procedures to test for substrate neutrality [49, 101]. The outcomes of these studies demonstrate that the brushed substrates exhibit a weak preference for PMMA over PS. A series of PS-PMMA films with varying thicknesses (in the range of $t/L_0 = 0.5$ to 2.5) were cast on the brushed substrates and annealed in air for 10 minutes at 240°C. These samples were cleaved into two pieces, and one section was further annealed under low vacuum (10 mTorr) for two days at 200°C. We also include one set of data (on brushes with $\Sigma = 0.2$ nm⁻²) that were acquired without the first annealing step at 240 °C [49]. The samples were imaged with high resolution AFM or SEM to characterize ordering at the air

interface. Each micrograph was analyzed with ImageJ software to identify the area fraction of perpendicular domains (f_{perp}). The procedures for image analysis are illustrated by Figure 2.1: A threshold was applied to each image to highlight the regions with parallel and perpendicular domain orientations, and then a binary mask was applied to define regions of interest (ROIs) that correspond with parallel domains. The area fraction of parallel domains (f_{par}) was calculated from the sum of all ROIs divided by the total image area, and $f_{\text{perp}} = 1 - f_{\text{par}}$. Figures 2.2a and 2.2b report the area fraction of perpendicular domains (f_{perp}) as a function of normalized film thickness (t/L_0), brush grafting density (Σ), and final processing temperature (200 °C or 240 °C).

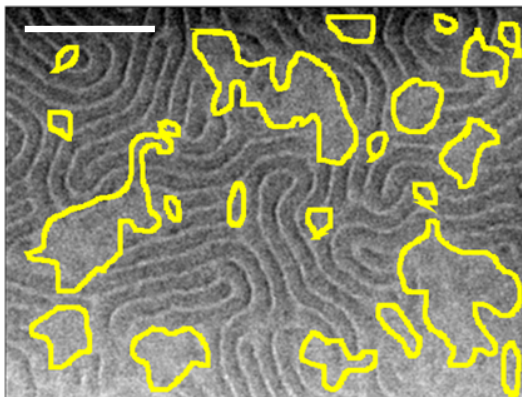


Figure 2.1: Mixed domain orientations in a PS-PMMA lamellar copolymer. Film thickness is $t = 1.2L_0$. Sample was annealed at 240 °C, then annealed again at 200 °C for two days. Scale bar = 250 nm.

After annealing at 240 °C for 10 min, substrates with high grafting densities ($\Sigma > 0.4 \text{ nm}^{-2}$) drive a perpendicular orientation of PS-PMMA lamellae ($f_{\text{perp}} = 1$) at all film thicknesses. The perpendicular orientation is unchanged with an additional 6 hours of annealing (see Appendix A Figures A.3 and A.4), so we conclude that these structures are stable. Samples with low grafting density ($\Sigma < 0.4 \text{ nm}^{-2}$) exhibit perpendicular domains in thicker films ($t/L_0 \geq 1$), but regions of parallel lamellae

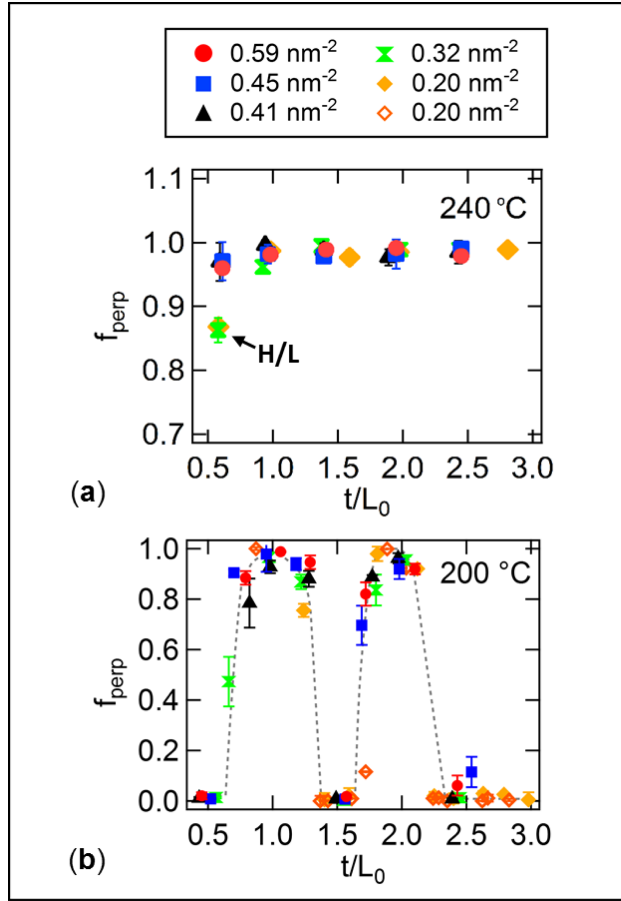


Figure 2.2: Fraction perpendicular lamellae. (a) Annealing at 240 °C for 10 min. H/L: hexagonal and lamellar structures. (b) Annealing at 200 °C for 2 days. The dashed line is a guide to the eye.

and a transition to hexagonal perforated lamellae are detected in ultrathin films ($t/L_0 < 1$). We note that perforated morphologies have been reported in thin films of cylindrical and lamellar block copolymers on preferential substrates [102,103], and examples of these data are included in Appendix A Figure A.5

When annealing temperature is reduced to 200 °C, the domain orientations exhibit a strong dependence on normalized film thickness t/L_0 . Perpendicular domains ($f_{\text{perp}} = 1$) are observed when film thicknesses are integer multiples of the lamellar periodicity, i.e., $t \approx nL_0$. Mixed orientations ($0 < f_{\text{perp}} < 1$) occur at intermediate

thicknesses near $t \approx (n \pm 0.2)L_0$. Parallel lamellae ($f_{\text{perp}} = 0$) are detected near $t \approx (n + 0.5)L_0$. These findings are true for both annealing schedules, meaning with

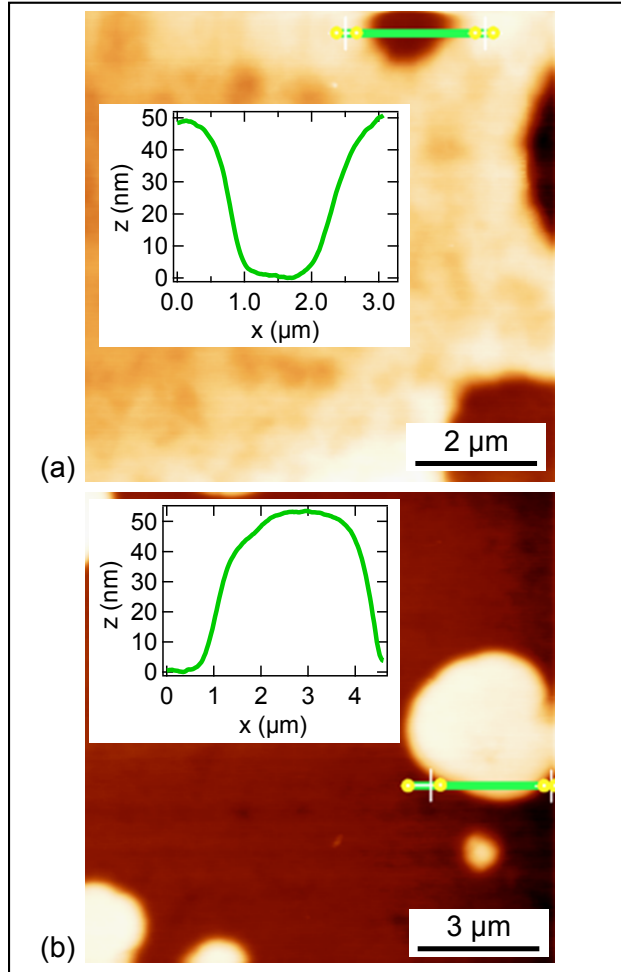


Figure 2.3: AFM images with parallel domain orientations. Samples heated at 200 °C with grafting density of 0.20 nm^{-2} a) $t/L_0 = 2.3$, and b) $t/L_0 = 2.7$. Inset plots denote the topography “ z ” along the line cut “ x ”.

and without the first annealing step at 240 °C, so these outcomes reflect the equilibrium state at 200 °C. Furthermore, when lamellae are parallel to the air interface at 200 °C, the samples can exhibit low densities of islands and holes. The heights of islands and depths of holes are approximately equal to the lamellar periodicity of $L_0 = 46 \text{ nm}$. Representative AFM data are included in Figure 2.3.

The dependence of f_{perp} on t/L_0 at each temperature reflects the balance between interfacial energetics and entropic frustration [49], so the data in Figure 2.2 can be used to identify the types of interactions at each boundary. We first discuss the data for annealing at 200 °C, where parallel domain orientations are favored near $t = (n + 0.5)L_0$, while perpendicular domain orientations are favored near $t = nL_0$. These outcomes are consistent with *asymmetric wetting* at the boundaries, meaning different blocks are energetically preferred at each interface. The rationale for this conclusion was presented elsewhere [49]: Film thicknesses of $t = (n + 0.5)L_0$ are commensurate with asymmetric wetting, so parallel lamellae can assemble between the air and substrate interfaces without stretching or compressing the chains. When the initial (as-cast) film thickness deviates from $t = (n + 0.5)L_0$, then the system can relieve frustration by separating into regions of commensurate thickness, i.e., forming islands or holes at the surface of the film. These surface relief structures are characterized by a topography of L_0 and their area density will increase with the extent of incommensurability [22, 101, 104]. In the present system, we observe low densities of islands (height = L_0) and holes (depth = L_0) for small degrees of incommensurability (see Figure 2.3). However, when the initial film thickness is near $t = nL_0$, which is highly incommensurate with asymmetric wetting, then the lamellae adopt a perpendicular orientation with respect to the free surface. It is likely that kinetic [49, 52, 105] or thermodynamic [106, 107] barriers inhibit island and hole growth at a high area density, so the domains change their orientation to relieve frustration. The stabilization of perpendicular PS-PMMA domains on brushed substrates is well-documented in many literature studies [44, 47, 49], but this behavior is observed only when there is a weak tendency to form wetting layers [49].

The data reported in Figure 2.2b and Figure 2.3 are consistent with asymmetric wetting, so we now discuss which block is preferred at each interface. At 200 °C, PS

has a slightly lower surface energy than PMMA (by less than 0.5 mN/m) [42,97]. All samples with parallel lamellae exhibited a water contact angle of $(90 \pm 1)^\circ$, confirming the formation of a PS wetting layer at the air interface (see Table 2.4). Therefore, since PS is (weakly) preferred at the top of the film, we conclude that PMMA is adsorbing at the brushed substrate. Many studies have shown that PMMA is strongly preferred over PS on an oxidized silicon wafer [10, 42, 43], but the P(S-*r*-MMA) brushes are designed to screen those interactions and generate a “neutral” substrate [10, 61, 71]. However, the PMMA segments are evidently penetrating the brushes and sensing the underlying oxide, even though the brushes have a higher content of styrene than methyl methacrylate monomer. This behavior may be a consequence of the low-to-moderate brush grafting density. We note that another work examined PS-PMMA lamellar ordering on *pure PS brushes*, and those authors detected perpendicular domains at the surface of the film when Σ was low (ca. 0.15 nm^{-2}) [88], which is consistent with our observation that substrate neutrality is a function of both the chemistry and grafting density of the brushes. Similar behavior is predicted in simulations of lamellar block copolymers on random copolymer brushes [84, 85].

We now consider the data for 240 °C. It is known that PS and PMMA have the same surface tensions at temperatures above 220 °C [45, 49, 53], so the polymer/air interface is neutral in our studies. [101] If the brushed substrate is selective to PMMA at 240 °C, then parallel lamellae are anticipated at $t = nL_0$ and $t = (n + 0.5)L_0$, while a high density of surface relief structures is anticipated at $t = (n \pm 0.25)L_0$ [101]. The experimental outcomes are inconsistent with these expectations: A perpendicular domain orientation is observed for nearly all film thicknesses and brush grafting densities (Figure 2.2a), and there are no conditions that drive formation of islands and holes. Based on these observations, one could conclude that the brushed substrate is neutral to PS-PMMA at 240 °C [97]. However, the brushes can still be “penetrated”

by the copolymer at high temperature, and PMMA is always preferred over PS at an oxidized substrate.

We propose that the brushed substrate is weakly preferential to PMMA at 240 °C, and the strength of these interactions is enhanced as Σ is reduced. These statements are supported by data in Figure 2.2a and the Appendix A Figure A.5: A few regions of parallel lamellae are detected in ultrathin films ($t/L_0 < 1$) on brushes with a low grafting density ($\Sigma < 0.4 \text{ nm}^{-2}$), and some of these domains exhibit hexagonal perforations that are characteristic of preferential interactions at the copolymer/substrate interface [87, 102, 103]. We note that perpendicular PS-PMMA lamellae have been reported in other studies with weakly preferential interfaces [80, 108]. In the following sections, we discuss the consequences of substrate interactions on in-plane and out-plane defectivity. We propose that lamellae can deform near the “nearly neutral” brushed substrate to create a more favorable interface and stabilize the perpendicular domain orientation.

2.3.3 Lateral Order.

We examined lateral domain ordering *at the top of the film* as a function of normalized block copolymer film thickness (t/L_0) and brush grafting density (Σ) using AFM and SEM. These studies are restricted to annealing at 240 °C, as processing at a lower temperature failed to drive perpendicular ordering over a broad range of film thicknesses. The normalized orientational correlation length (ζ/L_0) was calculated from each micrograph with the algorithm described in the Experimental Procedures and reported elsewhere [73, 74]. Representative images are included in Figure 2.4 for a few values of t/L_0 and Σ , where each grain is colored according to its in-plane orientation. It is clear by visual inspection that ordering is improved with increasing film thickness. Figure 2.5 summarizes ζ/L_0 as a function of t/L_0 and Σ , and we

observe two trends: First, for a fixed block copolymer film thickness, the orientational

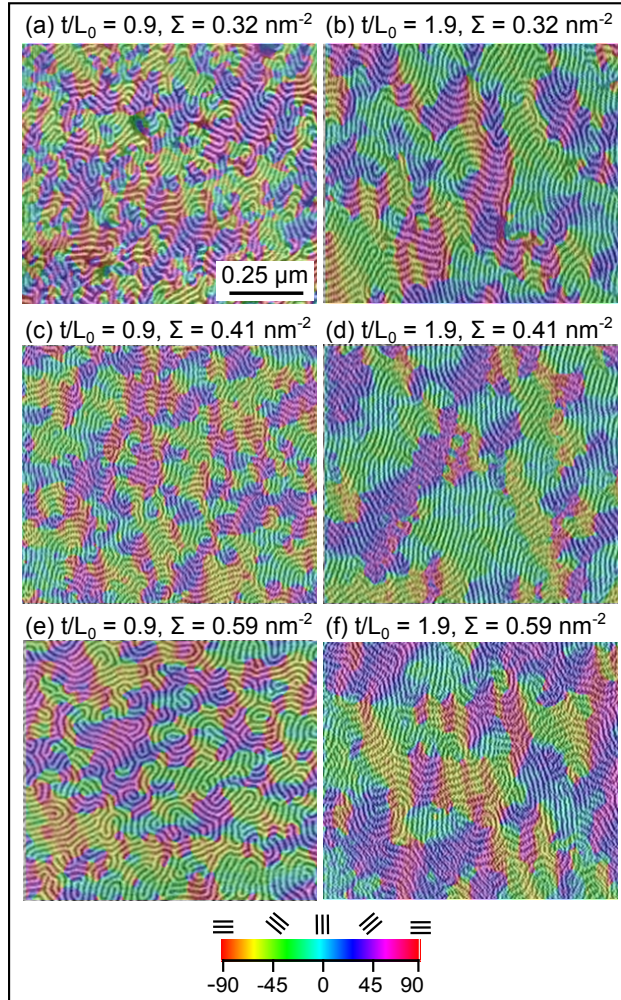


Figure 2.4: Microscopy measurements for different film thicknesses (t/L_0) and brush grafting densities (Σ). The grains in each image are colored according to their in-plane orientation.

correlation length generally increases with brush grafting density, although there is some overlap in the ζ values for brushes with similar Σ . To our knowledge, this is the first example where lateral ordering is correlated to systematic variations in the grafting density of an underlying brush. Second, for a fixed grafting density, the orientational correlation length increases with block copolymer film thickness. The latter trend is well-described with the simple scaling $\zeta \propto t^n$, and Table 2.5 summarizes

the exponent n for each Σ . A few studies have reported similar improvements

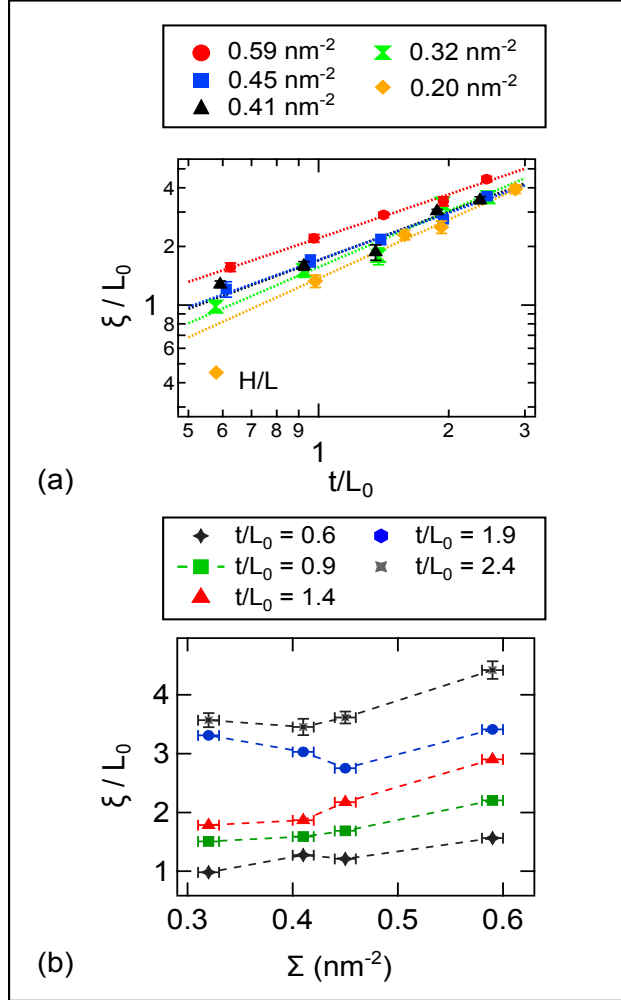


Figure 2.5: (a) OCL (ζ/L_0) at the top of the film as a function of film thickness (t/L_0). Lines are best-fit to a power law $\zeta \propto t^n$. (b) OCL (ζ/L_0) at the top of the film as a function of brush grafting density (Σ).

in lateral domain order with increasing film thickness [79, 80, 109], and the scaling exponent reported for PS-PMMA lamellae on rough indium tin oxide substrates [79] or brushed substrates [80] is $n \approx 0.42$ at 200°C. For our system, n increases from approximately 0.75 to 1 as Σ decreases from 0.6 nm⁻² to 0.2 nm⁻² (at 240°C). We propose that the scaling exponent n reflects how strongly the substrate “pins” domains and traps in-plane defects. The pinning effect decays with distance from the substrate,

Table 2.5: Scaling exponent n for OCL (ζ) as a function of film thickness, i.e., $\zeta \propto t^n$. Exponent is reported for each brush grafting density Σ .

Brush	Σ (nm ⁻²)	n
55% S	0.59 ± 0.01	0.75 ± 0.06
55% S	0.45 ± 0.01	0.80 ± 0.06
55% S	0.41 ± 0.01	0.83 ± 0.11
55% S	0.32 ± 0.01	0.97 ± 0.15
59% S	0.20 ± 0.01	1.00 ± 0.07

so a thicker film exhibits better order at the top than a thinner film. Pinning is minimized in our system by increasing Σ , so we conclude that higher grafting densities are more effective at screening interactions with the substrate.

The data in Figure 2.5 demonstrate that the influence of the substrate decays with distance, so it is likely that order changes throughout the thickness of the film. Depth-dependent structures have been reported in studies of PS-PMMA lamellae on crosslinkable neutral coatings [110]: the authors measured lateral order at the top and bottom of a thick film, and they demonstrated that ordering is significantly improved at the free surface compared with the substrate.

2.3.4 GISAXS.

We evaluated out-of-plane order (domain orientations) with GISAXS measurements [49, 111]. Figure 2.6 includes representative GISAXS data for PS-PMMA films with normalized thicknesses of $t/L_0 = 1$ and $t/L_0 = 2.5$ on brushes with $\Sigma = 0.32$ nm⁻², 0.45 nm⁻², and 0.59 nm⁻². The patterns contain several features that offer qualitative insight into the extent of in-plane and out-of-plane disorder. For example, the in-plane line shape of the first-order peak (along the 2Θ axis) is broader in thin films compared with thick films. Line shape is inversely related to orientational correlation length, so these data demonstrate that confinement suppresses lateral order, an

outcome that is consistent with the previously discussed microscopy data. Appendix A Figure A.7 includes a summary of line shape as a function of film thickness to illustrate this point. The GISAXS data also exhibit partial Debye-Scherrer rings that are associated with misoriented domains [49, 112], meaning lamellae that are tilted relative to the normal axis. Finally, the lamellar form factor is “smeared” due to out-of-plane disorder when the brush is very thin. The following paragraphs present two approaches for GISAXS data analysis that can quantify the out-of-plane structure of lamellar copolymers. The GISAXS patterns exhibit a strong first-order peak

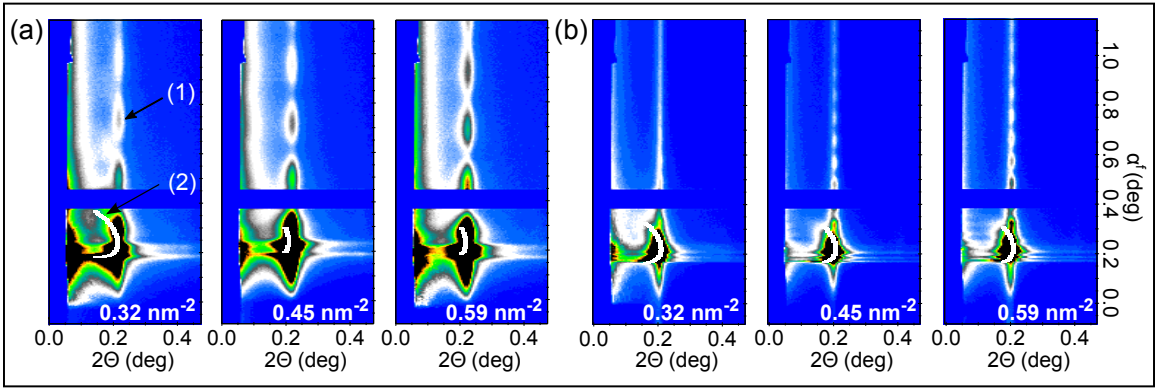


Figure 2.6: GISAXS patterns for films with thicknesses (a) $t/L_0 \simeq 1$; and (b) $t/L_0 \simeq 2.5$. ($\alpha^i = 0.22^\circ$). Arrows (1) and (2) indicate the scattering rod and Debye-Scherrer rings, respectively, at the first-order peak ($2\Theta \approx 0.21^\circ$).

at $2\Theta = 0.21^\circ$, so the in-plane scattering vector is $q_y \simeq 4\pi\Theta/\lambda = 0.136 \text{ nm}^{-1}$ and the average lattice period is $L_0 = 2\pi/q_y = 46 \text{ nm}$. The intensity of the first-order peak along the out-of-plane axis is produced by the intersection of the in-plane structure factor with the lamellar form factor [111]. This “scattering rod” is marked by the arrow in Figure 2.6 (feature 1). Therefore, by modeling this intensity profile, one can extract a distribution of domain orientations throughout the depth of the film. The GISAXS intensity is modeled using the distorted-wave Born approximation

(DWBA) [96, 111, 113],

$$\begin{aligned}
I(2\Theta, \alpha^f) = & \langle \langle | \sum_{j=2}^3 \Delta\rho_j T_j^f T_j^i F_j(q_y, q_{z,j}^1) + \Delta\rho_j R_j^f T_j^i F_j(q_y, q_{z,j}^2) \\
& + \Delta\rho_j T_j^f R_j^i F_j(q_y, q_{z,j}^3) + \Delta\rho_j R_j^f R_j^i F_j(q_y, q_{z,j}^4) |^2 \rangle_{PD_\gamma} \rangle_{\Delta\alpha^i} * K(2\Theta, \alpha^f), \quad (2.3)
\end{aligned}$$

with out-of-plane scattering vectors

$$k_{z,j}^i = -k_0 \{ \sin^2 \alpha^i - \sin^2 \alpha_{c,j} \}^{0.5}, \quad (2.4)$$

$$k_{z,j}^f = +k_0 \{ \sin^2 \alpha^f - \sin^2 \alpha_{c,j} \}^{0.5}, \quad (2.5)$$

$$q_{z,j}^1 = +k_{z,j}^f - k_{z,j}^i, \quad (2.6)$$

$$q_{z,j}^2 = -k_{z,j}^f - k_{z,j}^i, \quad (2.7)$$

$$q_{z,j}^3 = +k_{z,j}^f + k_{z,j}^i, \text{ and} \quad (2.8)$$

$$q_{z,j}^4 = -k_{z,j}^f + k_{z,j}^i. \quad (2.9)$$

The summation over j in Equation (2.3) accounts for the scattering from different layers with distinct electron density contrasts of $\Delta\rho_j$. Layer $j = 2$ describes a ‘‘bumpy’’ film surface where the PMMA domains are slightly taller than PS domains (scattering contrast from air/PMMA) [49]. Layer $j = 3$ describes the interior film structure, meaning the height and orientation of lamellar domains (scattering contrast from PS/PMMA). This notation for layer indexing comes from the Parratt recursions [93], where layers 1, 4, and 5 are vacuum, native oxide, and bulk silicon, respectively. There is no off-specular scattering from any of these layers, i.e., $\Delta\rho_j = 0$, so they do not appear in the DWBA formalism. The transmission and reflection coefficients for incoming (‘‘ i ’’) and outgoing (‘‘ f ’’) waves in each layer j are $T_j^f(\alpha^f)$, $T_j^i(\alpha^i)$, $R_j^f(\alpha^f)$, and $R_j^i(\alpha^i)$. The scattering potential for the lamellar nanostructures in each layer j

is

$$F_j(q_y, q_{z,j}^m) = S(q_y)P_j(q_y, q_{z,j}^m), \quad (2.10)$$

where $S(q_y) = \delta(q_y - 2\pi n/L_0)$ is the 1D structure factor and $P_j(q_y, q_{z,j}^m)$ is the lamellar form factor. The predicted GISAXS intensity reflects the average over lamellar domain heights and orientations in layer $j = 3$ (denoted by the subscript PD_γ), which is implemented with the local monodisperse approximation [96, 114], and includes corrections for incident angle divergence due to wafer curvature (denoted by the subscript $\Delta\alpha^i$). The scattering vectors defined by Equations (2.4)-(2.9) for a layer j are a function of the critical angle $\alpha_{c,j}$ and the wave vector modulus $k_0 = 2\pi/\lambda$. Finally, the DWBA intensity is convolved with a Gaussian resolution function $K(2\Theta, \alpha^f)$ having a standard deviation of 0.0045° (limited by the detector pixel size).

The aim of DWBA analysis is to fit a function for the scattering potential to experimental data, thereby determining the out-of-plane domain orientation distribution. All other terms in the DWBA model are calculated through independent measurements. For example, the incident angle spread is measured with rocking curves as described in the Experimental Procedures, and a representative outcome is reported in Figure 2.7(a) with the best-fit to Equation (2.1). The transmission and reflection coefficients in each layer are determined by fitting XRR measurements to the Parratt recursions, which was also described in the Experimental Procedures, and an example of these data is included in Figure 2.7(b). The scattering contrast for each layer is fixed based on the electron densities of each material [93].

To compare GISAXS data with the DWBA model, the diffuse background was subtracted from the first-order peak by fitting a polynomial baseline to each row of the spectra (along the 2Θ axis). A side-by-side comparison of an original and corrected data set is included in Figure 2.7(c) and Figure 2.7(d), respectively, for the left

and right side of the beam stop (mirror images). We then integrated the first-order peak along the 2Θ axis to produce a line profile $I(\alpha^f)$. Examples of these spectra are included in Figure 2.8(a-b). The next step for data analysis is to propose a model for the scattering potential, or specifically, the distribution of lamellar domain orientations. The surface structure in layer $j = 2$ is modeled as rectangular protrusions of

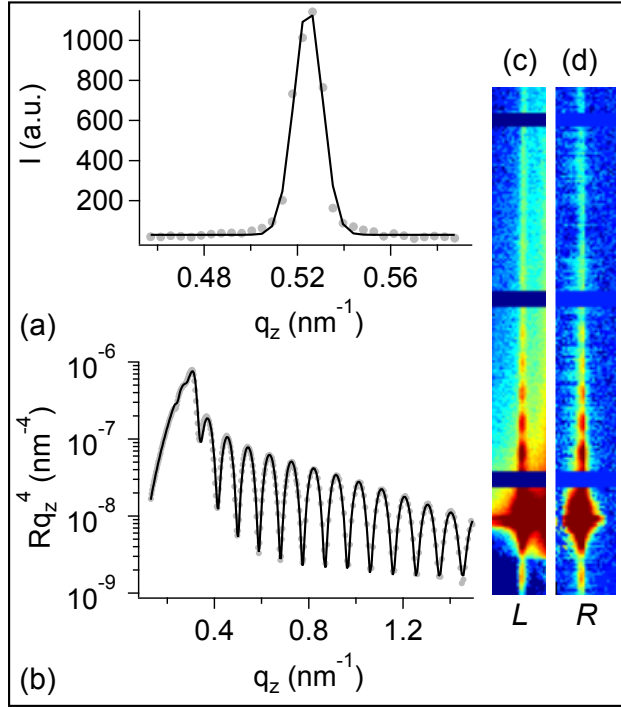


Figure 2.7: (a) Rocking curve and (b) reflectivity for a PS-PMMA film thickness of $t/L_0 = 1.5$ brush ($\Sigma = 0.59 \text{ nm}^{-2}$) (c) and (d) show the first-order peak before and after background correction, respectively.

PMMA with height h_{surf} and width $2w$, so the form factor is

$$\begin{aligned}
 P_2(q_y, q_{z,2}^m) &= \int_{-h_{surf}}^0 \int_{-w}^w \exp[-i(q_y \cdot y + q_{z,2}^m \cdot z)] dy dz & (2.11) \\
 &= 2i \frac{\sin[q_y w]}{q_y q_{z,2}^m} (1 - \exp[iq_{z,2}^m h_{surf}]).
 \end{aligned}$$

The composition of this PS-PMMA block copolymer is 53% styrene and $L_0 = 46$

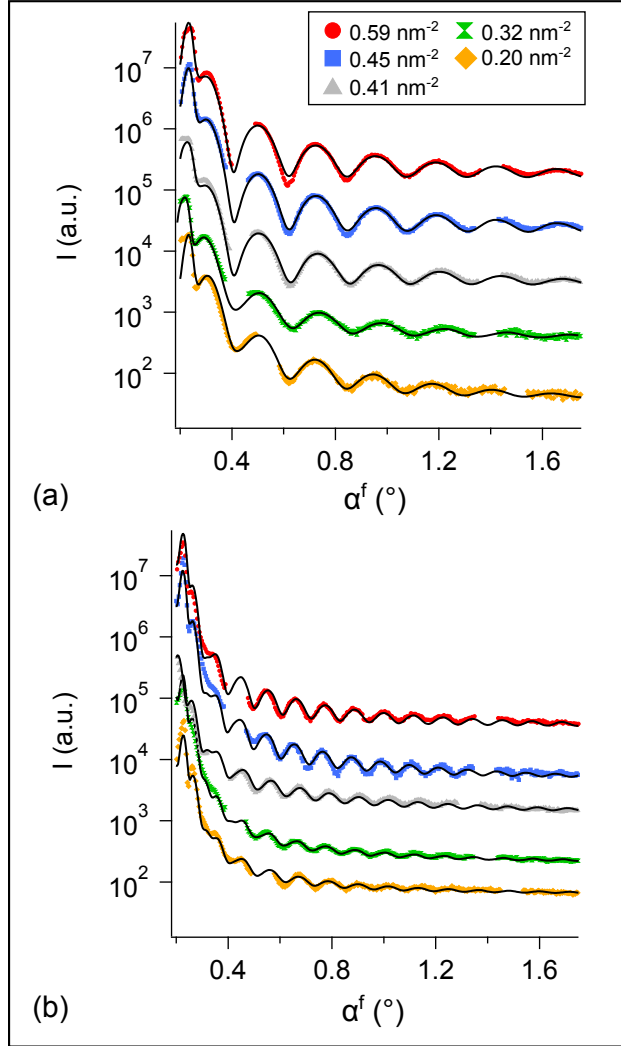


Figure 2.8: First-order diffraction rod as a function of brush grafting density for (a) $t/L_0 = 1$ and (b) $t/L_0 = 2$. Solid black line is the best-fit to the DWBA model ($\alpha^i \approx 0.22^\circ$).

nm, so the width of a PMMA domain is fixed at $2w = 22$ nm. The protrusion height h_{surf} is an adjustable parameter for optimization. We do not fit a dimension along the x -axis because the lamellar contour length in the fingerprint pattern is too small to detect for our range of $\alpha_f (< 2^\circ)$.

The PMMA domains in layer $j = 3$ are modeled as rectangular nanostructures

with height h and width $2w = 22$ nm, where the domain orientation γ can vary with respect to the z -axis. We use a Gaussian probability density to describe the distribution of domain orientations. The Gaussian function is centered at $\gamma = 0$, meaning perpendicular domains are most probable, and the standard deviation is σ_γ . Figure 2.9(a) illustrates the rectangular nanostructures, tilted orientations, and probability density function. The form factor for the misoriented lamellar domains is

$$\begin{aligned}
 P_j(q_y, q_{z,3}^m) &= \int_{-h}^{-h_{surf}} \int_{-w+z \cdot \tan \gamma}^{w+z \cdot \tan \gamma} \exp \left\{ -i (q_y \cdot y + q_{z,3}^m \cdot z) \right\} dy dz & (2.12) \\
 &\simeq \frac{2 \sin [q_y w] \left(i - i \cos [h \{ q_{z,3}^m + q_y \tan[\gamma] \}] + \sin [h \{ q_{z,3}^m + q_y \tan[\gamma] \}] \right)}{q_y (q_{z,3}^m + q_y \tan[\gamma])}.
 \end{aligned}$$

The adjustable parameters for optimization are h and σ_γ . This model for out-of-plane disorder is rather simple and does not account for the fact that domains may bend in addition to tilting. However, capturing domain curvature requires a form factor model with additional adjustable parameters, and increased model complexity will produce many degenerate solutions when experimental data are limited to a single well-defined scattering rod. We do not observe strong higher-order scattering rods along the q_y axis because the lateral ordering is poor, so the GISAXS intensity rapidly decays along the q_y axis [113], and the positions of even-order Bragg peaks ($q_y = 2\pi n/L_0$, $n = 2, 4, \dots$) coincide with minima in the lamellar form factor (see Figure 2.6, and Appendix A Figure A.8). For each sample, GISAXS data were acquired at two angles of incidence ($\alpha^i \approx 0.2^\circ$ and 0.22°), and each background-corrected spectra $I(\alpha^f)$ was independently analyzed with the DWBA model. Examples of best-fit results through nonlinear regression [115] are included in Figure 2.8(a-b). The optimal value of h_{surf} was always very small (ca. 0.2 nm), so the scattering from layer $j = 2$ produces a nearly flat profile along the α^f axis. This effect is similar to

adding a constant intensity offset in the objective function. The optimal value of h

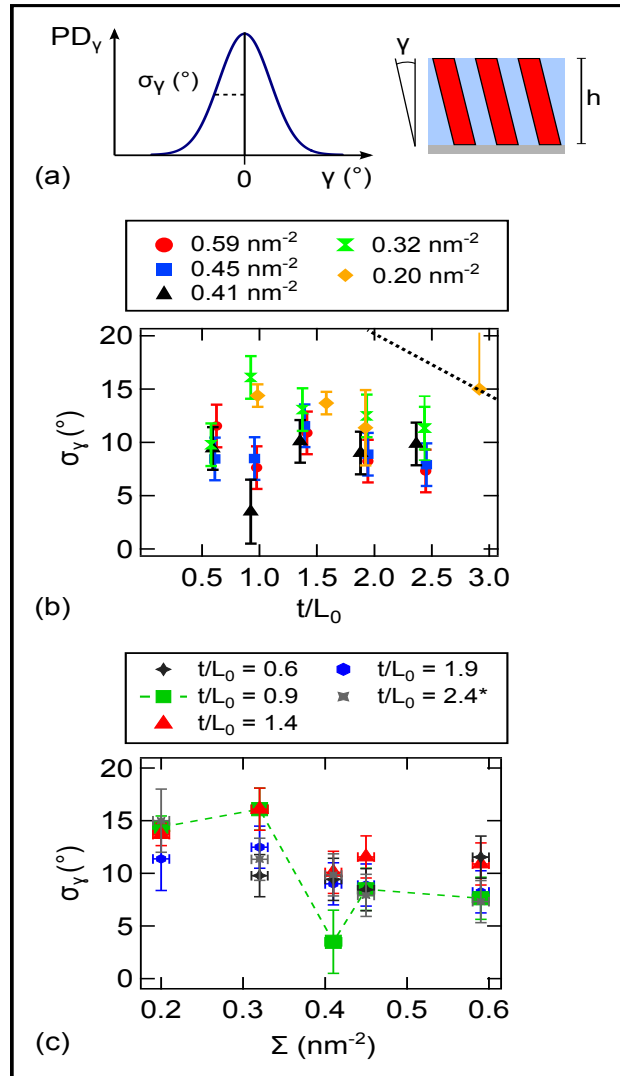


Figure 2.9: (a) Domain probability density (σ_γ) of tilt angles. (b) σ_γ as a function of film thickness t/L_0 . Dashed line marks the resolution limit for this method of analysis. (c) σ_γ as a function of brush grafting density Σ .

was typically a few nanometers less than the total film thickness measured by XRR. This outcome is expected because the total film thickness reflects both the PS-PMMA film and underlying brush.

The optimal values of σ_γ are reported in Figure 2.9 as a function of normalized film thickness and brush grafting density. The average values and uncertainties were

calculated from fits at both angles of incidence, and the dashed line in part b) denotes the resolution limit for the DWBA model. (The resolution limit is determined by the ability to distinguish the periodic $I(\alpha^f)$ oscillations, where the period in q_z -space is inversely related to domain height. The oscillations in thick films with “tall” domains are smeared when σ_γ exceeds approximately 15° . This smearing is observed in Figures 2.6(b) and 2.8(b) when Σ is low.) All samples are characterized by a population of misoriented domains. The dependence of σ_γ on thickness and grafting density is rather complex: In ultrathin films ($t/L_0 = 0.6$) and thick films ($t/L_0 > 1.9$), σ_γ is independent of Σ and approximately equal to 10° for both data sets. When $t/L_0 = 0.9$, $\sigma_\gamma \approx 8^\circ$ when $\Sigma > 0.4 \text{ nm}^{-2}$ and $\sigma_\gamma \approx 15^\circ$ when $\Sigma < 0.4 \text{ nm}^{-2}$. Similar behavior is observed when $t/L_0 = 1.4$, where $\sigma_\gamma \approx 10^\circ$ when $\Sigma > 0.4 \text{ nm}^{-2}$ and $\sigma_\gamma \approx 15^\circ$ when $\Sigma < 0.4 \text{ nm}^{-2}$. We will propose an explanation for these trends in a later section of this discussion; for now, we note that the maximum “disorder” is observed in samples where Σ of the underlying brush is low. It is challenging to calculate domain orientations from GISAXS data using the DWBA framework, because this method requires rocking curves, XRR, and a complex scattering theory to build the objective function for regression analysis. Therefore, we compared the DWBA model with a simple approach that is based on analysis of partial powder rings. Referring back to Figure 2.6, each GISAXS pattern exhibits a partial “Debye-Scherrer” powder ring (labeled as feature 2) that is characteristic of misoriented domains [49, 112]. The trajectory of these partial rings in $(2\Theta, \alpha_f)$ space was used to calculate the range of misorientation angles through a straightforward procedure [49]: First, the scattering vector for misoriented lamellar domains is defined in terms of γ

$$\vec{q} = \{q_y, q_z\} = \left\{ \frac{2\pi}{L_0}, 0 \right\} \cdot M_{rot}(\gamma) = \left\{ \frac{2\pi}{L_0} \cos[\gamma], -\frac{2\pi}{L_0} \sin[\gamma] \right\}. \quad (2.13)$$

The function $M_{rot}(\gamma)$ is a 2D rotation matrix in the (y, z) plane. Second, the scattering

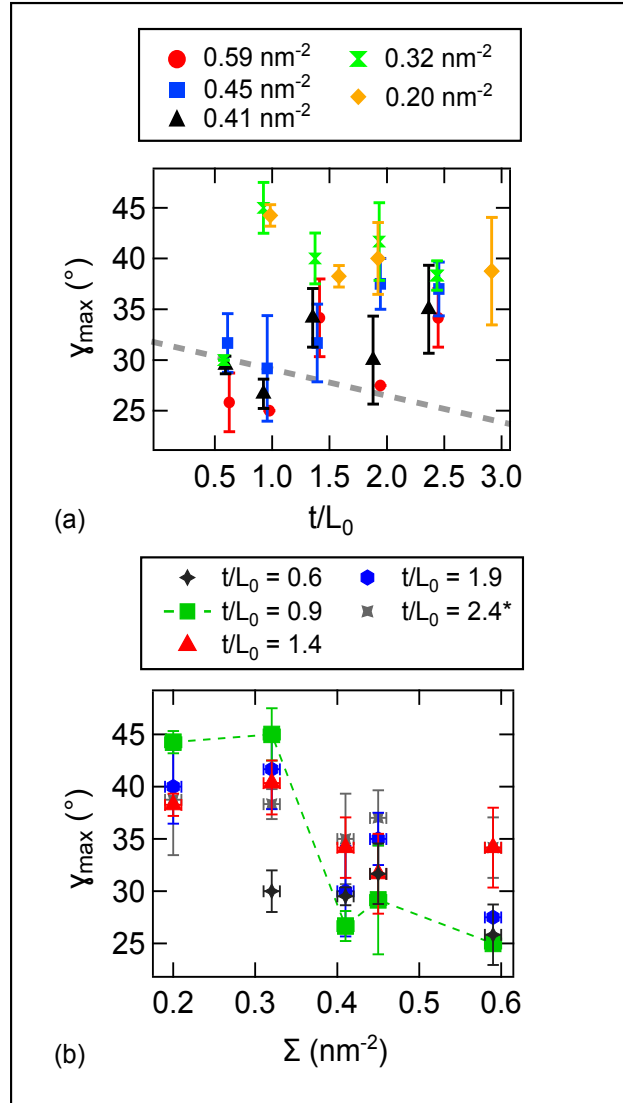


Figure 2.10: (a) γ_{max} as a function of normalized film thickness t/L_0 . Dashed line marks the resolution limit. (b) γ_{max} as a function of brush grafting density Σ .

vector is calculated for the range of angles spanning $\pm\gamma_{max}$, and the corresponding

scattering angles (in radians) are determined from Equations (2.14)-(2.15):

$$\alpha^f = \arcsin \sqrt{\sin^2[\alpha^i] + \left(\frac{q_z^2 \mp 2q_z k_0 \sqrt{\sin^2[\alpha^i] - \sin^2[\alpha_{c,3}]} }{k_0^2} \right)} \text{ and} \quad (2.14)$$

$$2\Theta \simeq q_y/k_0. \quad (2.15)$$

The “ \mp ” term in Equation (2.14) reflects the different scattering events that are possible in a GISAXS experiment, where the “ $-$ ” term is the solution to Equations (2.6) and (2.7), and the “ $+$ ” term is the solution to Equations (2.8) and (2.9). Finally, the γ -range is refined until the predicted trajectory matches the experimental data. (The trajectory is truncated when the intensity along the partial ring drops to 20% above the background level.) Examples of these comparisons are included in Figure 2.6. This model does not make assumptions about the shape of domains, so it can cap-

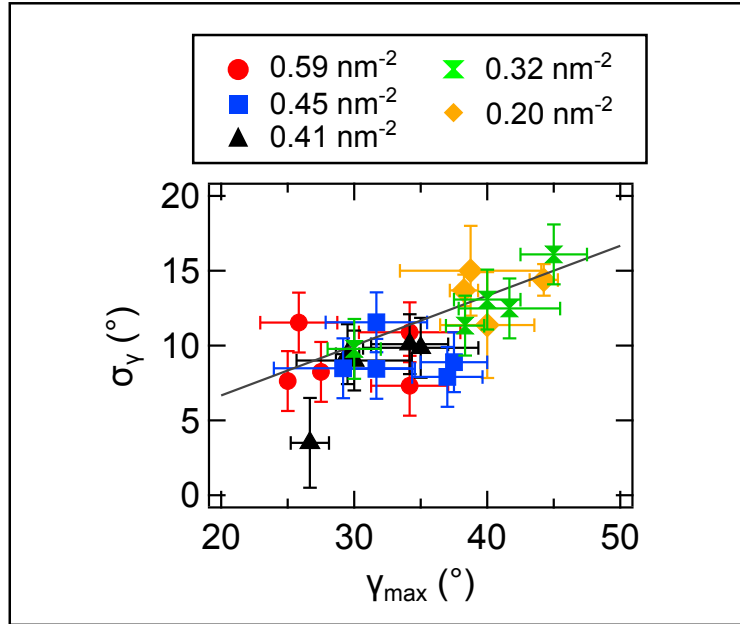


Figure 2.11: Comparison of DWBA modeling (σ_γ) and contour analysis (γ_{max}) The solid line marks $3\sigma_\gamma = \gamma_{max}$.

ture lamellar bending or uniform tilting, but it does imply that neighboring lamellar

segments have the same orientation (locally monodisperse). Figure 2.10(a) summarizes γ_{max} as a function of normalized PS-PMMA film thickness and brush thickness based on an average for $\alpha^i = 0.2^\circ$, 0.22° and 0.24° (error bars denote ± 1 standard deviation). The dashed line marks the resolution limit for this method of analysis, which is a consequence of broad line shapes in ultrathin films that obscure the partial rings (Appendix A Figure A.7). Significantly, this simple approach for interpretation of GISAXS data captured the same trends predicted by rigorous DWBA modeling, such as the greatest extent of out-of-plane disorder when $t/L_0 = 0.9$ and $\Sigma < 0.4 \text{ nm}^{-2}$. Furthermore, the two methods of data analysis are reconciled by noting that $\gamma_{max} \approx 3\sigma_\gamma$, which is expected for distributions that follow Gaussian statistics (Figure 2.11). Therefore, we propose that out-of-plane disorder can be evaluated by mapping the trajectory of partial Debye-Scherrer rings.

2.3.5 Physics of Out-of-Plane Disorder.

There are very few literature studies that consider out-of-plane disorder in thin films of perpendicular cylindrical or lamellar domains, so the underlying physics that drive this behavior are not fully understood. One work proposed that cylindrical domains will tilt in response to the strain field at dislocation or disclination cores [83]. The lamellar “fingerprint” patterns in Figure 2.4 are characterized by high densities of topological defects, but samples with the best in-plane order (measured at the free surface) do not show improvements in out-of-plane order, so it is unlikely that similar effects are dominant here. Other works have proposed that preferential interactions at the interfaces can deform the domains [49, 70, 86, 87, 116]. We used microscopy measurements to establish that PMMA is weakly preferred at the substrate, which we attribute to the low/moderate brush grafting densities [49, 88]. Therefore, we propose that domain bending and tilting is induced by adsorbed PMMA at the substrate

interface. The fact that large populations of misoriented domains are detected in

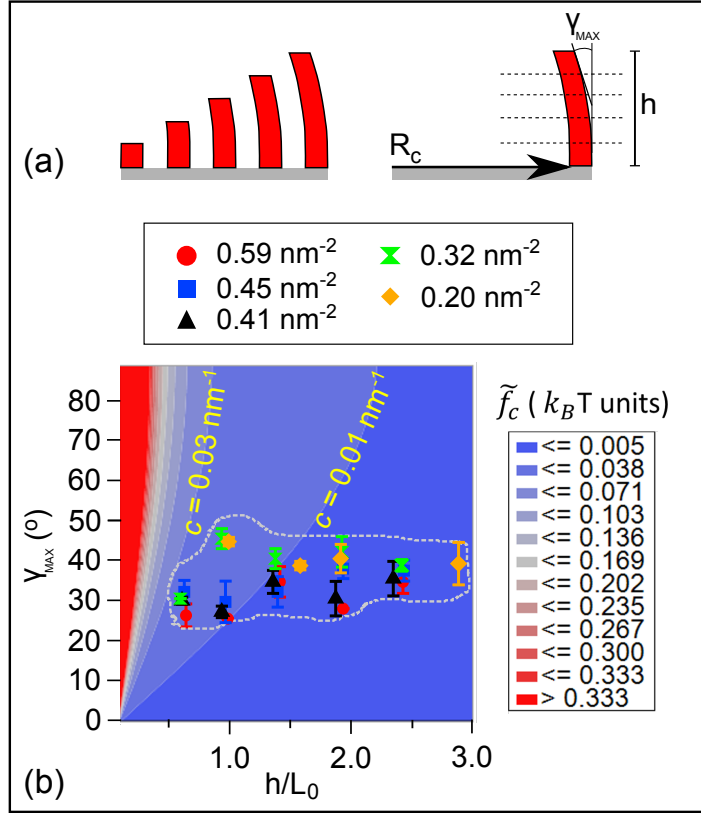


Figure 2.12: (a) For fixed bending curvature, γ_{max} increases with film thickness. (b) Free energy penalty (per chain) for domain curvature.

GISAXS suggests the bending energies are very low [117, 118]. To underline this point, we estimate the free energy penalty per chain (\tilde{f}_c) for deforming a lamellar PS-PMMA domain with constant curvature $c = 1/R_c$ [117, 119].

$$\frac{\tilde{f}_c}{k_B T} = \frac{\pi^2}{2048} \frac{L_0^4}{N a^2} c^2, \quad (2.16)$$

where k_B is the Boltzmann constant, T is annealing temperature, $L_0 = 46 \text{ nm}$ is the lamellar periodicity, $N = 978$ is the degree of polymerization, and $a = 0.66 \text{ nm}$ is the monomer segment length. This model was derived for strongly segregated domains

in the low curvature limit, and assumes that (1) end segments do not penetrate the adjacent domains, and (2) deformations from domain curvature and inhomogeneous domain thicknesses are independent. To compare the predicted curvature penalty with GISAXS measurements, we calculate the maximum misorientation angle for a lamellar domain that is bent with Gaussian curvature, i.e., $\gamma_{max} = \arcsin[c \cdot h]$. Figure 2.12(a) illustrates the relationship between γ_{max} , h , and c : When c is fixed, then γ_{max} increases with h .

Figure 2.12(b) summarizes \tilde{f}_c as a function of γ_{max} and h (units of $k_B T$). We include as an overlay the data from Figure 2.10a, and the dashed curve is a guide to the eye (enclosing the experimental outcomes). We suggest that bending of domains could allow for a more favorable interface with a slightly preferential substrate because the curvature penalties could be offset by a reduction in interfacial energy. We used microscopy at the free surface (Figure 2.5) to demonstrate that ordering in thicker films is less sensitive to Σ of the underlying brush, as the influence of the substrate decays with distance into the film. Out-of-plane order in thick films is similarly insensitive to Σ , as bending to a high γ_{max} costs little energy ($< 0.005k_B T$). When film thickness is reduced, substrate pinning is much stronger, and the domain curvature must increase to maintain the same deformation angle. The competition between domain bending and preferential wetting is more evident in this limit: For example, at $t/L_0 \approx 0.9$, there are two groupings of data that correspond with $\Sigma < 0.4 \text{ nm}^{-2}$ and $\Sigma > 0.4 \text{ nm}^{-2}$. Using equation 2.16, these data suggest that $c \sim 0.011 \text{ nm}^{-1}$ and $\tilde{f}_c \sim 0.006k_B T$ when Σ is low, while $c \sim 0.018 \text{ nm}^{-1}$ and $\tilde{f}_c \sim 0.017k_B T$ when Σ is high. In ultrathin films ($t/L_0 \approx 0.6$), the data for all $\Sigma \geq 0.32 \text{ nm}^{-2}$ converge and are consistent with $c \sim 0.019 \text{ nm}^{-1}$ and $\tilde{f}_c \sim 0.018k_B T$. The apparent threshold for deformations is around $c \sim 0.02 \text{ nm}^{-1}$ for the block copolymer and brushes employed in these studies. In the ultrathin film limit, deformations to a high angle are

unfavorable, so the system cannot satisfy the preference for PMMA at the substrate when Σ is low. This explains why microscopy detects an order-order transition to perforated lamellae along with patches of parallel lamellae for these samples (Figure 2.2 and Appendix A Figure A.5).

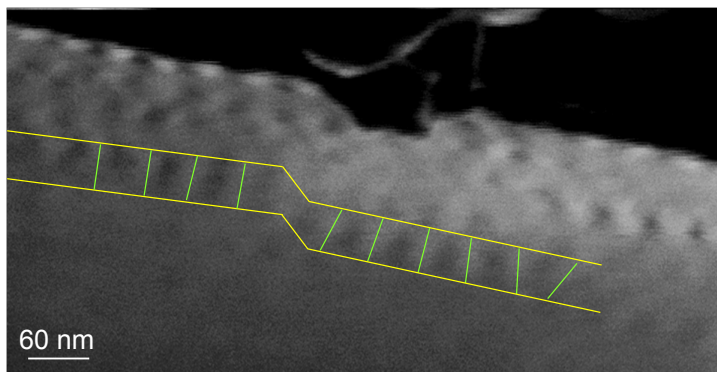


Figure 2.13: Cross-sectional SEM for $t/L_0 = 1.4$ and $\Sigma = 0.45 \text{ nm}^{-2}$. Horizontal yellow lines denote the top and bottom interfaces, while vertical green lines denote the approximate domain orientation.

Arguments based solely on domain curvature neglect strains that might accompany bending, such as compression or extension of chains [119] (For small strains ($< 10\%$), the free energy penalty per chain ranges from 0.01 up to 0.1 (in units of $k_B T$). This is estimated based on the models in reference [118]), and more rigorous modeling is needed to predict conformations and energetics at a preferential interface [84, 85, 87]. The aim of this discussion is to offer a simple physical explanation for the observed behavior, and demonstrate that a weak preference for one block at the substrate could be accommodated by bending the domains. As a related point, this analysis suggests that energies associated with out-of-plane defects are low, so there is little thermodynamic drive to “straighten out” a deformed domain. This suggests that out-of-plane defects are difficult to remove through thermal annealing, particularly in high molecular weight copolymers that exhibit slow ordering dynamics [49, 52, 105].

Lastly, we note that tilted domains can be detected in cross-sectional microscopy, but it is difficult to quantify their orientation distributions. We include such data in Figure 2.13 and the Appendix A Figures A.9-A.11. Sample preparation is challenging for a non-expert, and more importantly, it is difficult to find many regions in a poorly ordered fingerprint pattern where the in-plane lamellar orientation is normal to the cut.

2.4 Conclusions

Using surface microscopy and GISAXS, we examined in-plane and out-of-plane order in thin films of lamellar PS-PMMA copolymers ($L_0 = 46$ nm) on brushed P(S-*r*-MMA) substrates. The principal experimental variables discussed in this manuscript are brush grafting density Σ and normalized copolymer film thickness t/L_0 . A series of samples were prepared by annealing at 200 °C, a temperature where PS is weakly preferred over PMMA at the air interface. Through analysis of domain orientations (f_{perp}) and island/hole structures at 200 °C, we demonstrated that PMMA is preferred over PS at the brushed substrate. The remainder of the experiments were performed at 240 °C, a temperature where PS and PMMA have equal surface tensions, so the block copolymer was confined between a neutral free surface and a “nearly neutral” substrate. For a broad range of t/L_0 (0.5-2.5) and Σ (0.2-0.6 nm⁻²), we found that all films annealed at 240°C exhibited optically-flat surfaces with fingerprint patterns at the air interface. Islands or holes were not observed at any combination of t and Σ .

We quantified lateral order *at the free surface* of each film by calculating the orientational correlation length (ζ) from high resolution AFM and SEM micrographs. The scaling $\zeta \sim t^n$ described each data set (fixed Σ), which implies that lateral order is always improved as the influence of the substrate is reduced. The magnitude of ζ

for fixed t generally increased with Σ , and the exponent n increased from 0.75 to 1 as Σ decreased from 0.6 nm^{-2} to 0.2 nm^{-2} , demonstrating that brushes with higher grafting densities screen the influence of the substrate. While there are numerous experimental investigations that employ brushes as “neutral” coatings, the parameter Σ is rarely reported in the literature [10].

We examined out-of-plane order throughout the thickness of the film with GISAXS, and we described two methods of data analysis to determine the range of lamellar orientations with respect to the substrate: First, we fit the spectra using the distorted wave Born approximation to describe the GISAXS intensity. We used a form factor model based on a Gaussian distribution of lamellar orientations with a standard deviation of σ_γ . Second, we applied a simple method termed “contour analysis”. This approach plots the trajectory of the first order reflection as the lamellar structures are tilted through a maximum angle of γ_{max} , where $\gamma_{max} \approx 3\sigma_\gamma$. All films were characterized by bending or tilting of lamellar domains, where σ_γ ranged from approximately 8° to 15° , and outcomes from the two approaches are reasonably correlated. The domain orientations exhibit a non-monotonic dependence on film thickness, and the maximum value of σ_γ (or γ_{max}) was observed at film thicknesses of $t/L_0 \approx 1$ with brushes having low Σ . These data demonstrate that ordering at the free surface is not necessarily representative of the depth-dependent structure.

We propose that adsorption of PMMA at the substrate will pin in-plane topological defects and drive out-of-plane domain bending. In-plane and out-of-plane defects are both characterized by lamellar curvature, but the small entropic penalty for these deformations is likely offset by a reduction in energy at the copolymer-substrate interface. Other experimental and theoretical studies are consistent with this statement [70, 84–86, 117]. Substrate-induced defects may have severe consequences for block copolymer lithography, as the most demanding applications in the

semiconductor industry have low tolerances for errors (*i.e.*, integrated circuit manufacturing). For example, out-of-plane defects can distort the geometry and placement of nanopatterns in block copolymer lithography [83].

3 Thin film phase behavior of bottlebrush/linear polymer blends

3.1 Introduction

Bottlebrush polymers contain polymeric side-chains attached to a linear polymer backbone, and controlled polymerization techniques enable the preparation of fully grafted bottlebrush polymers with tunable backbone length, side-chain length, and side-chain composition [59, 120–123]. This synthetic tunability has motivated a number of recent studies into the potential applications of bottlebrush polymers, including drug delivery [124–126], polymer photonics [127–129], lubricants and rheology modifiers [121, 130–132], and surface coatings. [36, 58] These applications take advantage of unique aspects of bottlebrush polymers, including an extended backbone, densely grafted and flexible side-chains, and a very high entanglement molecular weight [132]. However, bottlebrush polymers are specialty materials that are difficult to synthesize in large quantities. Therefore, it is of interest to study their properties as additives in blends with low-cost, linear polymers.

A number of recent studies have focused on a related set of materials, blends of polymer coated nanoparticles with linear polymers, as detailed in recent reviews [133, 134]. Polymer-coated nanoparticles have a layer of linear polymers end-grafted to the nanoparticle surface which controls their dispersion in the melt. These studies have found that the properties of the blends are largely controlled by the areal density of the grafted polymer layer and the relative chain lengths of grafted and linear polymers. In particular, in athermal blends where the matrix and grafted chains

have the same composition, aggregation is observed when the matrix chains are much longer than the grafted chains. This phenomenon is driven by dewetting of the linear matrix chains from the grafted nanoparticle surface due to reduced entropy of mixing, similar to that observed for dewetting of linear chains from polymer brushes on planar surfaces.

Sheiko and Rubinstein et al. studied the two-dimensional conformations of individual bottlebrush polymers mixed with linear polymers of varying degree of polymerization (DP). [135] Their study focused on long bottlebrush polymers (backbone DPs in excess of 1000) with relatively short side-chains (side-chain DPs of 10) and found that conformations of the adsorbed bottlebrushes (swollen or ideal chain) were controlled by a balance of side chain wetting and backbone flexibility. These conformational changes are primarily driven by entropic effects.

In this work, we examine similar entropy-driven effects, but we focus on the dispersion and aggregation of bottlebrush polystyrene (PS) blended with linear deuterated polystyrene (dPS) in thin films. The bottlebrush polymers have short and fairly rigid backbones, so their structures resemble polymer-grafted nanoparticles. Using secondary ion mass spectroscopy (SIMS), we find that short dPS chains can wet the bottlebrush PS and stabilize its dispersion throughout the film thickness, while long dPS chains drive segregation of the bottlebrushes to the film surface and substrate. This behavior is controlled by architectural contributions to the free energy, as analogous blends of linear PS and linear dPS are fully miscible at the same annealing temperature (nearly athermal with $\chi \sim 10^{-4}$) [136, 137]. We discuss these results in terms of (1) wetting and dewetting transitions at the interface between polymer melts and brushlike surfaces and (2) the entropic preference for branched polymers relative to linear polymers at surfaces. Significantly, these studies demonstrate that certain bottlebrush polymer architectures can generate brushlike surfaces and interfaces in

any thermoplastic material through a spontaneous, entropy-driven segregation process.

3.2 Experimental Procedures

3.2.1 Materials

All reagents and solvents were purchased from commercial sources and were used as received unless otherwise noted. Styrene was passed through a column of aluminum oxide to remove inhibitors before use. 2,2'-Azobis(2-methylpropionitrile) (AIBN) was purified by recrystallization in methanol. Dichloromethane was dried over molecular sieves (4Å) Modified Grubb's catalyst (H₂IMes)(pyr)₂(Cl₂)RuCHPh [138], exo-7-oxabicyclo[2.2.1]hept-5-ene-2,3-dicarboxylic anhydride, [139] and norbornene-functionalized chain transfer agent (NB-CTA) were synthesized as previously reported. [58]. The synthesis of dPS bottlebrushes is described in the Appendix B Figure B.4.

3.2.2 Synthesis of NB-PS-CTA Macromonomers

NB-PS-CTA was prepared via reversible addition-fragmentation chain transfer (RAFT) polymerization. For the synthesis of NB-PS6K-CTA, styrene (4.84 g, 46.50 mmol), NB-CTA (101.40 mg, 0.182 mmol), and AIBN (3.40 mg, 1.82 × 10⁻² mmol) were mixed in a 100 mL of RBF, and the solution was purged by bubbling nitrogen through the solution for 30 min. The polymerization was initiated by raising the temperature to 60°C. After 11 h, the reaction flask was removed from the heat and the polymer was recovered by precipitation in methanol (0.75 g, 67.0% yield, based on the conversion of styrene). The GPC spectra are presented in the Appendix B Figure B.2.

3.2.3 P(NB-PS6K-CTA)

Bottlebrush polymers were prepared by ROMP using $(\text{H}_2\text{IMes})(\text{pyr})_2(\text{Cl})_2\text{RuCHPh}$. The macromonomers were added to a dry, 10 mL round-bottom flask charged with a stir bar. The flask was then degassed with three pump-purge cycles, and the desired amount of degassed, anhydrous dichloromethane (total macromonomer concentration was 0.02–0.05M) was added. $(\text{H}_2\text{IMes})(\text{pyr})_2(\text{Cl})_2\text{RuCHPh}$ was dissolved in degassed, anhydrous dichloromethane in a separate flask. The catalyst solution was transferred to the reaction flask containing macromonomers via cannula to initiate the polymerization and stirred at room temperature for at least 1h. The reaction was quenched by addition of ethyl vinyl ether after completion. The product was collected by precipitation in methanol dried under vacuum (95% yield, based on the conversion of NB-PS-CTA). The ^1H NMR and GPC spectra are presented in the Appendix B Figure B.1 and B.2, respectively.

3.2.4 P(NB-PS)

PS bottlebrush polymers were prepared by removing the chain transfer agent (CTA) end-group from P(NB-PS-CTA) bottlebrush polymers using an aminolysis reaction in the presence of tributylphosphine to prevent disulfide bond formation [138, 139]. The reaction was carried out in a nitrogen glovebox. P(NB-PS-CTA) was dissolved in anhydrous THF, and hexylamine (10 times the amount of CTA end-groups present on a molar basis) and tributylphosphine (equal to the amount of CTA end-groups present on a molar basis) were added successively. The reaction was stirred at room temperature, after which the solution turned from yellow to a clear, colorless solution, indicating removal of the CTA end-group. The final product

was precipitated in cold methanol and dried under vacuum. The ^1H NMR and GPC spectra are presented in the Appendix B Figure B.1 and B.2, respectively.

3.2.5 Synthesis of Deuterated Linear Polystyrene (dPS)

Linear dPS samples were synthesized by anionic polymerization [140, 141]. Styrene-d8 was polymerized from *sec*-BuLi initiator in benzene solvent and then terminated with methanol. Molecular weight was targeted by $[\textit{grams monomer}]/[\textit{moles initiator}] = MW$. Benzene, hexane, methanol, *sec*-BuCl, and Li were obtained from Aldrich; styrene-d8 was obtained from Cambridge Isotopes. *sec*-BuLi was synthesized in vacuo from *sec*-BuCl and excess Li and diluted with hexane. Styrene-d8 was distilled repeatedly from CaH_2 , Na mirror, and Bu_2Mg . Methanol was degassed. Benzene was purified by distilling repeatedly from CaH_2 , Na, and oligostyryllithium. Hexane was purified by distilling from *n*-BuLi. All reagents were encapsulated into glass ampules and affixed to polymerization reactors, which were themselves all-glass, sealed shut under vacuum, and equipped with break-seals for sequential incorporation of reagents and constrictions for removal of intermediate products. In the case of higher MW target materials (e.g., 50 kg/mol and higher) these reactors were washed with *n*-BuLi and rinsed with purified benzene prior to the polymerization. Styrene-d8 and *sec*-BuLi were mixed into benzene, and this monomer was polymerized overnight at room temperature; the following day MeOH was added to terminate the reaction. The reactor was opened, and the polymer was isolated by precipitation into unpurified methanol, filtered, and dried.

3.2.6 Instrumentation

3.2.7 Gel Permeation Chromatography (GPC)

Molecular weights and dispersities of the PS macromonomers and bottlebrush polymers were obtained using an Agilent 1200 module equipped with three PSS SDV columns in series (100, 1000, and 10000 Å pore sizes), an Agilent variable wavelength UV/vis detector, a Wyatt Technology HELEOS II multiangle laser light scattering (MALLS) detector ($\lambda = 658$ nm), and a Wyatt Technology Optilab reX RI detector. This system enables SEC with simultaneous refractive index (SEC-RI), UV/vis (SEC-UV/vis), and MALLS detection. THF was used as the mobile phase at a flow rate of 1 mL/min at 40 °C. GPC analysis of PS bottlebrushes and macromonomers is shown in the Appendix B Figure B.2.

Molecular weights and dispersities of linear deuterated polystyrene were obtained by size exclusion chromatography (SEC) using a Waters Alliance 2695 separations module equipped with three Polymer Laboratories PLgel 5 μ m mixed-C columns (300 \times 7.5 mm) in series, a Waters Model 2414 refractive index detector ($\lambda = 880$ nm), a Waters Model 2996 photodiode array detector, and a Wyatt Technology miniDAWN multiangle light scattering (MALS) detector ($\lambda = 660$ nm). THF was used as the mobile phase at a flow rate of 1 mL/min. Molecular weight values were determined by MALS analysis and were in good agreement with values from conventional RI analysis relative to monodisperse polystyrene standards. Dispersity values were taken according to RI conventional calibration results. Results are summarized in Table 3.2.

3.2.8 Nuclear Magnetic Resonance Spectroscopy (NMR)

Hydrogen NMR (^1H NMR) spectra were recorded using tetramethylsilane as internal standard in CDCl_3 on a 400 MHz Bruker multinuclear spectrometer. Samples

were placed in 5 mm o.d. tubes with a concentration of 20 mg/mL.

3.2.9 Preparation of Thin Film Blends

Linear dPS and bottlebrush PS were dissolved in toluene at a 9:1 ratio, where the typical concentration of all solids was 2–2.5 wt %. Films were prepared by spin-casting onto (100) p-type silicon substrates with 200 nm of thermal oxide. All substrates were cleaned with UV-ozone immediately prior to use (UVOCS system). Thermal annealing was conducted in a low vacuum oven (30 mTorr) at 165 °C for 2 and 7 days. An 80 nm film of deuterated polystyrene was floated on top of each sample from deionized water; this cover layer is needed to calibrate the etch depth during secondary ion mass spectrometry measurements and ensures that the instrument achieves a steady state etch rate [142].

3.2.10 Film Thickness Characterization

The thicknesses of silicon dioxide and polymer films were measured using a JA Wollam M-2000 spectroscopic ellipsometer. The ellipsometry parameters Δ and Ψ were modeled by assuming a polymer film described by the Cauchy dispersion relation $n(\lambda) = A + B/\lambda^2$, where A , B , and film thickness were regression fitting coefficients.

3.2.11 Secondary Ion Mass Spectrometry (SIMS)

The depth-dependent composition of bottlebrush polystyrene was measured with a PHI 6600 SIMS system using a focused Cs^+ primary ion beam which can ablate secondary ions having positive or negative charge. A quadrupole mass analyzer (mass resolution $m/\Delta m \sim 200$) separated the masses of ejected ions by resonant electric fields, where the user specifies the masses that are able to pass through for detection. The chamber was maintained under ultrahigh vacuum (10^{-10} Torr) by an ion pump.

The Cs⁺ ion beam size was 30 μm with 30 nA primary current and 5 keV impact energy. The beam bombarded the samples at an incident angle of 30 with respect to the surface and was rastered over an area of 500 $\mu m \times 500 \mu m$. Note that analysis of depth-dependent compositions by neutron reflectivity was unreliable, and this point is discussed in the Appendix B.

3.3 Results

Bottlebrush polymers were synthesized via a grafting through method that combines reversible addition–fragmentation chain transfer polymerization (RAFT) and ring-opening metathesis polymerization (ROMP). As shown in Figure 3.1, a norbornene-functionalized chain transfer agent (NB-CTA) was used to grow polystyrene side-chains (NB-PS-CTA), and subsequently, in the presence of a third-generation Grubbs catalyst, well-defined bottlebrush polymers P(NB-PS-CTA) were obtained. The GPC spectrum of the bottlebrush polymer shows a significant shift when compared to that of the macromonomer. The GPC spectrum of the bottlebrush polymer shows a significant shift when compared to that of the macromonomer NB-PS-CTA (see Appendix B Figure B.2). Well-defined bottlebrush polystyrenes were obtained with narrow \mathbb{D} and high ROMP conversion ($\sim 95\%$). The characteristics of the bottlebrush polymers are summarized in Table 3.1, where the subscripts “b” and “sc” denote backbone and side chain properties, respectively. These architectural parameters are also depicted in Figure 3.3.

Table 3.1: Characteristics of Bottlebrush Polystyrene

batch	$M_{n,b}(kDa)$	N_b	\mathbb{D}_b	$M_{n,sc}$	N_{sc}	\mathbb{D}_{sc}
1	8.5	90	1.17	6.4	61	1.13
2	18.0	193	1.17	6.4	61	1.16

Prior studies showed that the CTA end-groups (dodecyl chain) will induce the

formation of a coreshell structure [58]. To minimize this effect, thiol-terminated bottlebrush polymers P(NB-PS-SH) were prepared by removing the CTA end-group with an aminolysis reaction in the presence of tributylphosphine. The presence of phosphine has been shown to inhibit the formation of disulfide bonds after CTA removal [138, 139], even when exposed to air [143]. CTA removal is verified through a color change (from yellow to clear solution) and by ^1H NMR characterization (Appendix B Figure B.1). GPC analysis shows a clear shift to long retention times after CTA removal, consistent with a decrease in the total molecular weight, and the final product retains a unimodal molecular weight distribution (see Appendix B Figure B.2).

The approximate number of side-chains per unit area of the bottlebrush polymer is $\sigma \approx N_b/4\pi R_g^2 \approx 0.6\text{nm}^{-2}$, where N_b is the average number of side-chains per bottlebrush and R_g is the radius of gyration (estimated from small-angle neutron scattering measurements of a dilute solution of PS bottlebrushes in a good solvent) [144]. The shapes of these bottlebrush polymers can be predicted from their architectural parameters (summarized in Table 3.1) [121, 131, 135, 145–147]. The size of each norbornene repeat unit in the backbone is approximately 0.62 nm, so the length of a fully extended bottlebrush backbone is $L \approx (N_b \times 0.62)\text{nm}$ [121]. The size of each styrene repeat unit in the side-chain is 0.66 nm [148], so the diameter of a bottlebrush polymer is $D \approx (2\sigma^{0.25} N_{sc}^{0.75} \times 0.66)$ nm [145–147]. Therefore, the backbone DP's of 90 and 193 produce bottlebrushes with cylindrical aspect ratios (L:D) of approximately 2 and 4, respectively. The different backbone lengths from each batch are not a critical factor in our studies.

The objective of these studies is to characterize the thin film phase behavior of bottlebrush PS/linear dPS blends as a function of linear dPS chain length. Linear dPS was synthesized with chain lengths (N_m) that range from $N_m = 19$ to 2500 (Table

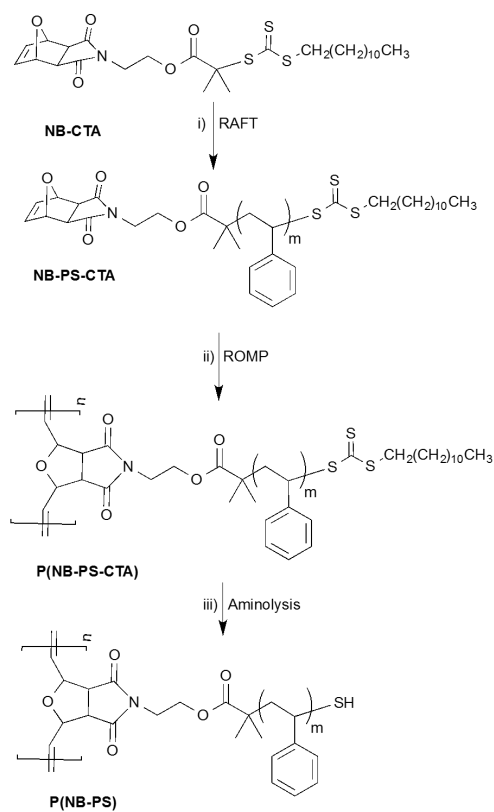


Figure 3.1: Synthetic scheme for the preparation of bottlebrush polymers with PS side-chains. i) AIBN, styrene, 60C, ii) CH_2Cl_2 , $((\text{H}_2\text{IMeS})(3\text{-Br-Py})_2(\text{Cl}_2)\text{RuCHPh})$ iii) THF, hexylamine, tributylphosphine.

3.2). (In the thesis in some of the figs we have represented N_m and N_b as N_M and N_B respectively). All blends contain 10 wt % (10 vol %) of bottlebrush PS. The blends are nearly athermal as the Flory interaction parameter for PS/dPS is approximately $\chi \cong 1.7 \times 10^{-4}$ [136]. The significance of a nearly athermal system is further discussed in the Appendix B. We note that blends of these dPS polymers (Table 3.2) with linear PS having an equivalent DP as the bottlebrushes ($N_b N_{sc}$, Table 3.1) are fully miscible at 165 °C. Therefore, any phase separation in blends of linear dPS and bottlebrush PS can be attributed to differences in architecture.

Thin films of the blends (150 or 200 nm) were cast on oxidized silicon wafers.

Table 3.2: Characteristics of Linear Deuterated Polystyrene

$M_n(kDa)$	N_m	\mathbf{D}_m
2.0	19	1.02
9.8	96	1.02
50.0	490	1.02
122.6	1201	1.02
254.9	2500	1.02

The film surfaces were imaged with optical microscopy and atomic force microscopy (see Appendix B, Figures B.3 – B.5), and there is no evidence of lateral phase separation in any samples (as-cast or annealed). The depth-dependent composition was measured with SIMS as a function of N_m and annealing time (at 165 C). The SIMS etch time is converted to etch depth by calibrating against a deuterated cover layer of known thickness [142]. The hydrogen signal during SIMS etching is unique to bottlebrush PS and is converted from counts to volume fraction (φ) based on the constraint that the amount of bottlebrush distributed throughout the film thickness is 10% of the total film volume. Representative SIMS data are included in Figure 3.2 for 150 nm blend films, and data for 200 nm blend films are reported in the Appendix B Figure B.6. Three clear trends emerge from visual inspection of these composition profiles. First, there is bottlebrush segregation at the top and or bottom of all films, but the interfacial excess is small in as-cast films and annealed films with $N_m < 100$. Second, the amount of bottlebrush polymer at each interface increases with annealing time when $N_m > 100$. Finally, while the bottlebrush does segregate at both interfaces when $N_m > 100$, there is a bias toward accumulation at the substrate over the free surface. These behaviors are illustrated by the schematic in Figure 3.3.

The SIMS data are fit using nonlinear regression to a depth-dependent composition profile $\varphi(z)$ that includes three additive contributions: (i) a bulk film structure represented by a Boxcar function, where $\varphi_{bulk}(z) = \varphi^\infty$ when $0 \leq z \leq h$ and 0

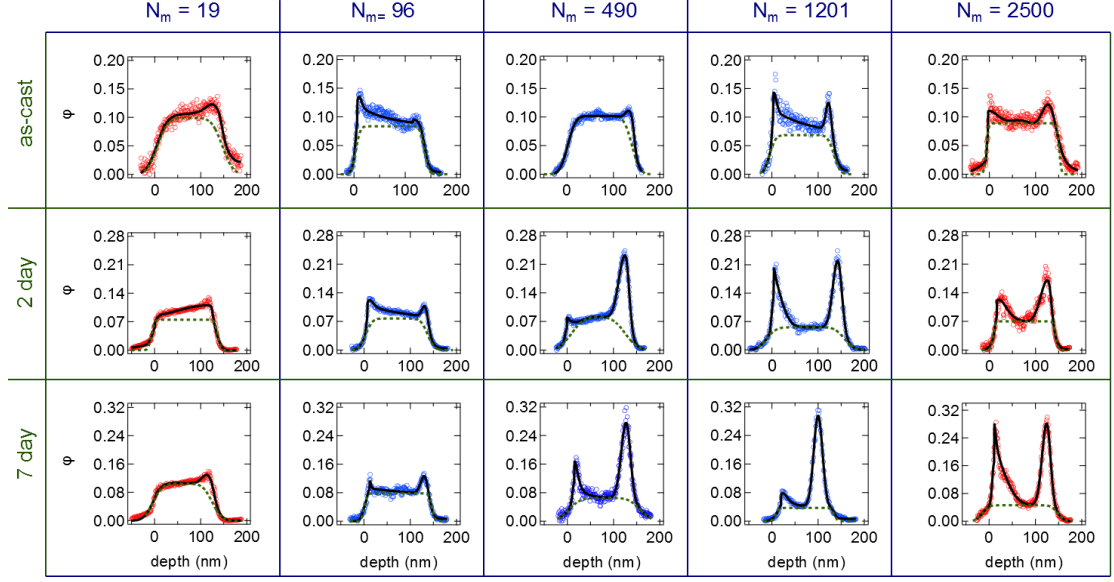


Figure 3.2: Concentration of bottlebrush polymer (φ) as a function of depth of film. Each column and row has different N_m , and different annealing times (165 C) respectively. (red: $N_b = 193$, and blue: $N_b = 90$).

otherwise; (ii) a surface excess which is modeled as an asymmetric Gaussian which is centered at $z = 0$ with skew toward the film interior; and (iii) a substrate excess centered at $z = h$ that is also modeled as an asymmetric Gaussian with skew toward the film interior. The composition profile $\varphi(z)$ is convolved with an instrumental Gaussian resolution function having a full width at half-maximum of 1218 nm (also a fitting parameter). Referring back to Figure 3.2, the dashed green line and the solid black line are the resolution-corrected profiles for φ^∞ and $\varphi(z)$, respectively.

The total interfacial excess z^* is defined as [142]

$$z^* = z_{surf}^* + z_{sub}^* = \int_0^{h/2} [\varphi(z) - \varphi^\infty] dz + \int_{h/2}^h [\varphi(z) - \varphi^\infty] dz, \quad (3.1)$$

where surface and substrate excesses are denoted as z_{surf}^* and z_{sub}^* , respectively, h is the total film thickness, and $z = 0$ denotes the top of the film. The interfacial excesses

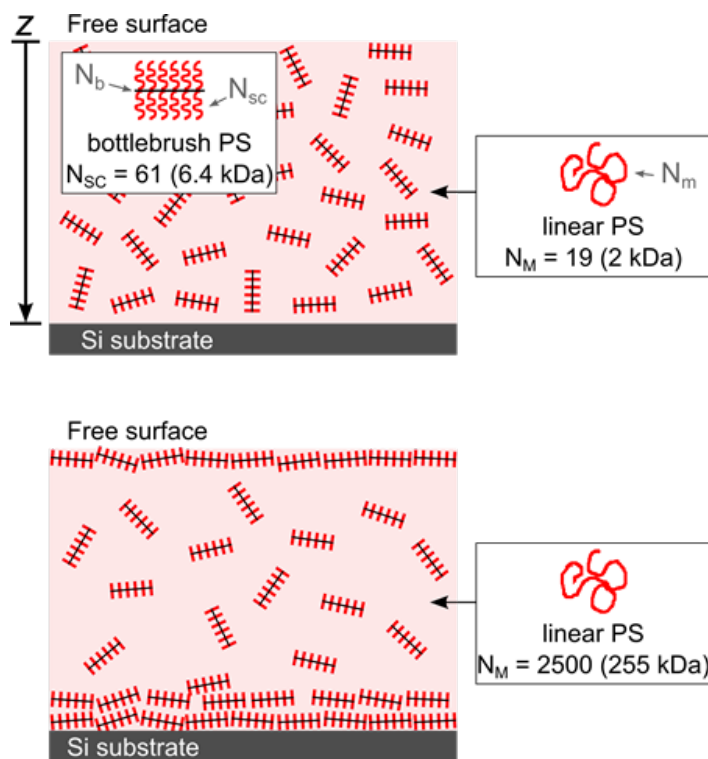


Figure 3.3: Cartoon illustrating the segregation profiles from SIMS after thermal annealing. As N_m increases, bottlebrush polymers segregate at both interfaces (with a bias toward accumulation at the substrate).

(z^*) and bulk concentration (φ^∞) are summarized as a function of N_m and annealing time for each data set in Figures 3.4 and 3.5, respectively. (The data sets differ in h and N_b , but the outcomes are independent of these parameters.) The as-cast films are characterized by a slight excess of bottlebrush at each interface, where z^* increases with N_m and is larger at the substrate than the free surface. After annealing at 165 C for 2 and 7 days, the surface excess is generally unchanged for all values of N_m . (There are two aberrations detected in the data set for $h = 150$ nm, at 2 days/ $N_m = 1201$ and 7 days/ $N_m = 490$.) The effects of annealing on substrate excess depend on N_m/N_{sc} , *i.e.*, the relative lengths of matrix chains to bottlebrush side chains. We identify two relevant regimes: When $N_m/N_{sc} \leq 1.6$, the substrate excess is only slightly enhanced

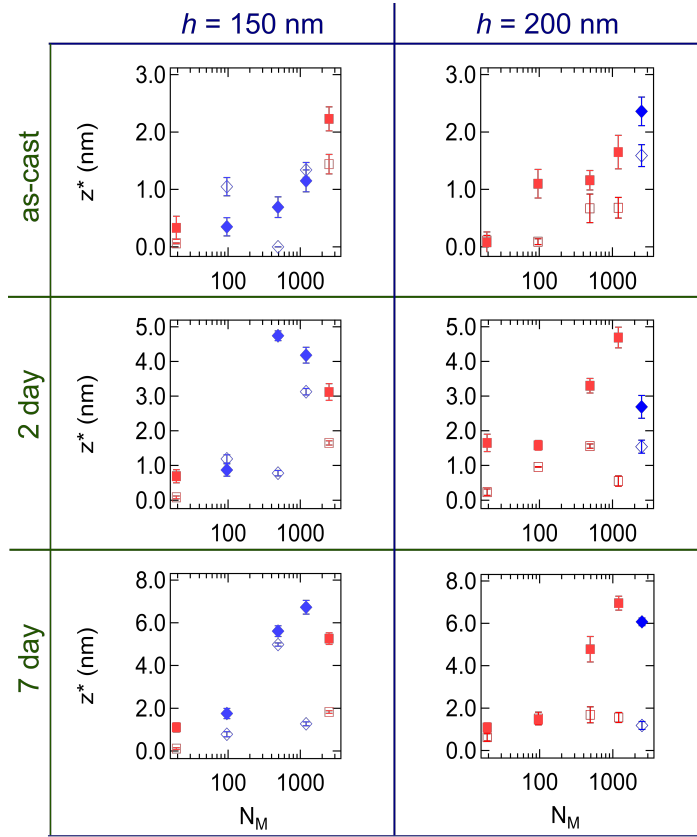


Figure 3.4: Interfacial excess z^* as a function of N_m and annealing time. Open and closed symbols correspond with surface and substrate excess, respectively. Red squares: $N_b = 193$ and blue diamonds: $N_b = 90$.

with annealing time. However, when $N_m/N_{sc} \geq 8$, thermal annealing increases the substrate excess by a factor of 35, and the ultimate concentration of bottlebrush near the substrate is approximately 30% (refer to the 7 day annealing data in Figure 3.2). A corresponding depletion of the bottlebrush polymers from the bulk of the film is observed in Figure 3.5. Data were not acquired for N_m/N_{sc} in the range of 1.68, so we cannot pinpoint the exact ratio that marks the boundary between dispersed and segregated phases.

The dependence of phase behavior on N_m/N_{sc} suggests that bottlebrush segregation is controlled by a balance of bulk miscibility and conformational entropy at the interfaces. The following paragraphs elaborate on these points. We observe a

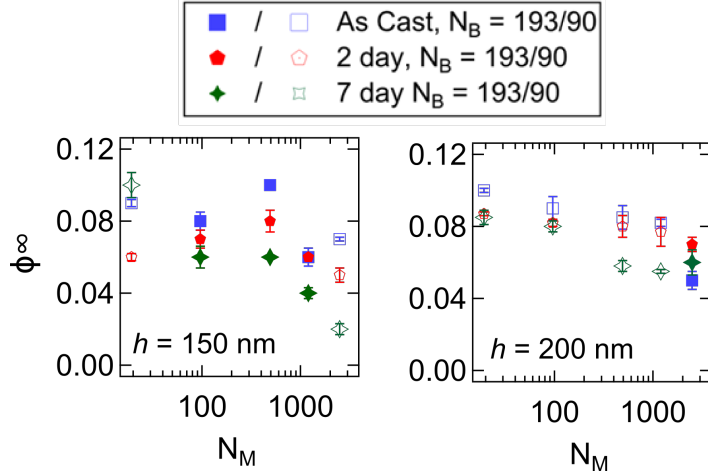


Figure 3.5: Bulk bottlebrush concentration φ^∞ as a function of N_m and annealing time. Closed symbols: $N_b = 193$ and open symbols: $N_b = 90$. $\varphi^\infty < 0.1$ indicates that bottlebrush is depleted from the middle of the film.

transition from dispersed to segregated bottlebrushes that is a function of swelling ratio N_m/N_{sc} and we interpret this behavior in the context of wetting and dewetting at the bottlebrush/melt interface. These wetting transitions have been examined for polymer melts in contact with planar brushes [89, 149] and polymer-grafted particles [150–152] using a variety of experimental methods and theoretical frameworks, and significant findings are discussed in recent Review [153] and Perspective [133, 134] articles. In general, fundamental studies aim to describe wetting behavior in terms of the polymer brush and melt architectures. Outcomes (e.g., scaling laws, phase diagrams) describe wettability as a function of polymer graft density σ , the ratio N_m/N_{sc} , and the curvature/aspect ratio of the brushed surface [149–151]. (Here we generalize N_{sc} to denote the length of grafted polymer chains at any type of surface.)

For example, the autophobic dewetting of homopolymers on a chemically identical planar brush was examined through self-consistent field theory (SCFT) [149], and predictions were later verified with detailed measurements of droplet contact angles and dry/wet brush thicknesses [89]. These works demonstrate that the interfacial tension γ between a melt and planar brush is always positive, but γ is very small when N_m/N_{sc} and/or grafting density are low, which permits metastable wetting at the brush/melt interface. On the other hand, when N_m/N_{sc} is large and/or grafting density is high, then the melt will dewet at the brush interface. The boundary between these regimes is difficult to define with a simple scaling law, as it depends on the criteria selected to define a wettable surface [149]. However, to offer a simple point of reference, the wetting/dewetting transition for a broad range of σ is observed with N_m/N_{sc} on the order of unity.

Similar trends are observed for polymer-grafted nanoparticles in bulk homopolymer matrices, where additional controlling variables include particle size and aspect ratio. These composites are characterized by dispersed and aggregated particle phases that correspond with wetting and dewetting at the graft/melt interface, respectively. In the limit of low particle curvature (large particles), the phase behavior predicted by SCFT and density functional theory (DFT) is similar to the planar brush/melt interface [150, 151]: The grafted shell is swollen at low N_m/N_{sc} and/or low σ , thereby dispersing the nanoparticles. As particle curvature is increased and/or aspect ratio is decreased (at constant σ), aggregation will occur at higher values of N_m/N_{sc} than planar dewetting [150, 151]. The parameter space controlling the transition from dispersed to aggregated nanoparticles has been mapped with experiments based on transmission electron microscopy [151, 152, 154, 155] (TEM) and ultrasmall-angle X-ray scattering [152, 156] (USAXS). While the exact phase boundaries depend on nanoparticle size, nanoparticle aspect ratio, and N_{sc} , these systems are generally

dispersed for low-to-intermediate values of N_m/N_{sc} in the range of 1–5 [151, 152, 157].

Thin film blends of polymer-grafted particles and linear polymers are not as widely studied as their bulk counterparts, but the few examples in the literature are consistent with the previously outlined concepts [154, 155]: Low N_m/N_{sc} ratios (<3) enable particle dispersion throughout the film thickness, and high N_m/N_{sc} ratios expel the particles from the matrix. In the latter regime, the particles are driven to both the free surface and the substrate interfaces, with a bias toward accumulation at the substrate. In an athermal system, there is no enthalpic preference for either constituent at the interfaces, so segregation is largely mediated by entropy: Specifically, the brushlike particles lose less conformational entropy at the surfaces compared with a linear polymer [153]. Similar behavior drives surface segregation of star polymers [158–160] and interfacial segregation of hard nanoparticles [161, 162] from a chemically identical linear melt.

The bottlebrush molecules employed for our studies are architecturally similar to polystyrene-grafted nanoparticles with cylindrical shapes, albeit without the inorganic core, and the bottlebrush side-chain lengths ($N_{sc} = 61$) are similar to the graft chain lengths employed by others [151, 155]. For polymer-coated nanoparticles, the grafting density σ is given by the number of polymeric chains per unit area of the nanoparticle surface. This definition is not applicable to bottlebrush polymers, where chains are tethered to a 1D polymer chain rather than a 2D surface, and the separation between side-chains along the bottlebrush backbone is given by the statistical segment length of the poly(oxanorbornene) backbone (0.62 nm) [121]. For comparison, we use the approximate number of side-chains per unit area of the bottlebrush polymer, $\sigma \approx 0.6nm^{-2}$. [144] This grafting density is comparable to that for polymer-coated nanoparticles which exhibit autophobic dewetting above a critical value of N_m/N_{sc} [151, 152].

We cannot test for dispersion and aggregation using TEM or grazing-incidence USAXS because the bottlebrush PS and matrix dPS have identical electron densities. Off-specular ultrasmall-angle neutron scattering is difficult to apply to thin films because the flux is very low, and to our knowledge, there are no dedicated beamlines in the US for this type of experiment. However, the SIMS data are indicative of a dispersed state when N_m/N_{sc} is low (≤ 1.6), and a segregated state when N_m/N_{sc} is high (≥ 8.0). These trends are highly consistent with the previously reviewed studies of polymer-grafted particles in chemically identical melts. As previously discussed, microscopy measurements do not detect any surface roughening that might indicate lateral aggregation and/or phase separation (see Appendix B Figures B.3 and B.4).

All films are characterized by an excess of PS bottlebrushes at the free surface and substrate interfaces, even at low values of N_m/N_{sc} . This behavior is not associated with enthalpic effects due to isotopic labeling, as the dPS matrix has a slightly lower surface energy than PS [137], and dPS is preferred over PS at an oxide surface [163]. To demonstrate this point, we carried out thin film blend studies using dPS bottlebrushes (Appendix B Figure B.7) mixed with high molecular weight linear PS. As shown in Appendix B Figure B.8, the dPS bottlebrushes also segregate to the film interfaces, and the surface excess is slightly enhanced compared with PS bottlebrushes. Another potential cause of interfacial excess at low N_m/N_{sc} is the end-groups on bottlebrush side-chains. The PS and dPS bottlebrush side-chains are terminated by thiol and CTA moieties, respectively. The similar segregation profiles in both systems suggest that end-group chemistry does not play a major role in the phase behavior, but this is difficult to quantitatively address without employing field theoretic models for data analysis [164]. We note that comparison of different terminal functionalities confirms that thiol-thiol bond formation does not drive the demixing

process, although such oxidative coupling is not anticipated with vacuum annealing [165]. Therefore, we attribute the interfacial excess of PS bottlebrush reported in Figure 3.4 to an architectural effect: The slight enthalpic preference for linear dPS at the free surface and substrate interfaces is more than offset by a conformational entropy gain at the film interior [158, 159].

In the limit of high N_m/N_{sc} (≥ 8.0), most of the bottlebrush expelled from the matrix is driven to the substrate rather than the free surface. A similar preference for the substrate interface has been reported for thin film blends of star [158] and polymer-coated nanoparticles [154] with linear polymers. Preferential segregation to the substrate may be due a stronger entropic driving force for segregation at the more restrictive hard surface. Alternatively, molecular simulation calculations indicate that even a weak attractive force can result in the adsorption of branched polymers or dendrimers onto a surface [166], and thus van der Waals interactions with the oxide surface may be driving preferential segregation to the substrate interface [153].

3.4 Conclusions

Through secondary ion mass spectroscopy, we examined the phase behavior of bottlebrush polystyrene and linear deuterated polystyrene in thin films. The bottlebrush polystyrenes employed for these studies have short backbones and resemble hairy cylindrical nanoparticles. These systems exhibit wetting and dewetting transitions that drive bottlebrush dispersion or aggregation, respectively, which are controlled by the relative lengths of matrix chains N_m to bottlebrush side-chains N_{sc} . At low values of N_m/N_{sc} (≤ 1.6), the bottlebrushes are dispersed throughout the film thickness with a slight excess at the free surface and substrate interfaces. At high values of N_m/N_{sc} (≥ 8.0), the bottlebrushes are depleted from the interior of the film and

strongly segregated at the interfaces. The interfacial excess is driven by an entropic depletion attraction effect: larger branched molecules are adsorbed (attracted) to the interfaces, and the linear chains are displaced to the films interior where they gain conformational entropy. A preferential segregation to the substrate interface over the air interface is observed, and this may be driven by the more restrictive condition of a hard surface or weak van der Waals interactions between the bottlebrush polymers and the oxide surface.

This work demonstrates the spontaneous segregation of bottlebrush additives to film interfaces due to entropic effects and suggests that bottlebrushes can potentially serve as useful additives for modifying the surface and interfacial properties of thin film coatings. Future work will explore a broader parameter space (N_{sc} , N_b) in thin film blends and bulk materials. In bulk systems, we expect that entropic effects can drive bottlebrush aggregation, and this behavior can be detected with ultrasmall-angle neutron scattering. Furthermore, we will extend this work to nonathermal blends, as functional bottlebrushes (composed of different types of side-chains) are relevant for applications in fouling reduction and adhesives.

4 Conclusion and Outlook

Complex morphologies arising from BCPs will have a tremendous impact in emerging technological areas [167–169]. The patterns from the microphase separation of the polymer blocks into nanodomains have the potential to serve as the building blocks for pattern transfer [170,171]. However, the need for the BCP pattern to have precise and reproducible regularity both across the substrate and through the depth of the film is an understatement. Thus the existing challenges in BCP thin films are of tremendous relevance in terms of understanding block-block interactions and the evolved structures [172,173].

In spite of their merits in parallel processing, resolution, and ability to generate templates for nanopatterning, the practical application of block copolymer thin films till now has been few [174]. Out-of-plane defects have not gained much attention, however, they have to be minimized in order to be able to use these systems as pattern transfer mask without significant errors in feature size and placement [175,176]. The lack of a robust strategy to modulate structure formation in thin film geometries has been considered a major obstacle.

We in this work have been able to shed light on the very important aspect of surface and substrate interactions for the lamellar diblock copolymer and its role in modification of morphology and structure. Domain orientations in diblock copolymer films are sensitive to annealing temperature, quality of neutral substrate and film thickness. Lateral in-plane order is better at the middle of the films than at interfaces. Our investigations on BCP thin films on surfaces modified by the random copolymer brushes show that it is difficult to modulate their substrate energetics. However the results unequivocally elucidate the importance of substrate interactions which can

induce and/or trap both out-of-plane and in-plane defects. We see that the influence of the substrate decays with distance into the film [177–179]. The outcomes from our study has helped us to understand the key variables, apart from thickness, annealing temperature and time, which control substrate interactions. For the random copolymers we have identified, grafting density as the most relevant variable which influence and screens interactions of the polymer with the substrate. However the parameter space can be broad which may enforce more stringent criterion on determining morphology and structure as has been reported in some recent simulations [85]. The studies reported the self-assembly of diblock copolymer on substrates modified by random copolymer brushes, where apart from grafting density, the blockiness of the random copolymer and ratio of the free chains to that of grafted chains do also play an important role.

We also briefly mention here some of the pertinent issues we had working with silanes as substrate modifiers. The BCP deposition procedure is identical to the random copolymer case. The material component we used for neutralization was octyldimethylchlorosilane(ODS), (Chemical Formula: $\text{CH}_3(\text{CH}_2)_7\text{Si}(\text{CH}_3)_2\text{Cl}$). Functionalization of ODS on the silicon substrate proceeded via the condensation reaction. The quality of surface neutrality in this case was mainly determined through the surface energies of the silane surface which was determined by the water contact angles. However from a perspective of experimental procedure we controlled the oxidation time (measured via UV-ozone exposure time) of the silane treated surface to generate the contact angles which gave us the desired lamellar fingerprint patterns. So we have chosen to represent the mean oxidation time as our process variable. In Figure 4.1 we show the investigations of morphology of the BCP films spin casted on silane substrate oxidized for $\tau_{ox} \sim 15$ secs which shows presence of mixed orientations. It may be a signature of the fact that the oxidation is not enough to screen preferential

interactions. We see from the Figure 4.2 that for films oxidized for $\tau_{ox} \geq 25$ secs the

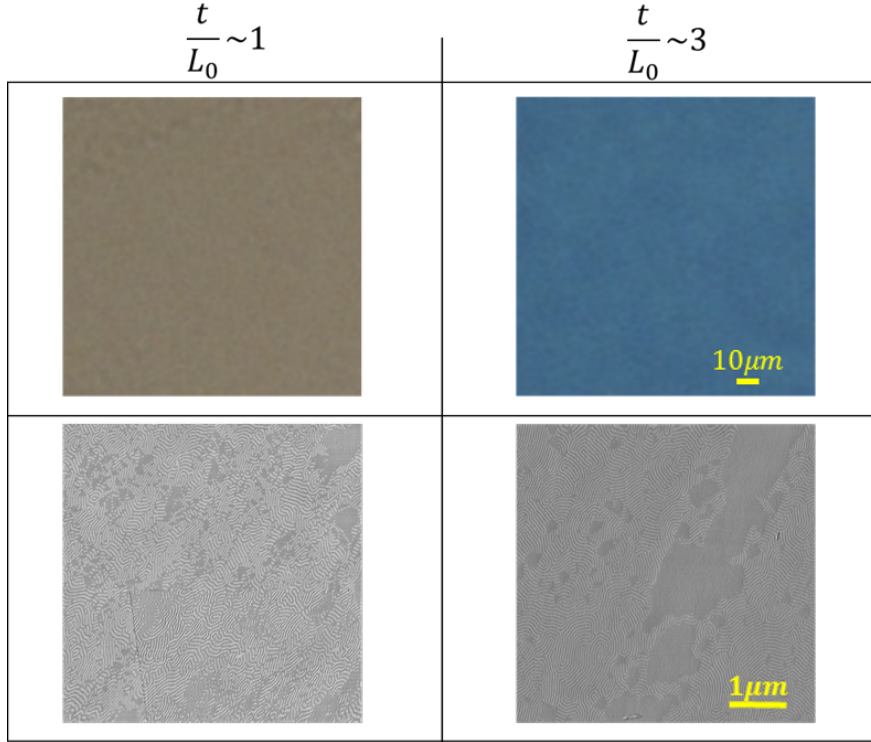


Figure 4.1: Patchy microscopy images for two BCP film thickness on silane substrate exposed for $\tau_{ox} = 15$ secs. Upper panel is the optical image and lower one is the AFM image.

films did not exhibit any structure. The structure is optimal for comparatively lower oxidation times with less misoriented domains and perpendicular structure as evident from GISAXS and SEM images respectively. However the structure also depends on film thickness (not shown here). We have also noticed that the lowest oxidation time gives rise to a high extent of patchy structures. Our observations indicate higher density of out-of-plane defects and narrow windows of perpendicularity for the coatings of oxidized ODS. Due to our inability to precisely tune surface energetics by oxidation of silanes, we like to propose that they may not be an optimal approach for substrate modification.

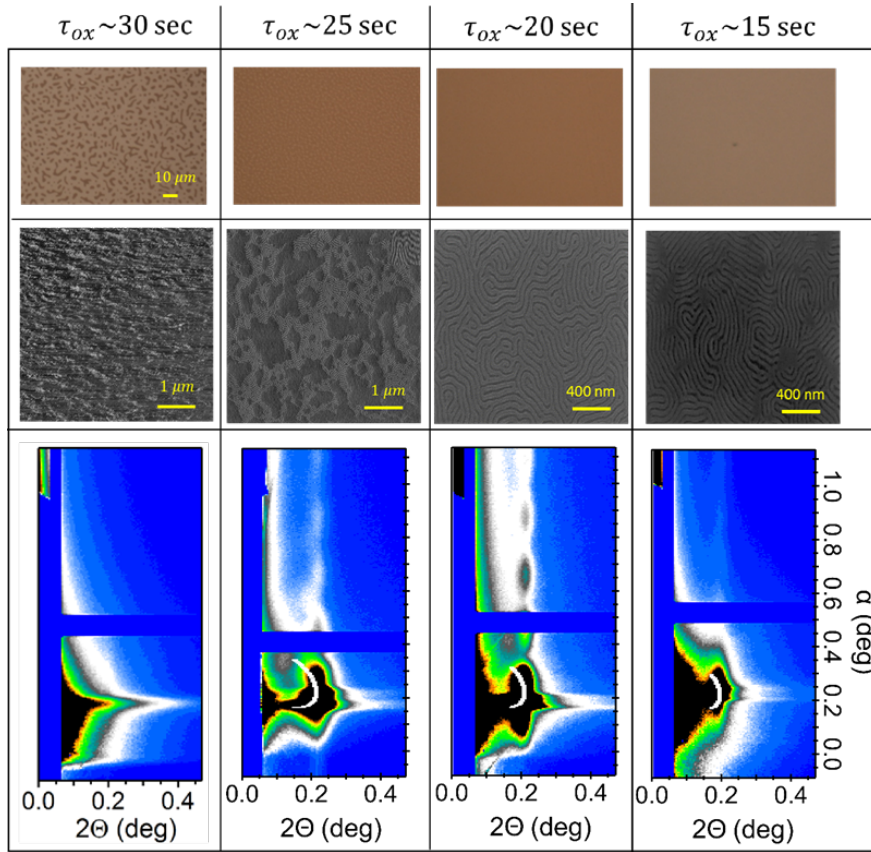


Figure 4.2: Optical, SEM and GISAXS characterization of thin films on SAM oxidized for different times as shown above. (All film thickness are $t/L_0 \sim 1$ except for $\tau_{ox} = 20$ secs, film thickness is around $0.5L_0$).

In order to check if the effects of interactions are specific to a particular morphology, we also have investigated the role of cylindrical diblock copolymer system (PS–PMMA). The molecular weight of the block copolymer has been quite similar to the lamellar diblock copolymer we have considered in our study. In Figure 4.3 we have shown the scattering data for a cylindrical diblock copolymer deposited on a surface modified by the random copolymer with 55% styrene. In Figure 4.3 the data is shown for two different sets of annealing temperature and times. From the GISAXS images some facts emerge by inspection. For example for the samples annealed at $T = 190$ °C for 10 min, the presence of tilted domains is indicated by the smeared

out-of-plane form factor oscillations. However, as temperature is increased the form factors indicate a flow towards order.

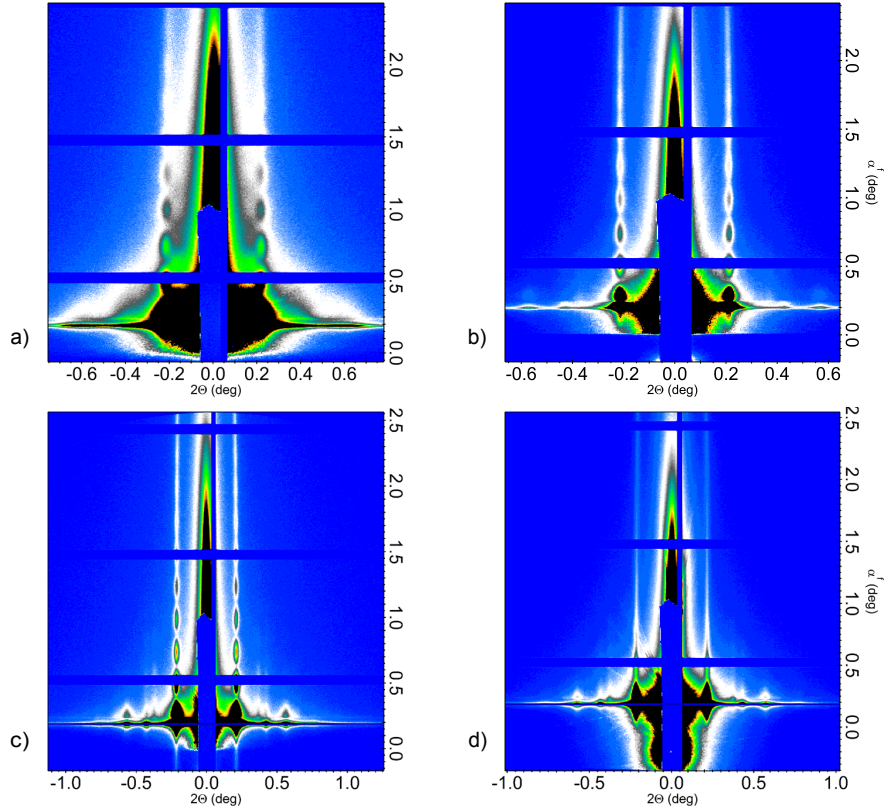


Figure 4.3: GISAXS data for cylindrical diblocks for $t/L_0 = 1.09$ a) T: 190 °C; time: 10 min, b) T: 240 °C; time: 10 min, c) T: 190 °C; time: 24 hours and d) T: 240 °C; time: 24 hours.

To quantify our conclusions further we have shown in Figure 4.4 the line cuts from the images in Figure 4.3. The analysis of peak positions from line cuts show systematic absence of some peak positions. Nevertheless the peak positions do indicate the presence of hexagonal cylindrical symmetry as expected from a cylindrical BCP [180]. We also notice that films annealed at T = 190 °C for 10 min has relatively poor order compared to the film annealed at T = 240 °C for 10 min. However, after 24 hrs of annealing time we see that for films annealed at both the temperatures the

order has substantially improved in both the films and comparable to each other as the presence of peaks from the respective line cuts demonstrate. We also measured the full width half maximum (FWHM) for the peaks in all the cases which quantifies the quality of lateral order (lateral order $\propto 1/FWHM$). The analysis of FWHM shows that in general the films annealed at 240 °C have better lateral order than the films annealed at 190 °C. However, for the films annealed at 240 °C we do not see any significant changes in lateral order even after increasing the annealing time to 24 hrs, but for the films annealed at 190 °C, there is slight improvement of lateral order after longer time. Thus our preliminary scattering studies on cylindrical morphology shows some very interesting issues related to the nature of polymer thin films which can actively be pursued in a later work.

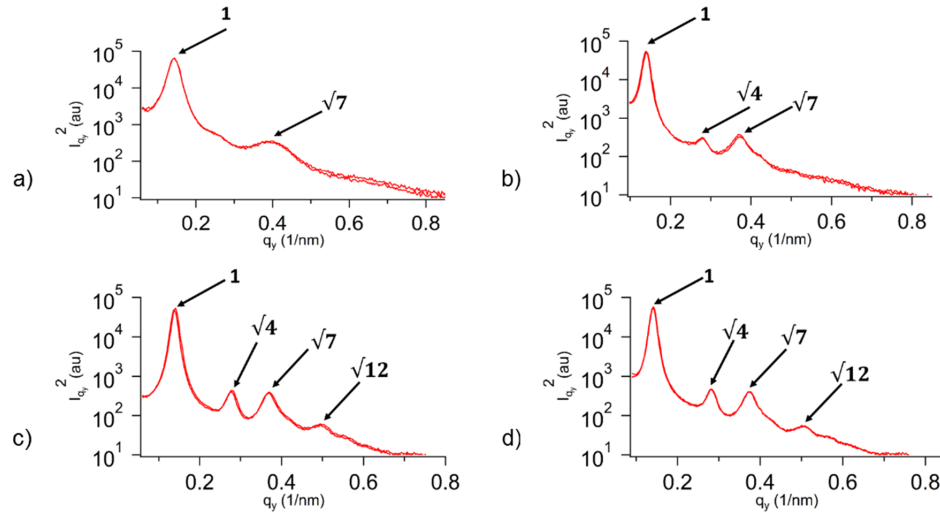


Figure 4.4: GISAXS line cuts for cylindrical diblocks for $t/L_0 = 1.09$ a) T: 190 °C; time: 10 min, b) T: 240 °C; time: 10 min, c) T: 190 °C; time: 24 hours and d) T: 240 °C; time: 24 hours. Arrows mark the relative peak positions.

4.1 Future Directions

A natural extension of this work can focus on systematically tuning the substrate interface by varying the parameter window, and measure the defect structure with GISAXS. Our results on the defect analysis as a result of the interactions between copolymer and the modified substrate can be readily extended to design and optimize the directed self-assembly of block copolymers on chemo-epitaxial templates [181–183]. Once we obtain the optimal design of the underlying coating, these materials can be tested in a directed self assembly process using a lamellar copolymer.

Operationally the random copolymer is grafted to a substrate, then coated with resist. The resist is patterned with conventional top-down lithographic methods, developed, and used as an oxidation mask. After removing the resist, the oxidized stripes are attractive to PMMA of the block copolymer. These oxidized stripes should serve to pin PMMA domains and force lateral order in the system. X-ray scattering can be used to measure defect densities and domain shapes as a function of quality of the neutral surfaces, the frequency of the pinning stripes and also the match between the lamellar periodicity L_0 and the width of the preferential stripes w [184–186]. We expect the density of defects will increase as the frequency of the stripes is reduced as we have shown in the cartoon in Figure 4.5.

For epitaxial templates, usually template commensurability (quantified by w/L_0) and types of interaction between the BCP domains and underlying epitaxial template governs domain shapes. Studies have originated in our group [86] using scattering profiles of the BCP thin films on epitaxial templates to detect the presence of sloped sidewalls and our present work can be further extended to probe these defects in greater detail.

While chemo-epitaxial templates can induce long-range lateral order, there is

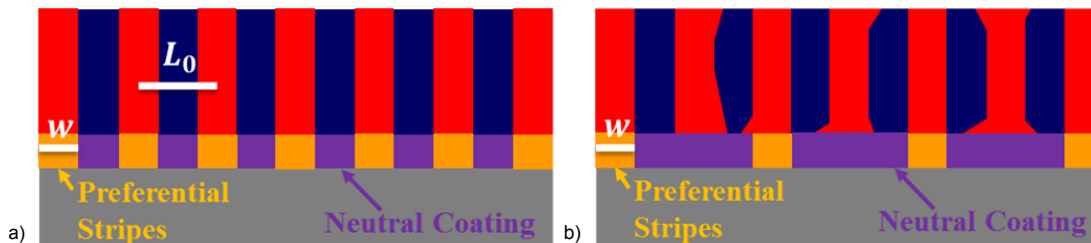


Figure 4.5: Effect of the frequency of chemical pattern on lamellar diblock copolymer ordering. a) Well ordered perpendicular lamellar and b) presence of tilted domains.

substantial evidence that thermal fluctuations induce variability in domain size and roughness [183]. Thus from a semiconductor manufacturing perspective, apart from defects, another important metric is line-edge roughness (LER) [187]. LER refers to fluctuations in the position of the line edge. Such fluctuations lead to variability in feature size, and this has a negative impact on the performance of transistors, where consistency across a chip is critical [183, 188]. We believe our results on substrate interactions of lamellar diblock copolymers can serve as an useful guide to understand the effects of the pinning stripes on LER.

The present work is mainly based on PS–PMMA lamellar diblock copolymer thin films. Even though PS–PMMA is an excellent system to illustrate the underlying mechanisms of block copolymer lithography, the χ –parameter for this diblock is pretty small. Thus PS–PMMA system will be unable to produce feature sizes below 10 nm length scales. From a directed self assembly perspective, there is a large collection of work [82, 189, 190] which focusses on the synthesis of new block copolymer systems with high enough χ . Poly(styrene–*b*–dimethylsiloxane) (PS–PDMS) is an example of such a system which can assemble into smaller domains. (≤ 10 nm) However due to a large mismatch in surface tensions of each block in this case, even with neutral substrate surface coatings, the top interface remains preferential irrespective

of thermal annealing treatments. This is a challenging problem and is a crucial for the eventual success of directed self assembly process. To address this problem, a variety of “topcoat” materials have been developed to control interactions at the top of the film [191,192]. However these approaches are difficult to extend to arbitrary block copolymer chemistries. In these regard our studies on the phase behavior of linear/bottlebrush polymer blends in Chapter 4 [193] can substantially help us to design bottlebrush additives which can spontaneously segregate into “neutral” topcoats for block copolymer lithography. To prove a point in this case, surface-active PS/PDMS bottlebrush polymer additives will form spontaneous topcoats for lamellar PS–PDMS block copolymer films which will promote perpendicular domain orientation, the most critical feature for nanopatterning.

References

- [1] I. W. Hamley, "Structure and flow behaviour of block copolymers," *Journal of Physics: Condensed Matter*, vol. 13, no. 33, p. R643, 2001.
- [2] F. Bates and G. Fredrickson, "Block Copolymer Thermodynamics - Theory And Experiment," *Annual Review Of Physical Chemistry*, vol. 41, pp. 525–557, 1990.
- [3] N. Bowden, S. Brittain, A. G. Evans, J. W. Hutchinson, and G. M. Whitesides, "Spontaneous formation of ordered structures in thin films of metals supported on an elastomeric polymer," *Nature*, vol. 393, no. 6681, pp. 146–149, 1998.
- [4] C. J. Buchko, L. C. Chen, Y. Shen, and D. C. Martin, "Processing and microstructural characterization of porous biocompatible protein polymer thin films," *Polymer*, vol. 40, no. 26, pp. 7397–7407, 1999.
- [5] M. Ibn-Elhaj and M. Schadt, "Optical polymer thin films with isotropic and anisotropic nano-corrugated surface topologies," *Nature*, vol. 410, no. 6830, pp. 796–799, 2001.
- [6] S. Y. Yang and M. F. Rubner, "Micropatterning of polymer thin films with pH-sensitive and cross-linkable hydrogen-bonded polyelectrolyte multilayers," *Journal of the American Chemical Society*, vol. 124, no. 10, pp. 2100–2101, 2002.
- [7] J. Ouyang, C.-W. Chu, C. R. Szmanda, L. Ma, and Y. Yang, "Programmable polymer thin film and non-volatile memory device," *Nature materials*, vol. 3, no. 12, pp. 918–922, 2004.

- [8] M. Lundstrom, “A top-down look at bottom-up electronics,” 2003.
- [9] D. Xia, D. Li, Z. Ku, Y. Luo, and S. R. J. Brueck, “Top-down approaches to the formation of silica nanoparticle patterns,” *Langmuir*, vol. 23, no. 10, pp. 5377–5385, 2007.
- [10] J. Bang, U. Jeong, D. Ryu, T. Russell, and C. Hawker, “Block Copolymer Nanolithography: Translation of Molecular Level Control to Nanoscale Patterns,” *Advanced Materials*, vol. 21, no. 47, pp. 4769–4792, 2009.
- [11] L. W. Liebmann, “Resolution enhancement techniques in optical lithography: It’s not just a mask problem,” in *Photomask and Next Generation Lithography Mask Technology VIII*, pp. 23–32, International Society for Optics and Photonics, 2001.
- [12] D. Bratton, D. Yang, J. Dai, and C. K. Ober, “Recent progress in high resolution lithography,” *Polymers for advanced technologies*, vol. 17, no. 2, pp. 94–103, 2006.
- [13] M. Shimomura and T. Sawadaishi, “Bottom-up strategy of materials fabrication: a new trend in nanotechnology of soft materials,” *Current opinion in colloid & interface science*, vol. 6, no. 1, pp. 11–16, 2001.
- [14] X. Zhang, C. Sun, and N. Fang, “Manufacturing at nanoscale: Top-down, bottom-up and system engineering,” *Journal of Nanoparticle Research*, vol. 6, no. 1, pp. 125–130, 2004.
- [15] W. Lu and C. M. Lieber, “Nanoelectronics from the bottom up,” *Nature materials*, vol. 6, no. 11, pp. 841–850, 2007.

- [16] T. P. Lodge, "Block copolymers: past successes and future challenges," *Macromolecular Chemistry and Physics*, vol. 204, no. 2, pp. 265–273, 2003.
- [17] J. Bang, U. Jeong, D. Y. Ryu, T. P. Russell, and C. J. Hawker, "Block copolymer nanolithography: translation of molecular level control to nanoscale patterns.," *Advanced materials (Deerfield Beach, Fla.)*, vol. 21, pp. 4769–92, Dec. 2009.
- [18] A. V. Ruzette and L. Leibler, "Block copolymers in tomorrow's plastics," *Nature materials*, vol. 4, no. 1, pp. 19–31, 2005.
- [19] J. Cheng, C. Ross, E. Thomas, H. Smith, and G. Vancso, "Fabrication of nanostructures with long-range order using block copolymer lithography," *Applied Physics Letters*, vol. 81, pp. 3657–3659, NOV 4 2002.
- [20] R. Ruiz, H. Kang, F. A. Detcheverry, E. Dobisz, D. S. Kercher, T. R. Albrecht, J. J. de Pablo, and P. F. Nealey, "Density multiplication and improved lithography by directed block copolymer assembly," *Science*, vol. 321, no. 5891, pp. 936–939, 2008.
- [21] M. Stoykovich, M. Muller, S. Kim, H. Solak, E. Edwards, J. de Pablo, and P. Nealey, "Directed assembly of block copolymer blends into nonregular device-oriented structures," *Science*, vol. 308, pp. 1442–1446, JUN 3 2005.
- [22] M. Fasolka and A. Mayes, "Block copolymer thin films: Physics and applications," *Annual Review of Materials Research*, vol. 31, pp. 323–355, 2001.
- [23] R. Segalman, "Patterning with block copolymer thin films," *Materials Science & Engineering R-Reports*, vol. 48, no. 6, pp. 191–226, 2005.

- [34] M. P. Stoykovich and P. F. Nealey, “Block copolymers and conventional lithography,” *Materials Today*, vol. 9, no. 9, pp. 20–29, 2006.
- [35] J. Y. Cheng, D. P. Sanders, H. D. Truong, S. Harrer, A. Friz, S. Holmes, M. Colburn, and W. D. Hinsberg, “Simple and versatile methods to integrate directed self-assembly with optical lithography using a polarity-switched photoresist,” vol. 4, no. 8, pp. 4815–4823, 2010.
- [36] B. Liu, S. Narayanan, D. T. Wu, and M. D. Foster, “Polymer Film Surface Fluctuation Dynamics in the Limit of Very Dense Branching,” *Macromolecules*, vol. 46, no. 8, pp. 3190–3197, 2013.
- [37] I. W. Hamley and others, *The physics of block copolymers*, vol. 19. Oxford University Press New York, 1998.
- [38] M. Matsen, “Thin films of block copolymer,” *Journal of Chemical Physics*, vol. 106, no. 18, pp. 7781–7791, 1997.
- [39] C. Harrison, M. Park, P. Chaikin, R. A. Register, D. H. Adamson, and N. Yao, “Depth profiling block copolymer microdomains,” *Macromolecules*, vol. 31, no. 7, pp. 2185–2189, 1998.
- [40] E. Huang, L. Rockford, T. P. Russell, and C. J. Hawker, “Nanodomain control in copolymer thin films,” *Nature*, vol. 395, no. 6704, pp. 757–758, 1998.
- [41] E. Huang, S. Pruzinsky, T. P. Russell, J. Mays, and C. J. Hawker, “Neutrality Conditions for Block Copolymer Systems on Random Copolymer Brush Surfaces,” *Macromolecules*, vol. 32, no. 16, pp. 5299–5303, 1999.

- [42] G. Coulon, T. Russell, V. Deline, and P. Green, "Surface-induced orientation of symmetric, diblock copolymers - a secondary ion mass-spectrometry study," *Macromolecules*, vol. 22, no. 6, pp. 2581–2589, 1989.
- [43] P. F. Green and T. P. Russell, "Adsorption of copolymer chains from a melt onto a flat surface," *Macromolecules*, vol. 25, no. 2, pp. 783–787, 1992.
- [44] S. Ham, C. Shin, E. Kim, D. Ryu, U. Jeong, T. Russell, and C. Hawker, "Microdomain orientation of PS-b-PMMA by controlled interfacial interactions," *Macromolecules*, vol. 41, no. 17, pp. 6431–6437, 2008.
- [45] E. Han, K. Stuen, M. Leolukman, C.-C. Liu, P. Nealey, and P. Gopalan, "Perpendicular orientation of domains in cylinder-forming block copolymer thick films by controlled interfacial interactions," *Macromolecules*, vol. 42, no. 13, pp. 4896–4901, 2009.
- [46] K. Yager, B. Berry, K. Page, D. Patton, A. Karim, and E. Amis, "Disordered nanoparticle interfaces for directed self-assembly," *Soft Matter*, vol. 5, no. 3, pp. 622–628, 2009.
- [47] H. Suh, H. Kang, C.-C. Liu, P. Nealey, and K. Char, "Orientation of block copolymer resists on interlayer dielectrics with tunable surface energy," *Macromolecules*, vol. 43, no. 1, pp. 461–466, 2010.
- [48] C. Bates, J. Strahan, L. Santos, B. Mueller, B. Bamgbade, J. Lee, J. Katzenstein, C. Ellison, and C. Willson, "Polymeric Cross-Linked Surface Treatments for Controlling Block Copolymer Orientation in Thin Films," *Langmuir*, vol. 27, no. 5, pp. 2000–2006, 2011.

- [49] T. Vu, N. Mahadevapuram, G. M. Perera, and G. E. Stein, “Controlling Domain Orientations in Thin Films of AB and ABA Block Copolymers,” *Macromolecules*, vol. 44, no. 15, pp. 6121–6127, 2011.
- [50] M. J. Maher, C. M. Bates, G. Blachut, S. Sirard, J. L. Self, M. C. Carlson, L. M. Dean, J. D. Cushen, W. J. Durand, C. O. Hayes, and others, “Interfacial Design for Block Copolymer Thin Films,” *Chemistry of Materials*, vol. 26, no. 3, pp. 1471–1479, 2014.
- [51] R. D. Peters, P. Stasiak, M. W. Matsen, and K. Dalnoki-Veress, “Morphology induced spinodal decomposition at the surface of symmetric diblock copolymer films,” *ACS Macro Letters*, vol. 2, no. 5, pp. 441–445, 2013.
- [52] S. Ji, U. Nagpal, G. Liu, S. P. Delcambre, M. MuñLLler, J. J. de Pablo, and P. F. Nealey, “Directed assembly of non-equilibrium ABA triblock copolymer morphologies on nanopatterned substrates,” *ACS nano*, vol. 6, no. 6, pp. 5440–5448, 2012.
- [53] P. Mansky, T. Russell, C. Hawker, J. Mays, D. Cook, and S. Satija, “Interfacial segregation in disordered block copolymers: Effect of tunable surface potentials,” *Physical Review Letters*, vol. 79, no. 2, pp. 237–240, 1997.
- [54] D. A. Winesett, H. Ade, J. Sokolov, M. Rafailovich, and S. Zhu, “Substrate dependence of morphology in thin film polymer blends of polystyrene and poly (methyl methacrylate),” *Polymer International*, vol. 49, no. 5, pp. 458–462, 2000.
- [55] D. A. Winesett, S. Story, J. Luning, and H. Ade, “Tuning substrate surface energies for blends of polystyrene and poly (methyl methacrylate),” vol. 19, no. 20, pp. 8526–8535, 2003.

- [56] C. D. Knorowski, J. A. Anderson, and A. Travesset, "Self-assembled ordered polymer nanocomposites directed by attractive particles.," *The Journal of chemical physics*, vol. 128, p. 164903, Apr. 2008.
- [57] J. Y. Cheng, C. A. Ross, E. L. Thomas, H. I. Smith, and G. J. Vancso, "Templated self-assembly of block copolymers: Effect of substrate topography," *Advanced Materials*, vol. 15, no. 19, pp. 1599–1602, 2003.
- [58] X. Li, S. L. Prukop, S. L. Biswal, and R. Verduzco, "Surface Properties of Bottlebrush Polymer Thin Films," *Macromolecules*, vol. 45, no. 17, pp. 7118–7127, 2012.
- [59] J. Rzayev, "Molecular bottlebrushes: new opportunities in nanomaterials fabrication," *ACS Macro Letters*, vol. 1, no. 9, pp. 1146–1149, 2012.
- [60] R. A. Farrell, T. G. Fitzgerald, D. Borah, J. D. Holmes, and M. A. Morris, "Chemical interactions and their role in the microphase separation of block copolymer thin films," *International journal of molecular sciences*, vol. 10, no. 9, pp. 3671–3712, 2009.
- [61] P. Mansky, Y. Liu, E. Huang, T. Russell, and C. Hawker, "Controlling polymer-surface interactions with random copolymer brushes," *Science*, vol. 275, no. 5305, pp. 1458–1460, 1997.
- [62] E. Han, K. Stuen, Y.-H. La, P. Nealey, and P. Gopalan, "Effect of composition of substrate-modifying random copolymers on the orientation of symmetric and asymmetric diblock copolymer domains," *Macromolecules*, vol. 41, no. 23, pp. 9090–9097, 2008.

- [63] P. Liu, P. Thebault, P. Guenoun, and J. Daillant, “Easy orientation of diblock copolymers on self-assembled monolayers using uv irradiation,” *Macromolecules*, vol. 42, no. 24, pp. 9609–9612, 2009.
- [64] J. N. L. Albert, M. J. Baney, C. M. Stafford, J. Y. Kelly, and T. H. Epps III, “Generation of monolayer gradients in surface energy and surface chemistry for block copolymer thin film studies,” *ACS nano*, vol. 3, no. 12, pp. 3977–3986, 2009.
- [65] W. J. Durand, G. Blachut, M. J. Maher, S. Sirard, S. Tein, M. C. Carlson, Y. Asano, S. X. Zhou, A. P. Lane, C. M. Bates, and others, “Design of high- Γ block copolymers for lithography,” *Journal of Polymer Science Part A: Polymer Chemistry*, vol. 53, no. 2, pp. 344–352, 2015.
- [66] M. J. Maher, C. T. Rettner, C. Bates, G. Blachut, M. C. Carlson, W. J. Durand, C. J. Ellison, D. P. Sanders, J. Y. Cheng, and C. G. Willson, “Directed Self-Assembly of Silicon-Containing Block Copolymer Thin Films,” *ACS applied materials & interfaces*, 2015.
- [67] G. E. Stein, N. Mahadevapuram, and I. Mitra, “Controlling interfacial interactions for directed self assembly of block copolymers,” *Journal of Polymer Science Part B: Polymer Physics*, vol. 53, no. 2, pp. 96–102, 2015.
- [68] C. M. Bates, M. J. Maher, D. W. Janes, C. J. Ellison, and C. G. Willson, “Block copolymer lithography,” *Macromolecules*, vol. 47, no. 1, pp. 2–12, 2014.
- [69] H. Yi, X.-Y. Bao, J. Zhang, C. Bencher, L.-W. Chang, X. Chen, R. Tiberio, J. Conway, H. Dai, Y. Chen, S. Mitra, and H.-S. P. Wong, “Flexible Control of Block Copolymer Directed Self-Assembly using Small, Topographical

- Templates: Potential Lithography Solution for Integrated Circuit Contact Hole Patterning,” *Advanced Materials*, vol. 24, pp. 3107–3114, JUN 19 2012.
- [70] C. C. Liu, A. Ramirez-Hernandez, E. Han, G. S. W. Craig, Y. Tada, H. Yoshida, H. Kang, S. Ji, P. Gopalan, J. J. de Pablo, and P. F. Nealey, “Chemical patterns for directed self-assembly of lamellae-forming block copolymers with density multiplication of features,” *Macromolecules*, vol. 46, no. 4, pp. 1415–1424, 2013.
- [71] D. Ryu, K. Shin, E. Drockenmuller, C. Hawker, and T. Russell, “A generalized approach to the modification of solid surfaces,” *Science*, vol. 308, no. 5719, pp. 236–239, 2005.
- [72] C. Harrison, D. H. Adamson, Z. Cheng, J. M. Sebastian, S. Sethuraman, D. A. Huse, R. A. Register, and P. M. Chaikin, “Mechanisms of ordering in striped patterns,” *Science*, vol. 290, no. 5496, pp. 1558–1560, 2000.
- [73] C. Harrison, Z. Cheng, S. Sethuraman, D. A. Huse, P. M. Chaikin, D. A. Vega, J. M. Sebastian, R. A. Register, and D. H. Adamson, “Dynamics of pattern coarsening in a two-dimensional smectic system,” *Physical Review E*, vol. 66, no. 1, p. 011706, 2002.
- [74] M. Hammond, E. Cochran, G. Fredrickson, and E. Kramer, “Temperature dependence of order, disorder, and defects in laterally confined diblock copolymer cylinder monolayers,” *Macromolecules*, vol. 38, pp. 6575–6585, 2005.
- [75] H. Takahashi, N. Laachi, K. T. Delaney, S.-M. Hur, C. J. Weinheimer, D. Shykind, and G. H. Fredrickson, “Defectivity in Laterally Confined Lamella-Forming Diblock Copolymers: Thermodynamic and Kinetic Aspects,” *Macromolecules*, vol. 45, no. 15, pp. 6253–6265, 2012.

- [76] V. Mishra, G. H. Fredrickson, and E. J. Kramer, "Effect of film thickness and domain spacing on defect densities in directed self-assembly of cylindrical morphology block copolymers," *ACS nano*, vol. 6, no. 3, pp. 2629–2641, 2012.
- [77] I. P. Campbell, S. Hirokawa, and M. P. Stoykovich, "Processing approaches for the defect engineering of lamellar-forming block copolymers in thin films," *Macromolecules*, vol. 46, no. 24, pp. 9599–9608, 2013.
- [78] S. Choi, E. Kim, H. Ahn, S. Naidu, Y. Lee, D. Y. Ryu, C. J. Hawker, and T. P. Russell, "Lamellar microdomain orientation and phase transition of polystyrene-*b*-poly (methyl methacrylate) films by controlled interfacial interactions," *Soft Matter*, vol. 8, no. 12, pp. 3463–3469, 2012.
- [79] E. Sivaniah, Y. Hayashi, S. Matsubara, S. Kiyono, T. Hashimoto, K. Fukunaga, E. J. Kramer, and T. Mates, "Symmetric diblock copolymer thin films on rough substrates. kinetics and structure formation in pure block copolymer thin films," *Macromolecules*, vol. 38, no. 5, pp. 1837–1849, 2005.
- [80] S. M. Park, B. C. Berry, E. Dobisz, and H.-C. Kim, "Observation of surface corrugation-induced alignment of lamellar microdomains in PS-*b*-PMMA thin films," *Soft Matter*, vol. 5, pp. 957–961, Feb. 2009.
- [81] C. Harrison, P. M. Chaikin, D. A. Huse, R. A. Register, D. H. Adamson, A. Daniel, E. Huang, P. Mansky, T. Russell, E. D. A. I. V. Hawker, Craig J, and B. Eberhard, "Reducing substrate pinning of block copolymer microdomains with a buffer layer of polymer brushes," *Macromolecules*, vol. 33, no. 3, pp. 857–865, 2000.

- [82] Y. S. Jung and C. A. Ross, "Orientation-controlled self-assembled nanolithography using a polystyrene-polydimethylsiloxane block copolymer," *Nano letters*, vol. 7, no. 7, pp. 2046–2050, 2007.
- [83] J. K. Bosworth, E. A. Dobisz, O. Hellwig, and R. Ruiz, "Impact of Out-of-Plane Translational Order in Block Copolymer Lithography," *Macromolecules*, vol. 44, no. 23, pp. 9196–9204, 2011.
- [84] D. M. Trombly, V. Pryamitsyn, and V. Ganesan, "Surface Energies and Self-Assembly of Block Copolymers on Grafted Surfaces," *Physical Review Letters*, vol. 107, no. 14, p. 148304, 2011.
- [85] D. M. Trombly, V. Pryamitsyn, and V. Ganesan, "Self-assembly of diblock copolymer on substrates modified by random copolymer brushes," vol. 44, no. 24, pp. 9867–9881, 2011.
- [86] G. M. Perera, C. Wang, M. Doxastakis, R. J. Kline, W.-l. Wu, A. W. Bosse, and G. E. Stein, "Directed self-assembly of lamellar copolymers: Effects of interfacial interactions on domain shape," vol. 1, no. 11, pp. 1244–1248, 2012.
- [87] A. Ramirez-Hernandez, H. S. Suh, P. F. Nealey, and J. J. de Pablo, "Control of directed self-assembly in block polymers by polymeric topcoats," *Macromolecules*, vol. 47, no. 10, pp. 3520–3527, 2014.
- [88] R. Guo, E. Kim, J. Gong, S. Choi, and S. Ham, "Perpendicular orientation of microdomains in ps-b-pmma thin films on the ps brushed substrates," *Soft Matter*, vol. 7, no. 15, pp. 6920–6925, 2011.

- [89] X. Zhang, F. K. Lee, and O. K. Tsui, “Wettability of end-grafted polymer brush by chemically identical polymer films,” *Macromolecules*, vol. 41, no. 21, pp. 8148–8151, 2008.
- [90] Y. Zhao, E. Sivaniah, and T. Hashimoto, “SAXS analysis of the order-disorder transition and the interaction parameter of polystyrene-block-poly(methyl methacrylate),” *Macromolecules*, vol. 41, no. 24, pp. 9948–9951, 2008.
- [91] Z. Jiang, X. Li, J. Strzalka, M. Sprung, T. Sun, A. R. Sandy, S. Narayanan, D. R. Lee, and J. Wang, “The dedicated high-resolution grazing-incidence X-ray scattering beamline 8-ID-E at the Advanced Photon Source,” *Journal of Synchrotron Radiation*, vol. 19, no. 4, pp. 627–636, 2012.
- [92] L. G. Parratt, “Surface studies of solids by total reflection of x-rays,” *Physical Review*, vol. 95, no. 2, pp. 359–369, 1954.
- [93] M. Tolan, *X-Ray Scattering from Soft-Matter Thin Films: Materials Science and Basic Research*. Springer Tracts in Modern Physics, 1999.
- [94] S. Wu, “Polymer interface and adhesion,” *Journal of Polymer Science Part C: Polymer Symposia*, vol. 34, p. 19, 1971.
- [95] S. Wu, “Polar and nonpolar interactions in adhesion,” *Journal of Adhesion*, vol. 5, pp. 39–55, 1973.
- [96] Z. Jiang, D. R. Lee, S. Narayanan, J. Wang, and S. K. Sinha, “Waveguide-enhanced grazing-incidence small-angle x-ray scattering of buried nanostructures in thin films,” *Physical Review B*, vol. 84, no. 7, p. 075440, 2011.

- [97] S. Wu, "Surface and interfacial tensions of polymer melts. ii. poly (methyl methacrylate), poly (n-butyl methacrylate), and polystyrene," *The Journal of Physical Chemistry*, vol. 74, no. 3, pp. 632–638, 1970.
- [98] Y. Kitazaki and T. Hata, "Surface-chemical criteria for optimum adhesion: Ii. the variability of critical surface tension (γ_c) and its choice," *The Journal of Adhesion*, vol. 4, no. 2, pp. 123–132, 1972.
- [99] J. Dann, "Forces involved in the adhesive process: I. critical surface tensions of polymeric solids as determined with polar liquids," *Journal of Colloid and Interface Science*, vol. 32, no. 2, pp. 302–320, 1970.
- [100] B. Jańczuk and T. Białłopiotrowicz, "Surface free-energy components of liquids and low energy solids and contact angles," *Journal of colloid and interface science*, vol. 127, no. 1, pp. 189–204, 1989.
- [101] S. Kim, C. M. Bates, A. Thio, J. D. Cushen, C. J. Ellison, C. G. Willson, and F. S. Bates, "Consequences of Surface Neutralization in Diblock Copolymer Thin Films," *ACS Nano*, vol. 7, no. 11, pp. 9905–9919, 2013.
- [102] M. Luo, J. E. Seppala, J. N. L. Albert, R. L. Lewis, N. Mahadevapuram, G. E. Stein, and T. H. Epps, "Manipulating nanoscale morphologies in cylinder-forming poly(styrene-b-isoprene-b-styrene) thin films using film thickness and substrate surface chemistry gradients," *Macromolecules*, vol. 46, no. 5, pp. 1803–1811, 2013.
- [103] H. Ahn, C. Shin, B. Lee, and D. Y. Ryu, "Phase transitions of block copolymer film on homopolymer-grafted substrate," vol. 43, no. 4, pp. 1958–1963, 2010.

- [104] G. Coulon, B. Collin, D. Ausserre, D. Chatenay, and T. Russell, “Islands And Holes On The Free-Surface Of Thin Diblock Copolymer Films .1. Characteristics Of Formation And Growth,” *Journal de Physique*, vol. 51, no. 24, pp. 2801–2811, 1990.
- [105] E. Choi, S. Park, H. Ahn, M. Lee, J. Bang, B. Lee, and D. Y. Ryu, “Substrate-independent lamellar orientation in high-molecular-weight polystyrene-b-poly(methyl methacrylate) films: Neutral solvent vapor and thermal annealing effect,” *Macromolecules*, vol. 47, no. 12, pp. 3969–3977, 2014.
- [106] N. Koneripalli, F. Bates, and G. Fredrickson, “Fractal hole growth in strained block copolymer films,” *Physical Review Letters*, vol. 81, no. 9, pp. 1861–1864, 1998.
- [107] R. Peters and K. Dalnoki-Veress, “Film thickness dependent ordering dynamics of lamellar forming diblock copolymer thin films,” *The European Physical Journal E*, vol. 35, no. 12, 2012.
- [108] I. Park, S. Park, H.-W. Park, T. Chang, H. Yang, and C. Y. Ryu, “Unexpected hexagonally perforated layer morphology of ps-b-pmma block copolymer in supported thin film,” vol. 39, no. 1, pp. 315–318, 2006.
- [109] S. Ji, C. C. Liu, W. Liao, A. L. Fenske, G. S. Craig, and P. F. Nealey, “Domain orientation and grain coarsening in cylinder-forming poly (styrene-b-methyl methacrylate) films,” vol. 44, no. 11, pp. 4291–4300, 2011.
- [110] D. W. Janes, C. J. Thode, C. G. Willson, P. F. Nealey, and C. J. Ellison, “Light-Activated Replication of Block Copolymer Fingerprint Patterns,” *Macromolecules*, vol. 46, no. 11, pp. 4510–4519, 2013.

- [111] G. Stein, E. Kramer, X. Li, and J. Wang, "Layering transitions in thin films of spherical-domain block copolymers," *Macromolecules*, vol. 40, no. 7, pp. 2453–2460, 2007.
- [112] P. Mueller-Buschbaum, E. Maurer, E. Bauer, and R. Cubitt, "Surface versus confinement induced morphology transition in triblock copolymer films: A grazing incidence small angle neutron scattering investigation," *Langmuir*, vol. 22, no. 22, pp. 9295–9303, 2006.
- [113] B. Lee, I. Park, J. Yoon, S. Park, J. Kim, K. Kim, T. Chang, and M. Ree, "Structural analysis of block copolymer thin films with grazing incidence small-angle X-ray scattering," *Macromolecules*, vol. 38, no. 10, pp. 4311–4323, 2005.
- [114] G. Renaud, R. Lazzari, and F. Leroy, "Probing surface and interface morphology with Grazing Incidence Small Angle X-Ray Scattering," *Surface Science Reports*, vol. 64, no. 8, pp. 255–380, 2009.
- [115] Deterministic approaches are appropriate when fitting with a limited set of parameters. However, if more parameters were included to describe complex domain shapes, then nonlinear regression would likely fail.
- [116] H. Yoshida, H. S. Suh, A. Ramirez-Hernandez, J. I. Lee, K. Aida, L. Wan, Y. Ishida, Y. Tada, R. Ruiz, J. de Pablo, and P. F. Nealey, "Topcoat approaches for directed self-assembly of strongly segregating block copolymer thin films," *Journal of Photopolymer Science and Technology*, vol. 26, no. 1, pp. 55–58, 2013.
- [117] G. Wilmes, D. Durkee, N. Balsara, and J. Liddle, "Bending soft block copolymer nanostructures by lithographically directed assembly," *Macromolecules*, vol. 39, no. 7, pp. 2435–2437, 2006.

- [118] S.-M. Park, M. Dong, C. T. Rettner, D. S. Dandy, Q. Wang, and H.-C. Kim, "Bending of Lamellar Microdomains of Block Copolymers on Nonselective Surfaces," *Macromolecules*, vol. 43, no. 3, pp. 1665–1670, 2010.
- [119] Z. G. Wang, "Response and instabilities of the lamellar phase of diblock copolymers under uniaxial-stress," *Journal of Chemical Physics*, vol. 100, no. 3, pp. 2298–2309, 1994.
- [120] H. Lee, J. Pietrasik, S. S. Sheiko, and K. Matyjaszewski, "Stimuli-responsive molecular brushes," *Progress in Polymer Science*, vol. 35, no. 1, pp. 24–44, 2010.
- [121] Y. Xia, B. D. Olsen, J. A. Kornfield, and R. H. Grubbs, "Efficient synthesis of narrowly dispersed brush copolymers and study of their assemblies: the importance of side chain arrangement," *Journal of the American Chemical Society*, vol. 131, no. 51, pp. 18525–18532, 2009.
- [122] Y. Xia, J. A. Kornfield, and R. H. Grubbs, "Efficient synthesis of narrowly dispersed brush polymers via living ring-opening metathesis polymerization of macromonomers," *Macromolecules*, vol. 42, no. 11, pp. 3761–3766, 2009.
- [123] Z. Li, K. Zhang, J. Ma, C. Cheng, and K. L. Wooley, "Facile syntheses of cylindrical molecular brushes by a sequential RAFT and ROMP "grafting-through" methodology," *Journal of Polymer Science Part A: Polymer Chemistry*, vol. 47, no. 20, pp. 5557–5563, 2009.
- [124] J. A. Johnson, Y. Y. Lu, A. O. Burts, Y. Xia, A. C. Durrell, D. A. Tirrell, and R. H. Grubbs, "Drug-loaded, bivalent-bottle-brush polymers by graft-through ROMP," *Macromolecules*, vol. 43, no. 24, pp. 10326–10335, 2010.

- [125] Z. Li, J. Ma, C. Cheng, K. Zhang, and K. L. Wooley, "Synthesis of heterografted amphiphilic diblock molecular brushes and their self-assembly in aqueous medium," *Macromolecules*, vol. 43, no. 3, pp. 1182–1184, 2010.
- [126] K. Huang and J. Rzayev, "Well-defined organic nanotubes from multicomponent bottlebrush copolymers," *Journal of the American Chemical Society*, vol. 131, no. 19, pp. 6880–6885, 2009.
- [127] S. Jha, S. Dutta, and N. B. Bowden, "Synthesis of ultralarge molecular weight bottlebrush polymers using Grubbs' catalysts," *Macromolecules*, vol. 37, no. 12, pp. 4365–4374, 2004.
- [128] G. M. Miyake, V. A. Piunova, R. A. Weitekamp, and R. H. Grubbs, "Precisely Tunable Photonic Crystals From Rapidly Self-Assembling Brush Block Copolymer Blends," *Angewandte Chemie International Edition*, vol. 51, no. 45, pp. 11246–11248, 2012.
- [129] G. M. Miyake, R. A. Weitekamp, V. A. Piunova, and R. H. Grubbs, "Synthesis of Isocyanate-Based Brush Block Copolymers and Their Rapid Self-Assembly to Infrared-Reflecting Photonic Crystals," *Journal of the American Chemical Society*, vol. 134, no. 34, pp. 14249–14254, 2012.
- [130] X. Banquy, J. Burdynska, D. W. Lee, K. Matyjaszewski, and J. Israelachvili, "Bioinspired Bottle-Brush Polymer Exhibits Low Friction and Amontons-like Behavior," *Journal of the American Chemical Society*, vol. 136, no. 17, pp. 6199–6202, 2014.
- [131] S. J. Dalsin, M. A. Hillmyer, and F. S. Bates, "Molecular Weight Dependence of Zero-Shear Viscosity in Atactic Polypropylene Bottlebrush Polymers," *ACS Macro Letters*, vol. 3, no. 5, pp. 423–427, 2014.

- [132] M. Hu, Y. Xia, G. B. McKenna, J. A. Kornfield, and R. H. Grubbs, "Linear rheological response of a series of densely branched brush polymers," *Macromolecules*, vol. 44, no. 17, pp. 6935–6943, 2011.
- [133] S. K. Kumar, N. Jouault, B. Benicewicz, and T. Neely, "Nanocomposites with polymer grafted nanoparticles," *Macromolecules*, vol. 46, no. 9, pp. 3199–3214, 2013.
- [134] Y. N. Pandey, G. J. Papakonstantopoulos, and M. Doxastakis, "Polymer/nanoparticle interactions: Bridging the gap," *Macromolecules*, vol. 46, no. 13, pp. 5097–5106, 2013.
- [135] F. C. Sun, A. V. Dobrynin, D. Shirvanyants, H.-I. Lee, K. Matyjaszewski, G. J. Rubinstein, M. Rubinstein, and S. S. Sheiko, "Flory theorem for structurally asymmetric mixtures," *Physical review letters*, vol. 99, no. 13, p. 137801, 2007.
- [136] F. S. Bates and G. D. Wignall, "Isotope-induced quantum-phase transitions in the liquid state," *Physical review letters*, vol. 57, no. 12, p. 1429, 1986.
- [137] R. A. Jones, E. J. Kramer, M. H. Rafailovich, J. Sokolov, and S. A. Schwarz, "Surface enrichment in an isotopic polymer blend," *Physical review letters*, vol. 62, no. 3, p. 280, 1989.
- [138] M. Li, P. De, S. R. Gondi, and B. S. Sumerlin, "End group transformations of RAFT-generated polymers with bismaleimides: Functional telechelics and modular block copolymers," *Journal of Polymer Science Part A: Polymer Chemistry*, vol. 46, no. 15, pp. 5093–5100, 2008.

- [139] M. Li, P. De, H. Li, and B. S. Sumerlin, "Conjugation of RAFT-generated polymers to proteins by two consecutive thiol-ene reactions," *Polymer Chemistry*, vol. 1, no. 6, pp. 854–859, 2010.
- [140] N. Hadjichristidis, H. Iatrou, S. Pispas, and M. Pitsikalis, "Anionic polymerization: high vacuum techniques," *Journal of Polymer Science Part A: Polymer Chemistry*, vol. 38, no. 18, pp. 3211–3234, 2000.
- [141] D. Uhrig and J. W. Mays, "Experimental techniques in high-vacuum anionic polymerization," *Journal of Polymer Science Part A: Polymer Chemistry*, vol. 43, no. 24, pp. 6179–6222, 2005.
- [142] E. J. Kramer, "Depth profiling methods that provide information complementary to neutron reflectivity," *Physica B: Condensed Matter*, vol. 173, no. 1, pp. 189–198, 1991.
- [143] J. W. Chan, B. Yu, C. E. Hoyle, and A. B. Lowe, "The nucleophilic, phosphine-catalyzed thiol-ene click reaction and convergent star synthesis with RAFT-prepared homopolymers," *Polymer*, vol. 50, no. 14, pp. 3158–3168, 2009.
- [144] S. L. Pesek, X. Li, B. Hammouda, K. Hong, and R. Verduzco, "Small-Angle Neutron Scattering Analysis of Bottlebrush Polymers Prepared via Grafting-Through Polymerization," *Macromolecules*, vol. 46, no. 17, pp. 6998–7005, 2013.
- [145] I. I. Potemkin, A. R. Khokhlov, and P. Reineker, "Stiffness and conformations of molecular bottle-brushes strongly adsorbed on a flat surface," *The European Physical Journal E*, vol. 4, no. 1, pp. 93–101, 2001.
- [146] G. H. Fredrickson, "Surfactant-induced lyotropic behavior of flexible polymer solutions," *Macromolecules*, vol. 26, no. 11, pp. 2825–2831, 1993.

- [147] T. M. Birshtein, O. V. Borisov, Y. B. Zhulina, A. R. Khokhlov, and T. A. Yurasova, “Conformations of comb-like macromolecules,” *Polymer Science USSR*, vol. 29, no. 6, pp. 1293–1300, 1987.
- [148] H. B. Eitouni and N. P. Balsara, “Thermodynamics of polymer blends,” in *Physical Properties of Polymers Handbook*, pp. 339–356, Springer, 2007.
- [149] M. W. Matsen and J. M. Gardiner, “Autophobic dewetting of homopolymer on a brush and entropic attraction between opposing brushes in a homopolymer matrix,” *The Journal of Chemical Physics*, vol. 115, no. 6, pp. 2794–2804, 2001.
- [150] D. M. Trombly and V. Ganesan, “Curvature effects upon interactions of polymer-grafted nanoparticles in chemically identical polymer matrices,” *The Journal of chemical physics*, vol. 133, no. 15, p. 154904, 2010.
- [151] A. L. Frischknecht, M. J. Hore, J. Ford, and R. J. Composto, “Dispersion of polymer-grafted nanorods in homopolymer films: theory and experiment,” *Macromolecules*, vol. 46, no. 7, pp. 2856–2869, 2013.
- [152] D. Sunday, J. Ilavsky, and D. L. Green, “A phase diagram for polymer-grafted nanoparticles in homopolymer matrices,” *Macromolecules*, vol. 45, no. 9, pp. 4007–4011, 2012.
- [153] P. F. Green, “The structure of chain end-grafted nanoparticle/homopolymer nanocomposites,” *Soft Matter*, vol. 7, no. 18, pp. 7914–7926, 2011.
- [154] L. Meli, A. Arceo, and P. F. Green, “Control of the entropic interactions and phase behavior of athermal nanoparticle/homopolymer thin film mixtures,” *Soft Matter*, vol. 5, no. 3, pp. 533–537, 2009.

- [155] J. Kim and P. F. Green, "Phase behavior of thin film brush-coated nanoparticles/homopolymer mixtures," *Macromolecules*, vol. 43, no. 3, pp. 1524–1529, 2010.
- [156] C. Chevigny, J. Jestin, D. Gigmes, R. Schweins, E. Di-Cola, F. Dalmas, D. Bertin, and F. Boué, "'wet-to-dry' conformational transition of polymer layers grafted to nanoparticles in nanocomposite," *Macromolecules*, vol. 43, no. 11, pp. 4833–4837, 2010.
- [157] A. Bansal, H. Yang, C. Li, B. C. Benicewicz, S. K. Kumar, and L. S. Schadler, "Controlling the thermomechanical properties of polymer nanocomposites by tailoring the polymer-particle interface," *Journal of Polymer Science Part B: Polymer Physics*, vol. 44, no. 20, pp. 2944–2950, 2006.
- [158] M. D. Foster, C. C. Greenberg, D. M. Teale, C. M. Turner, S. Corona-Galvan, E. Cloutet, P. D. Butler, B. Hammouda, and R. P. Quirk, "Effective χ and surface segregation in blends of star and linear polystyrene," *Macromolecular Symposia*, vol. 149, no. 1, pp. 263–268, 2000.
- [159] D. T. Wu and G. H. Fredrickson, "Effect of architecture in the surface segregation of polymer blends," *Macromolecules*, vol. 29, no. 24, pp. 7919–7930, 1996.
- [160] J. P. Donley, D. T. Wu, and G. H. Fredrickson, "On the control of surface enrichment in polymer blends and copolymers," *Macromolecules*, vol. 30, no. 7, pp. 2167–2174, 1997.
- [161] E. S. McGarrity, A. L. Frischknecht, L. J. D. Frink, and M. E. Mackay, "Surface-induced first-order transition in athermal polymer-nanoparticle blends," *Physical review letters*, vol. 99, no. 23, p. 238302, 2007.

- [162] R. S. Krishnan, M. E. Mackay, C. J. Hawker, and B. Van Horn, "Influence of molecular architecture on the dewetting of thin polystyrene films," vol. 21, no. 13, pp. 5770–5776, 2005.
- [163] A. Hariharan, S. K. Kumar, M. H. Rafailovich, J. Sokolov, X. Zheng, D. Duong, S. A. Schwarz, and T. P. Russell, "The effect of finite film thickness on the surface segregation in symmetric binary polymer mixtures," *The Journal of chemical physics*, vol. 99, no. 1, pp. 656–663, 1993.
- [164] J. S. Lee, M. D. Foster, and D. T. Wu, "Effects of branch points and chain ends on the thermodynamic interaction parameter in binary blends of regularly branched and linear polymers," *Macromolecules*, vol. 39, no. 15, pp. 5113–5121, 2006.
- [165] J. Kamada, K. Koynov, C. Corten, A. Juhari, J. A. Yoon, M. W. Urban, A. C. Balazs, and K. Matyjaszewski, "Redox responsive behavior of thiol/disulfide-functionalized star polymers synthesized via atom transfer radical polymerization," *Macromolecules*, vol. 43, no. 9, pp. 4133–4139, 2010.
- [166] A. Striolo and J. M. Prausnitz, "Adsorption of branched homopolymers on a solid surface," *The Journal of Chemical Physics*, vol. 114, no. 19, pp. 8565–8572, 2001.
- [167] D. A. Hajduk, P. E. Harper, S. M. Gruner, C. C. Honeker, G. Kim, E. L. Thomas, and L. J. Fetters, "The gyroid: A new equilibrium morphology in weakly segregated diblock copolymers," *Macromolecules*, vol. 27, no. 15, pp. 4063–4075, 1994.

- [168] L. Rockford, S. G. J. Mochrie, and T. P. Russell, "Propagation of nanopatterned substrate templated ordering of block copolymers in thick films," *Macromolecules*, vol. 34, no. 5, pp. 1487–1492, 2001.
- [169] H. C. Kim, S. M. Park, and W. D. Hinsberg, "Block copolymer based nanostructures: materials, processes, and applications to electronics," vol. 110, no. 1, pp. 146–177, 2009.
- [170] C. Liu, P. Nealey, Y.-H. Ting, and A. Wendt, "Pattern transfer using poly(styrene-block-methyl methacrylate) copolymer films and reactive ion etching," *Journal of Vacuum Science & Technology B*, vol. 25, no. 6, pp. 1963–1968, 2007. 51st International Conference on Electron, Ion, and Photon Beam Technology and Nanofabrication, Denver, CO, MAY 29-JUN 01, 2007.
- [171] L. Oria, A. R. de Luzuriaga, J. A. Alduncín, and F. Pérez-Murano, "Block copolymer guided self-assembly by surface chemical modification: optimization of multiple patterning process and pattern transfer," 2012.
- [172] C. Tang, E. M. Lennon, G. H. Fredrickson, E. J. Kramer, and C. J. Hawker, "Evolution of block copolymer lithography to highly ordered square arrays," *Science*, vol. 322, no. 5900, pp. 429–432, 2008.
- [173] Y. C. Tseng and S. B. Darling, "Block copolymer nanostructures for technology," *Polymers*, vol. 2, no. 4, pp. 470–489, 2010.
- [174] K. A. Tavakkoli, K. W. Gotrik, A. F. Hannon, A. Alexander-Katz, C. A. Ross, and K. K. Berggren, "Templating three-dimensional self-assembled structures in bilayer block copolymer films," *Science*, vol. 336, no. 6086, pp. 1294–1298, 2012.

- [175] S. Kim, H. Solak, M. Stoykovich, N. Ferrier, J. de Pablo, and P. Nealey, “Epitaxial self-assembly of block copolymers on lithographically defined nanopatterned substrates,” *Nature*, vol. 424, no. 6947, pp. 411–414, 2003.
- [176] A. P. Marencic and R. A. Register, “Controlling order in block copolymer thin films for nanopatterning applications,” *Annual Review of Chemical and Biomolecular Engineering*, vol. 1, pp. 277–297, 2010.
- [177] D. M. Smilgies, P. Busch, C. M. Papadakis, and D. Posselt, “Characterization of polymer thin films with small-angle x-ray scattering under grazing incidence (gisaxs),” 2002.
- [178] G. Stein, W. Lee, G. Fredrickson, E. Kramer, X. Li, and J. Wang, “Thickness dependent ordering in laterally confined monolayers of spherical-domain block copolymers,” *Macromolecules*, vol. 40, no. 16, pp. 5791–5800, 2007.
- [179] M. Komura, K. Watanabe, T. Iyoda, T. Yamada, H. Yoshida, and Y. Iwasaki, “Laboratory-GISAXS measurements of block copolymer films with highly ordered and normally oriented nanocylinders,” *Chemistry Letters*, vol. 38, no. 5, pp. 408–409, 2009.
- [180] C. Tang, J. Bang, G. E. Stein, G. H. Fredrickson, C. J. Hawker, E. J. Kramer, M. Sprung, and J. Wang, “Square packing and structural arrangement of ABC triblock copolymer spheres in thin films,” *Macromolecules*, vol. 41, no. 12, pp. 4328–4339, 2008.
- [181] S. Xiao, X. M. Yang, E. W. Edwards, Y. H. La, and P. F. Nealey, “Graphoepitaxy of cylinder-forming block copolymers for use as templates to pattern magnetic metal dot arrays,” *Nanotechnology*, vol. 16, no. 7, p. S324, 2005.

- [182] S. Kim, B. Kim, D. Meng, D. Shin, C. Koo, H. Solak, and Q. Wang, “Novel Complex Nanostructure from Directed Assembly of Block Copolymers on Incommensurate Surface Patterns,” *Advanced Materials*, vol. 19, no. 20, pp. 3271–3275, 2007.
- [183] G. Stein, J. Liddle, A. Aquila, and E. Gullikson, “Measuring the Structure of Epitaxially Assembled Block Copolymer Domains with Soft X-ray Diffraction,” *Macromolecules*, vol. 43, no. 1, pp. 433–441, 2010.
- [184] E. W. Edwards, M. F. Montague, H. H. Solak, C. J. Hawker, and P. F. Nealey, “Precise control over molecular dimensions of block-copolymer domains using the interfacial energy of chemically nanopatterned substrates,” *Advanced Materials*, vol. 16, no. 15, pp. 1315–1319, 2004.
- [185] J. Y. Cheng, C. A. Ross, H. I. Smith, and E. L. Thomas, “Templated self-assembly of block copolymers: Top-down helps bottom-up,” *Advanced Materials*, vol. 18, no. 19, pp. 2505–2521, 2006.
- [186] E. Kim, H. Ahn, S. Park, H. Lee, M. Lee, S. Lee, T. Kim, E.-A. Kwak, J. H. Lee, X. Lei, and others, “Directed assembly of high molecular weight block copolymers: highly ordered line patterns of perpendicularly oriented lamellae with large periods,” *ACS nano*, vol. 7, no. 3, pp. 1952–1960, 2013.
- [187] M. P. Stoykovich, K. C. Daoulas, M. MuñLler, H. Kang, J. J. de Pablo, and P. F. Nealey, “Remediation of line edge roughness in chemical nanopatterns by the directed assembly of overlying block copolymer films,” *Macromolecules*, vol. 43, no. 5, pp. 2334–2342, 2010.

- [188] A. W. Bosse, "Phase-Field Simulation of Long-Wavelength Line Edge Roughness in Diblock Copolymer Resists," *Macromolecular Theory and Simulations*, vol. 19, no. 7, pp. 399–406, 2010.
- [189] C. C. Chao, T.-C. Wang, R. M. Ho, P. Georgopoulos, A. Avgeropoulos, and E. L. Thomas, "Robust block copolymer mask for nanopatterning polymer films," *ACS nano*, vol. 4, no. 4, pp. 2088–2094, 2010.
- [190] J. W. Jeong, W. I. Park, M. J. Kim, C. A. Ross, and Y. S. Jung, "Highly tunable self-assembled nanostructures from a poly (2-vinylpyridine-*b*-dimethylsiloxane) block copolymer," *Nano letters*, vol. 11, no. 10, pp. 4095–4101, 2011.
- [191] E. Huang, T. Russell, C. Harrison, P. Chaikin, R. Register, C. Hawker, and J. Mays, "Using surface active random copolymers to control the domain orientation in diblock copolymer thin films," *Macromolecules*, vol. 31, no. 22, pp. 7641–7650, 1998.
- [192] C. M. Bates, T. Seshimo, M. J. Maher, W. J. Durand, J. D. Cushen, L. M. Dean, G. Blachut, C. J. Ellison, and C. G. Willson, "Polarity-Switching Top Coats Enable Orientation of Sub-10-nm Block Copolymer Domains," *Science*, vol. 338, no. 6108, pp. 775–779, 2012.
- [193] I. Mitra, X. Li, S. L. Pesek, B. Makarenko, B. S. Lokitz, D. Uhrig, J. F. Ankner, R. Verduzco, and G. E. Stein, "Thin Film Phase Behavior of Bottlebrush/Linear Polymer Blends," *Macromolecules*, vol. 47, no. 15, pp. 5269–5276, 2014.

Appendix A

X-ray reflectivity measurements from polymer brushes: Polymer brush thicknesses were calculated from X-ray reflectivity measurements. Results are reported in Figure A.1, where circles (blue) and lines (red) denote the data and best-fit to the Parratt recursions, respectively. The calculated brush thicknesses are 6.2 nm, 4.8 nm, 4.4 nm, 3.4 nm and 2.6 nm.

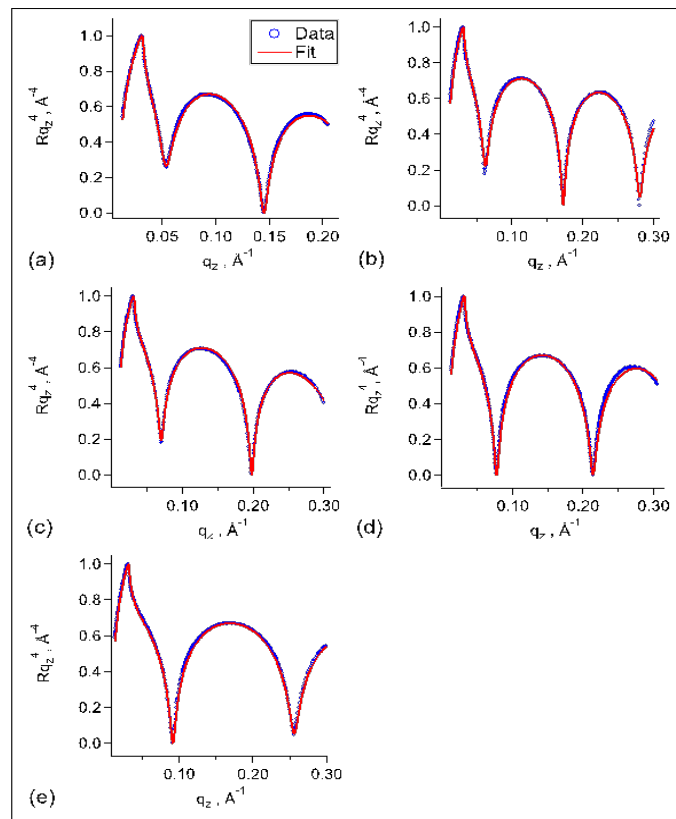


Figure A.1: Brush thicknesses from X-ray reflectivity. Best fit results in (a-e) are 6.2 nm, 4.8 nm, 4.4 nm, 3.4 nm and 2.6 nm, respectively.

Comparison of AFM/SEM in calculation of orientational correlation length:
length:

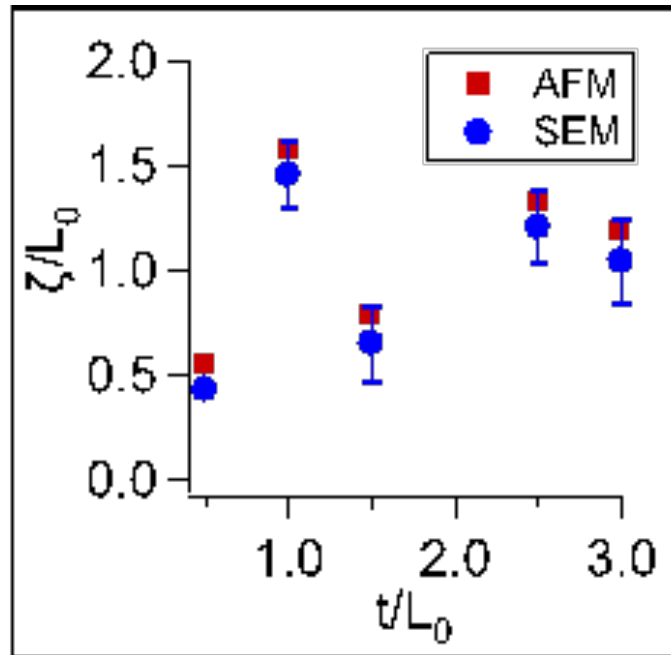


Figure A.2: Normalized orientational correlation length as a function of normalized film thickness.

Stability of perpendicular lamellar orientation at elevated temperature: Perpendicular lamellae are detected at the air interface when annealed at 240 °C for 10 min (in air). To verify that this orientation is stable, we further annealed one set of films at 230 °C for 6 hours (under low vacuum). (The surface tensions of PS and PMMA are identical above 220 °C. The annealing schedule of 230 °C and 6 hours was employed in the studies from Bates, Willson, and coworkers that are referenced in the manuscript.) The outcomes of this experiment are reported in Figure A.3 below and Figure A.4 on the following page.

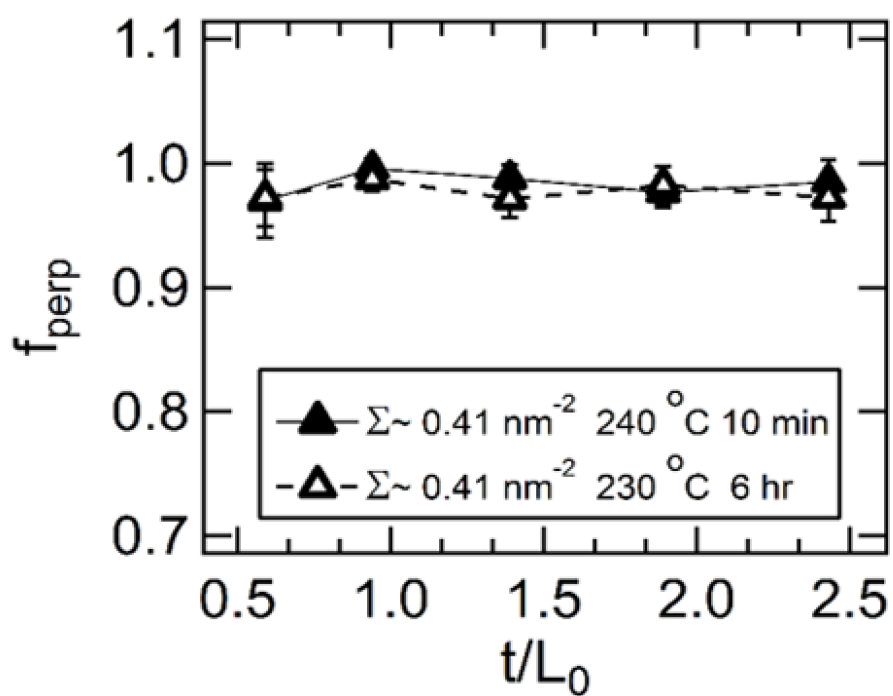


Figure A.3: Area fraction of perpendicular lamellae (f_{perp}) as a function of normalized film thickness (t/L_0) and annealing time.

Microscopy images for PS-PMMA films annealed at 230 °C:

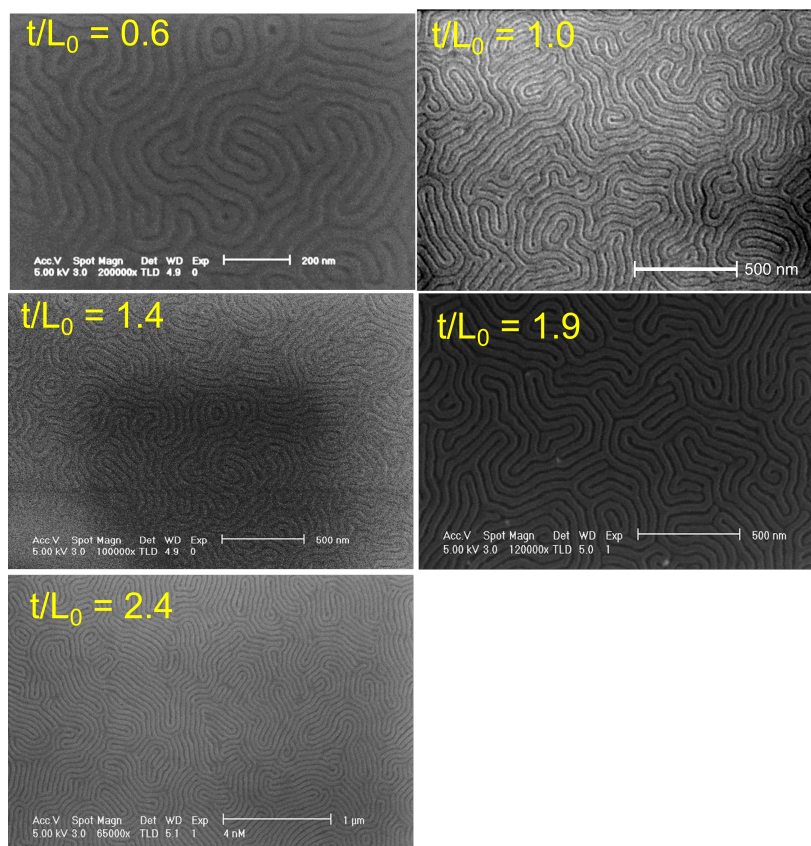


Figure A.4: Perpendicular lamellae are detected after annealing for 6 hours at 230 °C. Normalized film thickness is noted on each image.

Effect of film thickness and grafting density (lowest two):

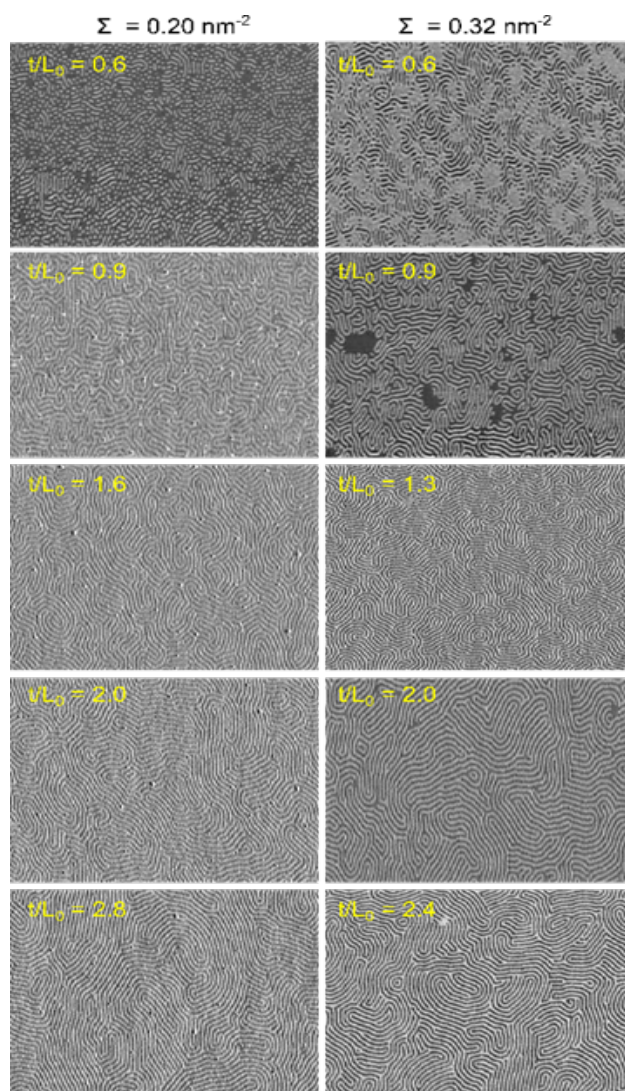


Figure A.5: Surface microscopy images as a function of film thickness and grafting densities. Image width = $3 \mu\text{m}$.

Effect of film thickness and grafting density (highest three):

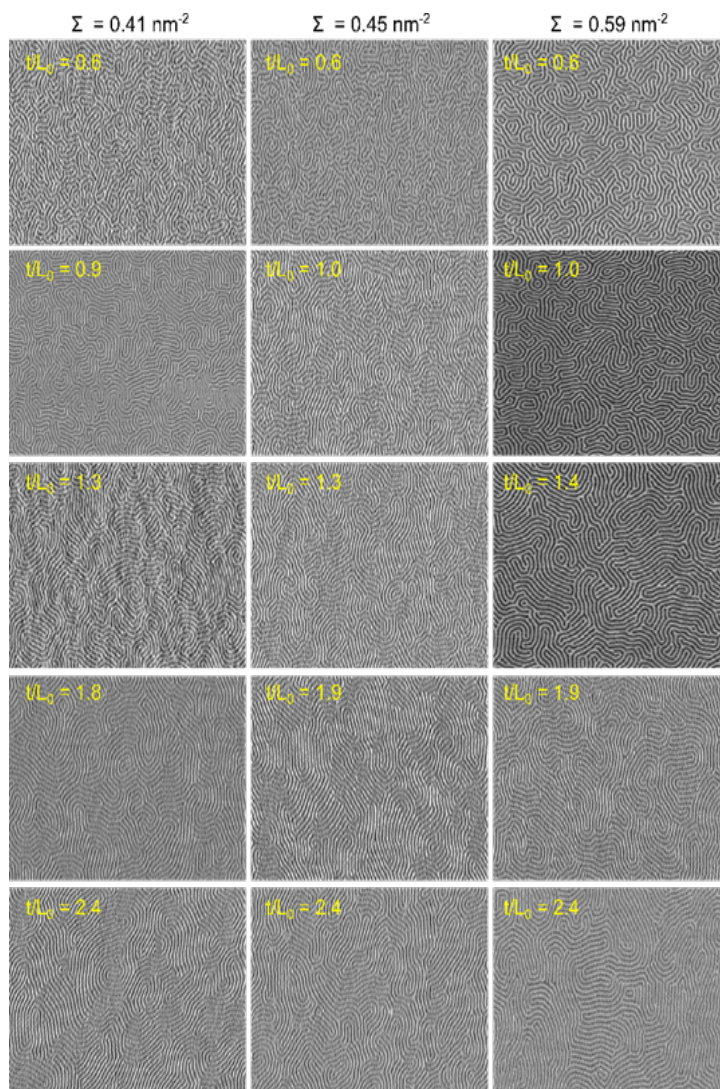


Figure A.6: Surface microscopy images as a function of film thickness and grafting densities. Image width = 3 μm .

Line shape as a function of film thickness: The in-plane line shape becomes narrower as film thickness is increased. Line profiles $I(q_y)$ were extracted from GISAXS data and fit to a Lorentzian function, as demonstrated by Figure A.7(a). The full width at half maximum (FWHM) is reported in Figure A.7(b) for two data sets (each set has a fixed brush grafting density and composition, with two PS-PMMA film thicknesses). Thinner films have broader line shapes, which is evidence of reduced orientational order. The line shape is generally independent of incident angle.

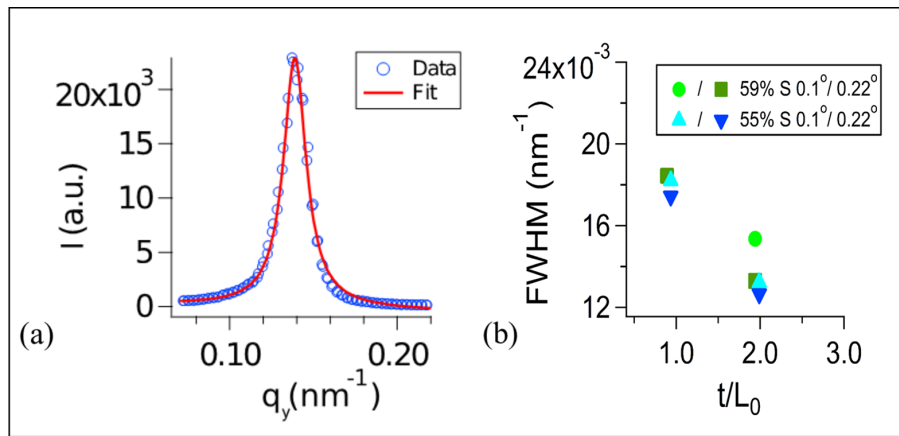


Figure A.7: (a) In-plane line shape example; (b) FWHM as a function of normalized film thickness.

Line cuts as a function of film thickness: In-plane line cuts for each film thickness were extracted from data acquired with an incidence angle of 0.22° . Data are shown for two data sets having brush grafting densities of 0.32 nm^{-2} and 0.59 nm^{-2} . Neither show a strong second or fourth-order peak, which is consistent with scattering expected for an equal-volume lamellar copolymer. There is also no evidence of hexagonal structure in any samples (including other grafting densities).

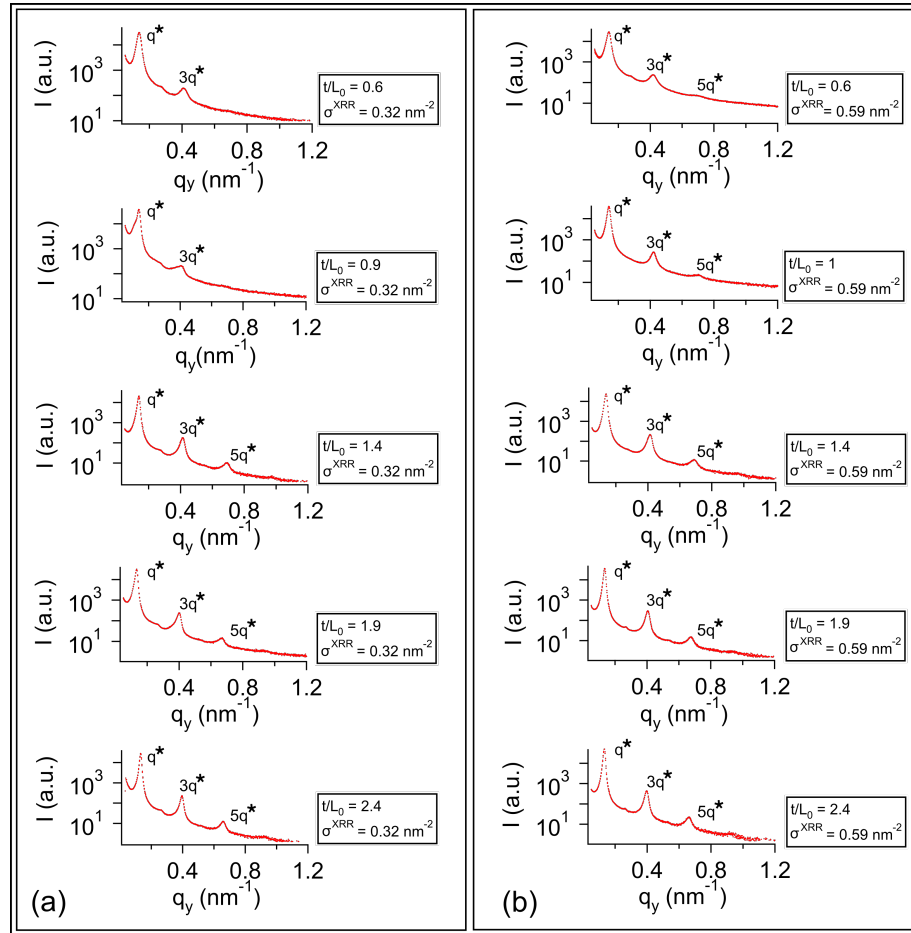


Figure A.8: Plots of intensity (I) versus scattering vector (q_y) for PS-PMMA thin films on brushes with Σ (a) 0.32 nm^{-2} , and (b) 0.59 nm^{-2} . The first-order peak is denoted as q^* .

SEM cross-section: Films were cleaved, etched for a few seconds in oxygen plasma, and then mounted at near-vertical angles in an SEM for cross-sectional imaging. The image quality is not good enough for quantitative analysis, but domains having different orientations are detected. Examples are included in the following figures.

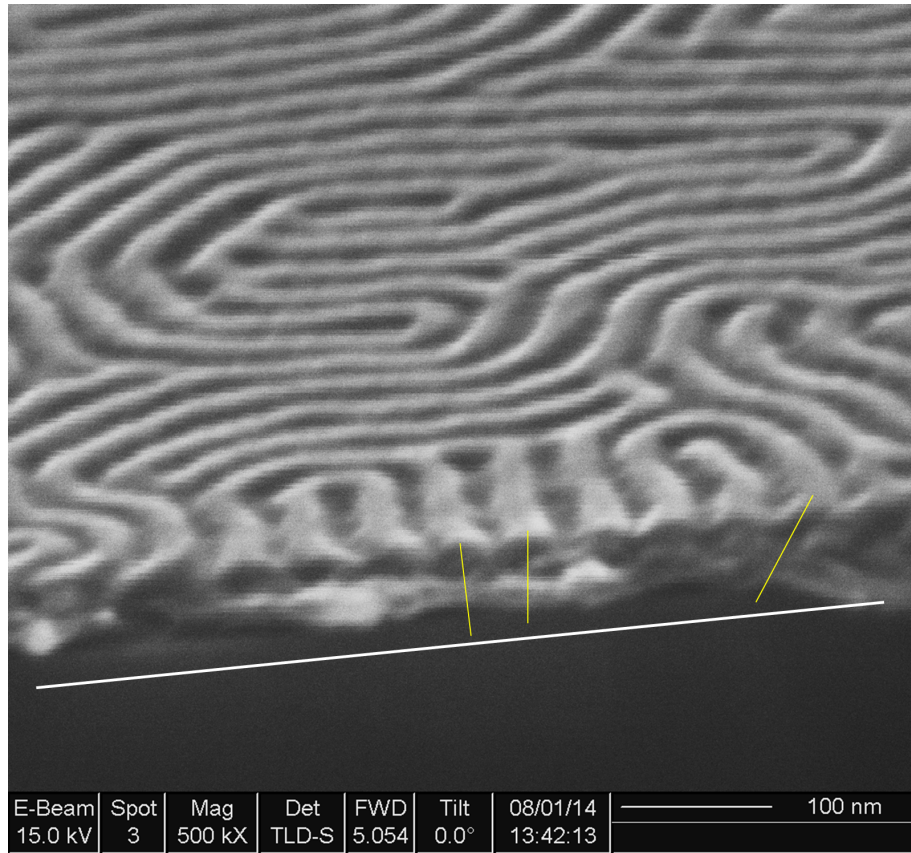


Figure A.9: Film of thickness $t = 1.5L_0$ on brush with $\Sigma = 0.59 \text{ nm}^{-2}$. Substrate orientation is marked by the white line. Yellow lines mark approximate domain orientation with respect to the substrate.

SEM cross-section:

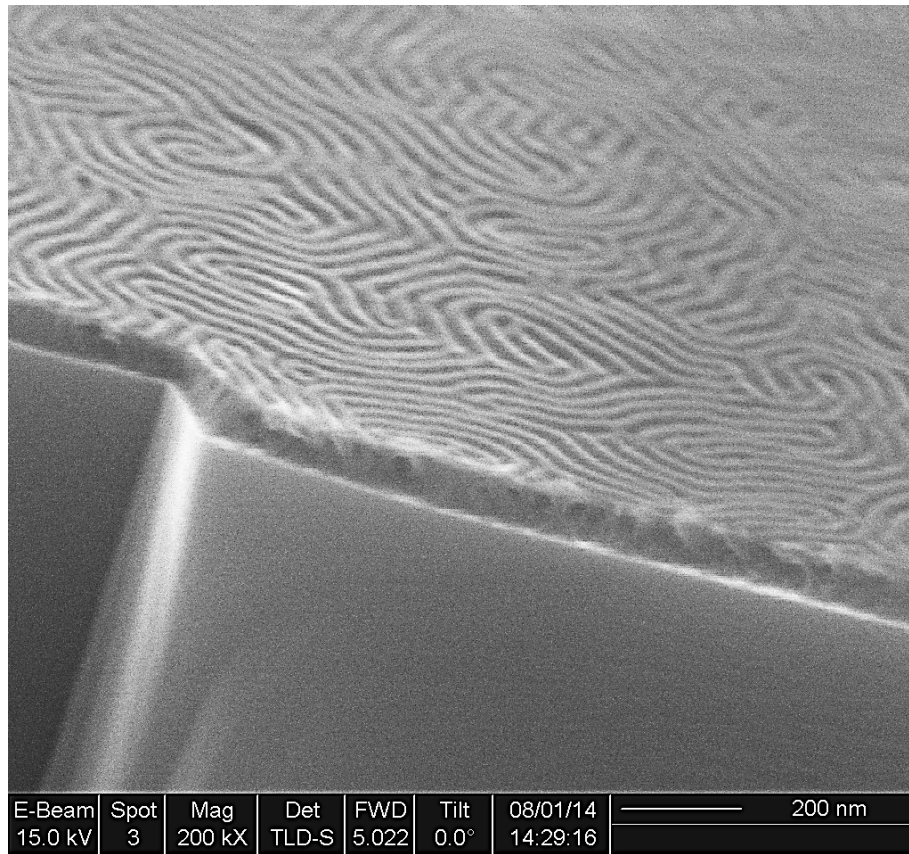


Figure A.10: Film of thickness $t = 2L_0$ on brush with $\Sigma = 0.45 \text{ nm}^{-2}$.

SEM cross-section:

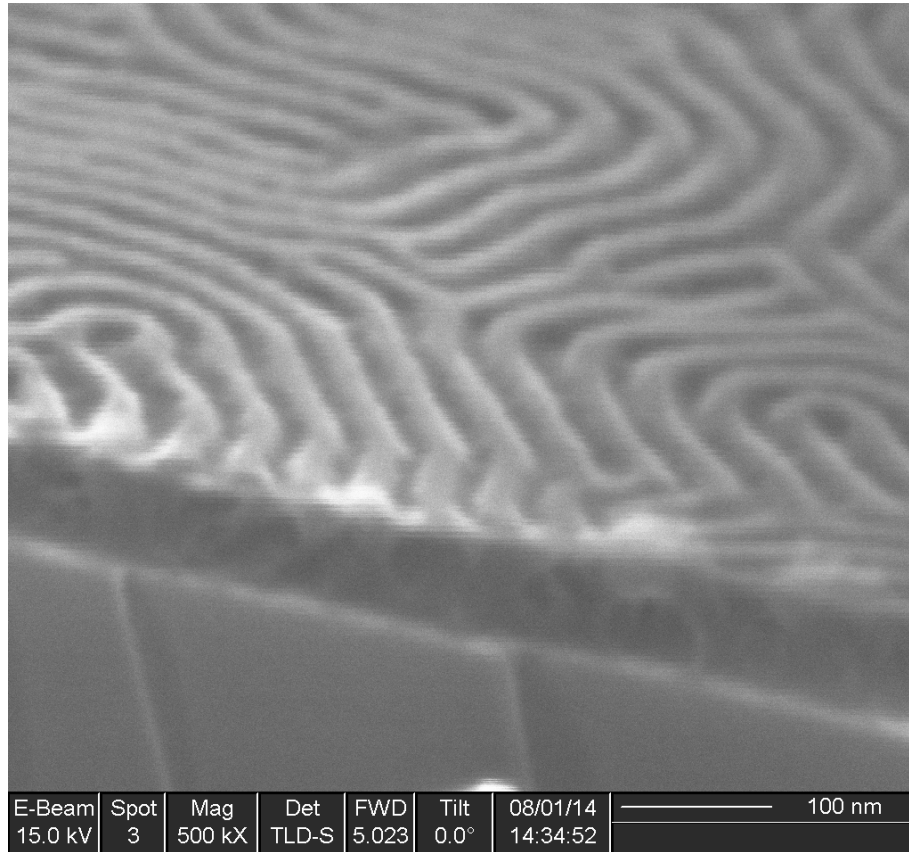


Figure A.11: Film of thickness $t = 2L_0$ on brush with $\Sigma = 0.45 \text{ nm}^{-2}$ at higher magnification compared to Figure A.10.

Appendix B

Nuclear Magnetic Resonance (NMR) Spectroscopy: Figure B.1 compares ^1H NMR spectra of PS bottlebrush polymers acquired before and after removal of the chain transfer agent (CTA) through aminolysis in the presence of triphenylphosphine. The hydrogen at the position of 3.25ppm (H_a), corresponding to the one the dodecyl chain near thiol group, disappears after removal of CTA endgroups. An absorbance peak at 380 nm also disappears after removal of the CTA.

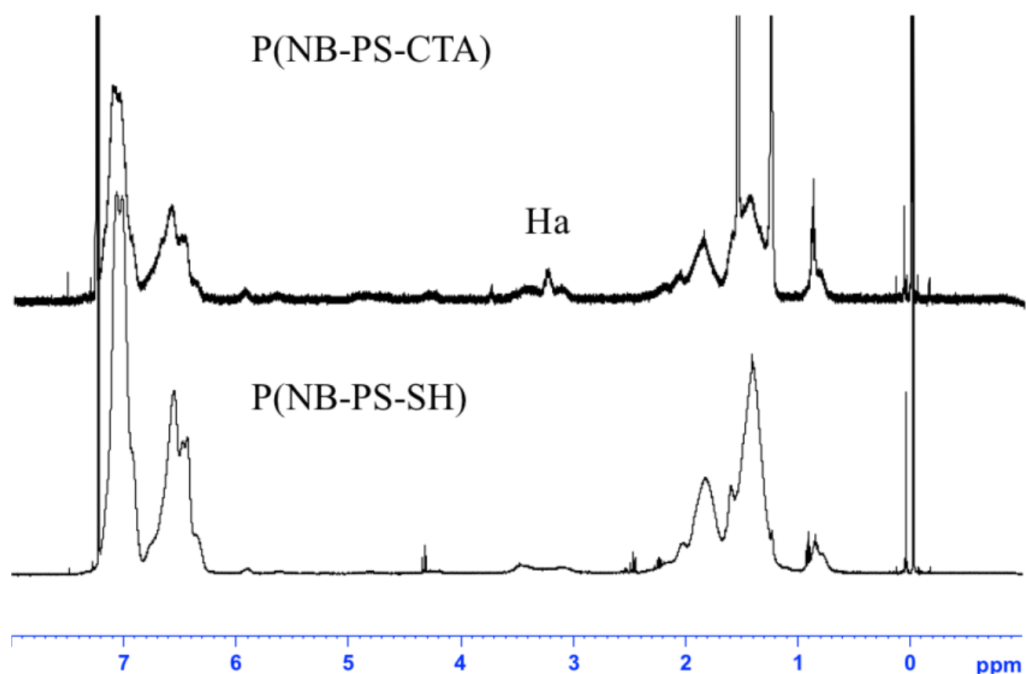


Figure B.1: ^1H NMR spectra of PS bottlebrush with CTA side-chain endgroups (P(NB-PS-CTA) , top); and PS bottlebrush with thiol side-chain endgroups (P(NB-PS-SH)), bottom).

Gel Permeation Chromatography (GPC):

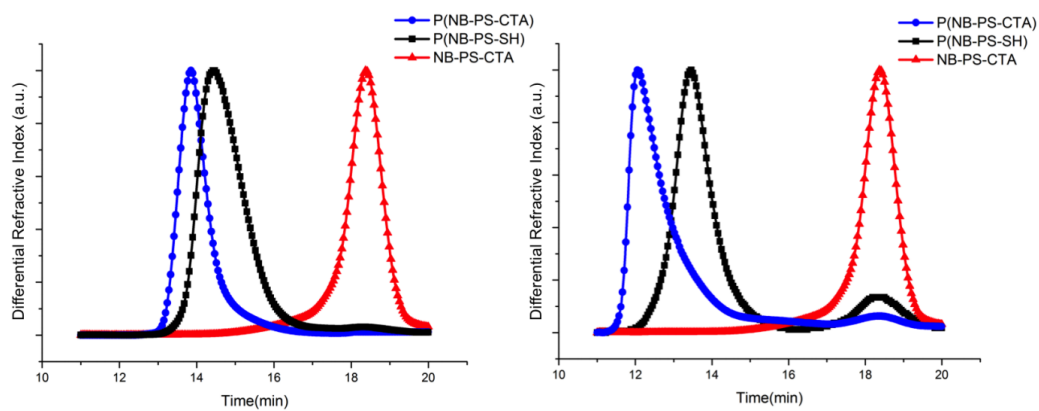


Figure B.2: Size-exclusion chromatography analysis of PS bottlebrush and macromonomers used for PS bottlebrush batch 1 (left) and batch 2 (right).

Miscibility of linear PS/linear dPS by Flory-Huggins Theory: The χ parameter for blends of PS and dPS is [136]:

$$\chi = 0.2T(K)^{-1} - 2.9 \times 10^{-4}.$$

This is valid for the temperature range of approximately 140–230 °C, and at 165 °C, $\chi \approx 1.7 \times 10^{-4}$. The critical solution temperature (T_c) for these blends can be estimated with Flory–Huggins theory as $\chi_c = \frac{1}{2}(\frac{1}{N_{PS}^{1/2}} + \frac{1}{N_{dPS}^{1/2}})^2 = 0.2T_c(K)^{-1} - 2.9 \times 10^{-4}$ [148].

Table B.1 summarizes T_c for blends of linear PS and linear dPS, where we define a linear PS molecule with the equivalent molecular weight to a bottlebrush. Such blends are completely miscible. (Note that we extrapolate χ to temperatures where the model is no longer valid; this is merely to illustrate that the annealing temperature of 165 °C is well above the critical point.)

Table B.1: Critical temperature predicted by Flory-Huggins theory for analogous linear PS/linear dPS blends.

$N_{dPS} = N_m$	$N_{dPS} = N_m$	χ_c	$T_c(^{\circ}C)$
19	12,159	2.810^{-2}	-266
96	12,159	6.210^{-3}	-242
490	12,159	1.810^{-3}	-160
1201	12,159	7.810^{-4}	-75
2500	12,159	4.210^{-4}	8

Atomic Force Microscopy: Atomic force microscopy images were collected with a MultiMode 3 (Veeco) in Tapping Mode using silicon probes with a spring constant of approximately 40 N/m. Typical parameters for data acquisition were 1.7 Hz scan frequency, $10\ \mu\text{m} \times 10\ \mu\text{m}$ scan area, and 512×512 image resolution. The surfaces are very flat with no evidence of phase separation.

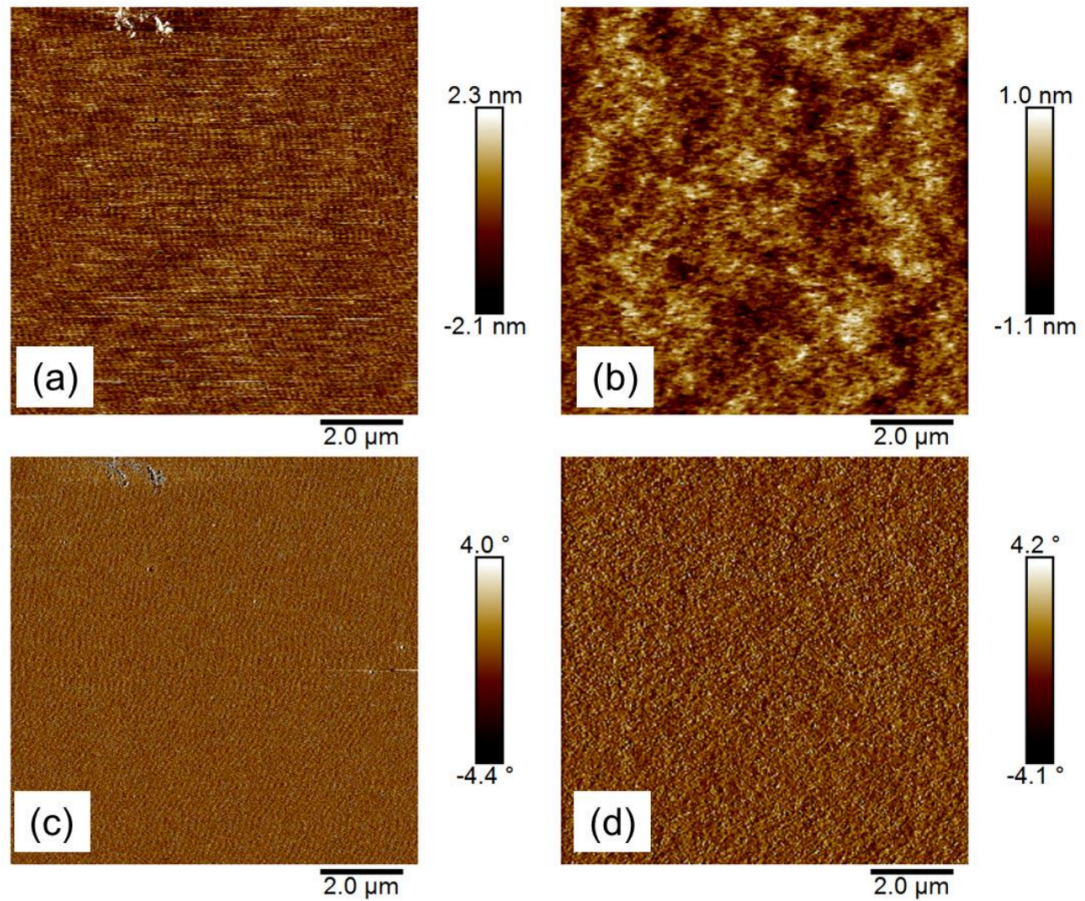


Figure B.3: AFM measurements of blend films (10 wt% bottlebrush polymer). (a,c) Height and phase measurements of films surface, $N_m = 19$; (b,d) Height and phase measurements of films surface, $N_m = 2500$.

Optical Microscopy: Optical microscopy images of as-cast and annealed 150 nm films were acquired using a Nikon LV150 reflected light microscope. Images were acquired at a magnification of 2.5X (Figure B.4) and 100X (Figure B.5). The surfaces exhibit some variation in thickness over very large length scales (ca. 1 mm), but are optically flat over tens of micrometers.

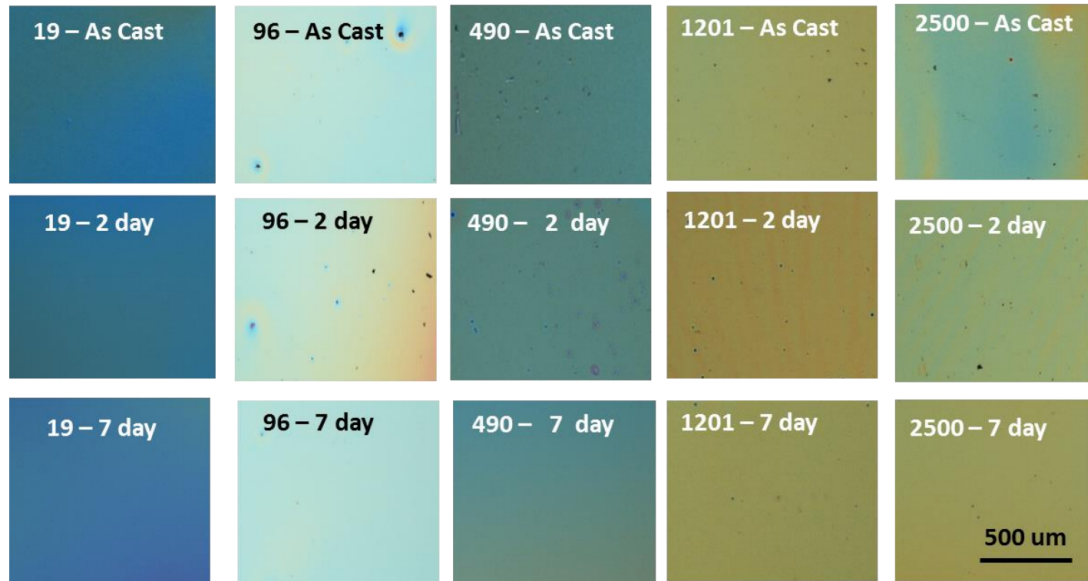


Figure B.4: Optical microscopy (2.5X) of blend films (10 wt% bottlebrush polymer, $N_{sc} = 61$). N_m is noted on each micrograph, along with the annealing time at 165 °C.

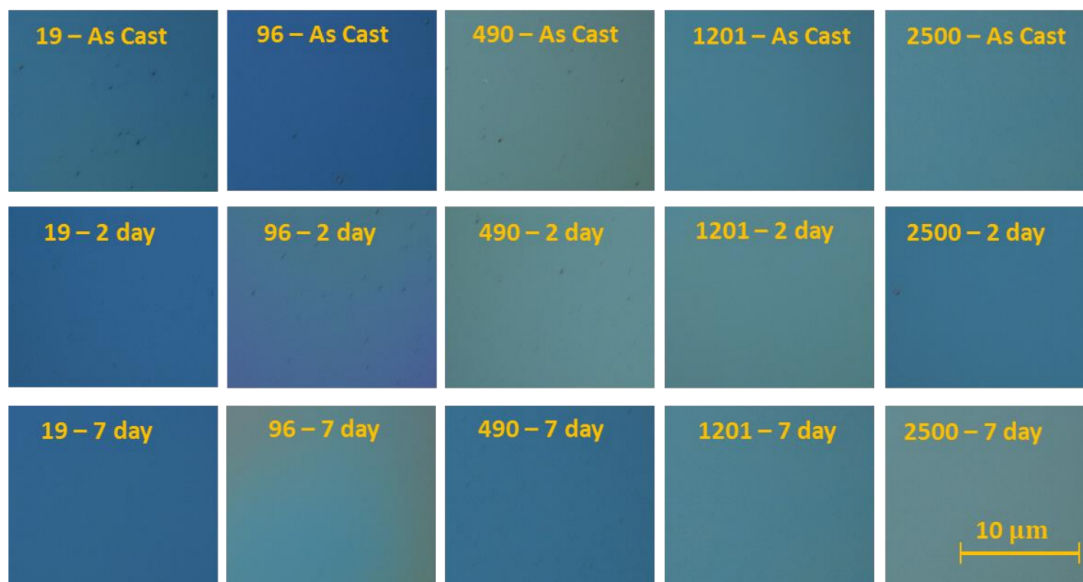


Figure B.5: Optical microscopy (100X) of blend films (10 wt% bottlebrush polymer, $N_{sc} = 61$). N_m is noted on each micrograph, along with the annealing time at 165 °C.

SIMS Data for 200 nm Films: Figure B.5 reports the SIMS data for 200 nm films with fits to the composition profile described in the manuscript. The interfacial excesses are reported in Figure 3.4 of the manuscript.

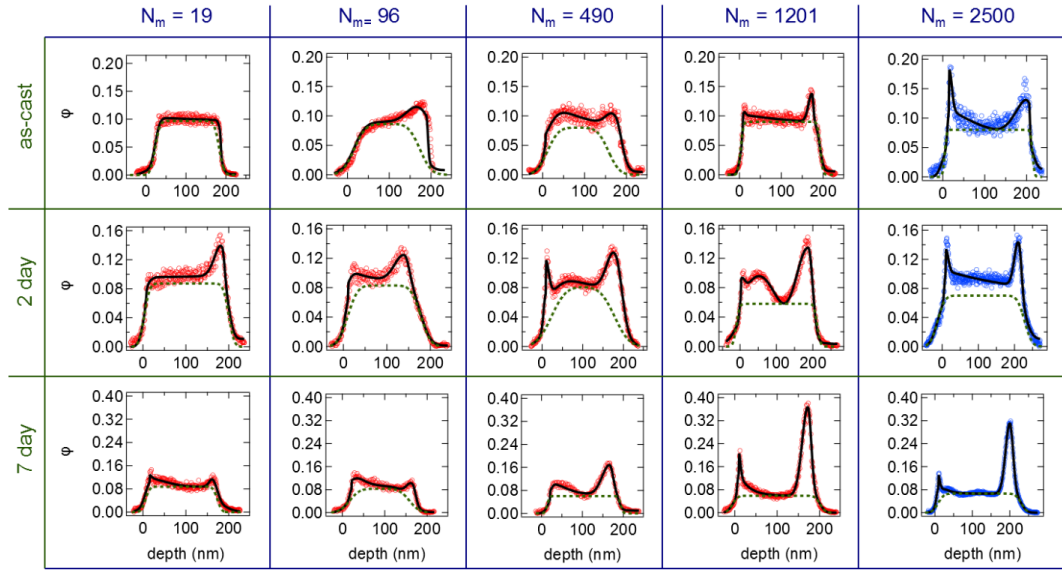


Figure B.6: φ as a function of depth into the film. Each column has different N_m , and each row, different annealing time (165 C). (red: $N_b = 193$, and blue: $N_b = 90$).

Synthesis of NB-dPS-CTA macromonomers: NB-dPS-CTA was prepared via reversible-addition fragmentation chain transfer (RAFT) polymerization. For the synthesis of NB-dPS6K-CTA, d8-styrene (10.0 g, 89.13 mmol), NB-CTA (194.1 mg, 0.349 mmol), and AIBN (5.7 mg, 3.47×10^{-2} mmol) were mixed in a 100 mL RBF, and the solution was purged by bubbling nitrogen through the solution for 30 minutes. The polymerization was initiated by raising the temperature to 65 °C. After 9 h, the reaction flask was removed from the heat and the polymer was recovered by precipitation in methanol. (1.54 g, 71 % yield, based on the conversion of styrene.) The GPC spectrum is presented in Figure B.7.

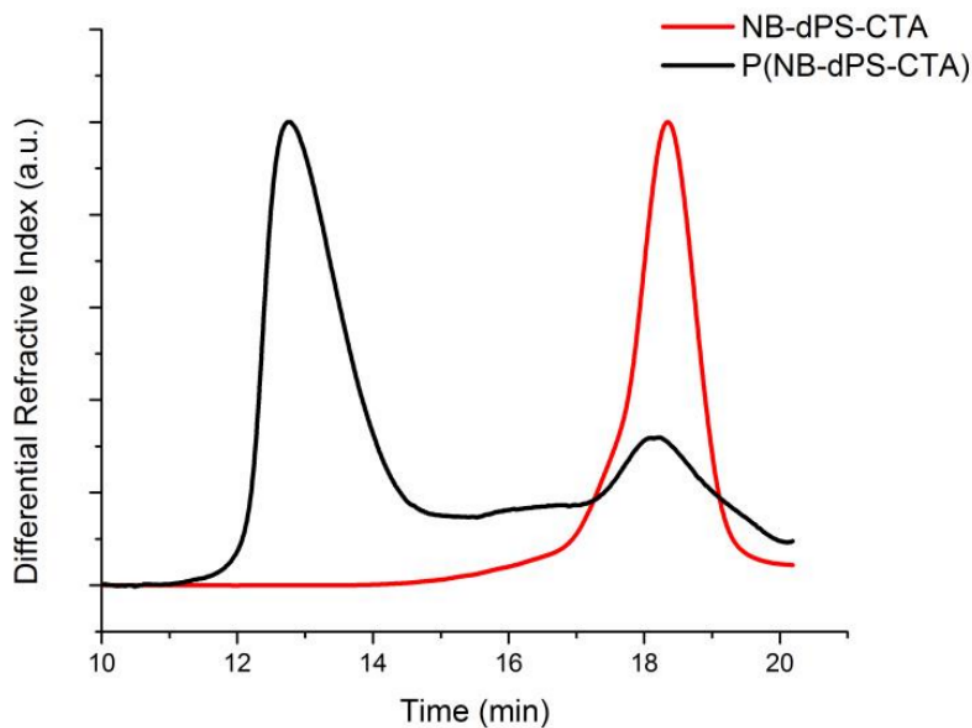


Figure B.7: GPC spectra of dPS macromonomer (NB-dPS-CTA, red line) and dPS bottlebrush (P(NB-dPS-CTA), black line).

P(NB-dPS6K-CTA): Bottlebrush polymers were prepared by ROMP using a procedure similar to that for protonated PS bottlebrushes. The macromonomers were added to a dry, 10 mL round bottom flask charged with a stir bar. The flask was then degassed with three pump-purge cycles, and the desired amount of degassed, anhydrous dichloromethane (total macromonomer concentration was 0.02–0.05 M) was added. $(\text{H}_2\text{IMes})(\text{pyr})_2(\text{Cl})_2$ RuCHPh was dissolved in degassed, anhydrous dichloromethane in a separate flask. The catalyst solution was transferred to the reaction flask containing macromonomers via cannula to initiate the polymerization and stirred at room temperature for at least 1 hour. The reaction was quenched by addition of ethyl vinyl ether after completion. The product was collected by precipitation in methanol dried under vacuum. (95% yield, based on the conversion of NB-PS-CTA). The GPC spectrum is presented in Figure B.7.

SIMS Data for dPS bottlebrush/PS matrix: The objective of these experiments was to determine if isotopic labeling or type of functional group at the end of side-chains play a role in the bottlebrush segregation profiles. After 2 days of thermal annealing at 165C, we observe that dPS bottlebrushes segregate more strongly than PS bottlebrushes at the free surface, which is expected based on (1) the slightly lower surface energy of dPS compared with PS, and (2) the presence of low surface energy CTA groups at the chain ends. The surface and substrate excesses after annealing are $z^* = 3.3$ nm and 4.0 nm, respectively. (For comparison, the corresponding surface excess for PS bottlebrush/dPS matrix was approximately 1.5 nm after 2 or 7 days of annealing, while the substrate excess was 3–6 nm depending on the annealing time.) The dPS bottlebrushes have shorter backbone lengths than either PS bottlebrush, and the difference in size/aspect ratio might play a role in the observed phase behavior.

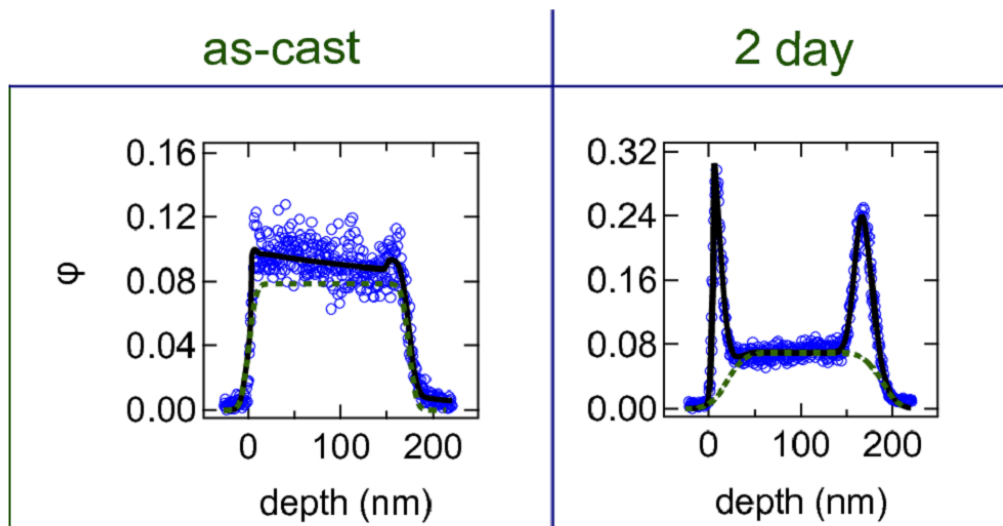


Figure B.8: SIMS data of dPS bottlebrushes (BB) with hydrogenated linear PS. The dPS BB has $N_{sc} = 52$ ($\bar{D} = 1.23$) and $N_b = 49$ ($\bar{D} = 1.28$). The linear PS matrix has $N_m = 2476$ ($\bar{D} = 1.05$).

Neutron Reflectometry (NR): Measurements were made using the Liquids Reflectometer (LR) of the Spallation Neutron Source (SNS) at Oak Ridge National Laboratory with the source to sample distance of 13.6 m, sample to detector distance of 1.5 m, wavelength range $2.5\text{\AA} - 17.5\text{\AA}$, bandwidth 3.5\AA , q range 0.006\AA^{-1} to 0.192\AA^{-1} and minimum reflectivity 1×10^{-7} . Data were collected at six different angles with incident-beam slits set to maintain a constant wave vector resolution of $\delta Q/Q = 0.05$, which allows the data obtained different angles to be stitched together into a single reflectivity curve. Approximately 1 ml of polymer solution (chloroform, 20 mg/ml, 10 wt% bottlebrush) was dropped onto freshly cleaned round Si wafer (diameter: 1 inch) and spun cast at a rate of 1500 RPM for 1 min. Samples were annealed at $165\text{ }^\circ\text{C}$ for 16 hrs under vacuum. Data were collected for each sample before and after annealing.

The aim of NR experiments is to determine the distribution of bottlebrush throughout the thickness of the film. Three NR models were implemented with the Parratt recursions: (i) A single layer film characterized by a uniform concentration of bottlebrush; (ii) A bilayer film that allows for bottlebrush excess at one interface; and (iii) A trilayer film that accounts for excess at both interfaces. The neutron scattering length density (SLD) was determined using the equation $\text{SLD} = b/v$, where b is the monomer scattering length (sum of scattering lengths of constituent atomic nuclei) and v is the monomer volume. The calculated reflectivity curves were optimized for goodness-of-fit using nonlinear regression. Total film thickness and surface roughness were the only adjustable parameters for Model (i). Total film thickness, surface roughness, and amount of bottlebrush excess were adjustable parameters for Models (ii) and (iii), subject to the constraint that the total amount of bottlebrush in the film was 10 wt%.

Figure B.9 shows representative data with best-fit results for PS bottlebrush (10

wt%) blended with 2 kg/mol dPS. Before annealing, clear oscillations in the scattered intensity are observed. The data can be fit to any of the three models (although none of the fits are perfect, as nonlinear regression is too sensitive to the initial guess). After annealing, the oscillations are severely damped due to roughening of the free surface and/or the broad gradients in bottlebrush composition.

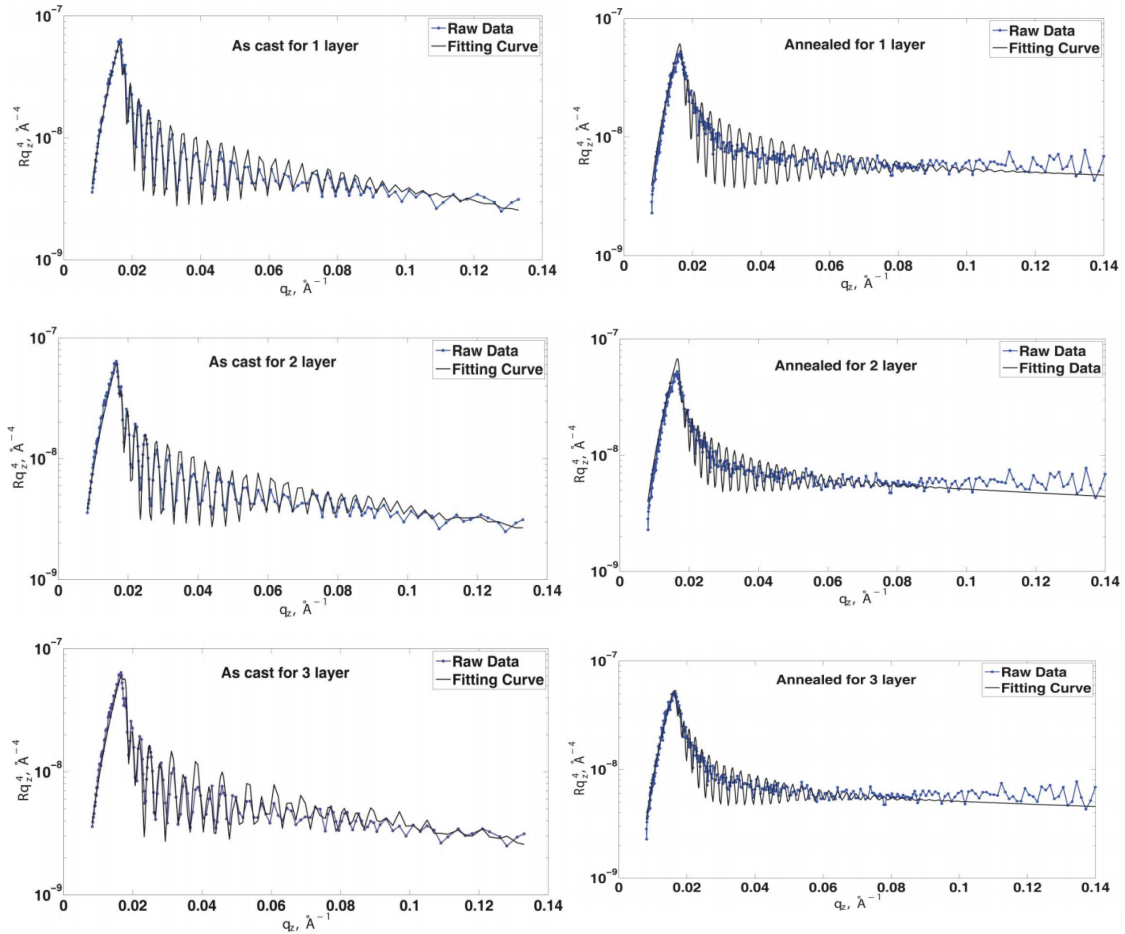


Figure B.9: Representative neutron reflectivity spectra of bottlebrush polymer mixed with 2K deuterated linear PS for as cast and thermally annealed films. Data were fit with a 1, 2, or 3-layer model.